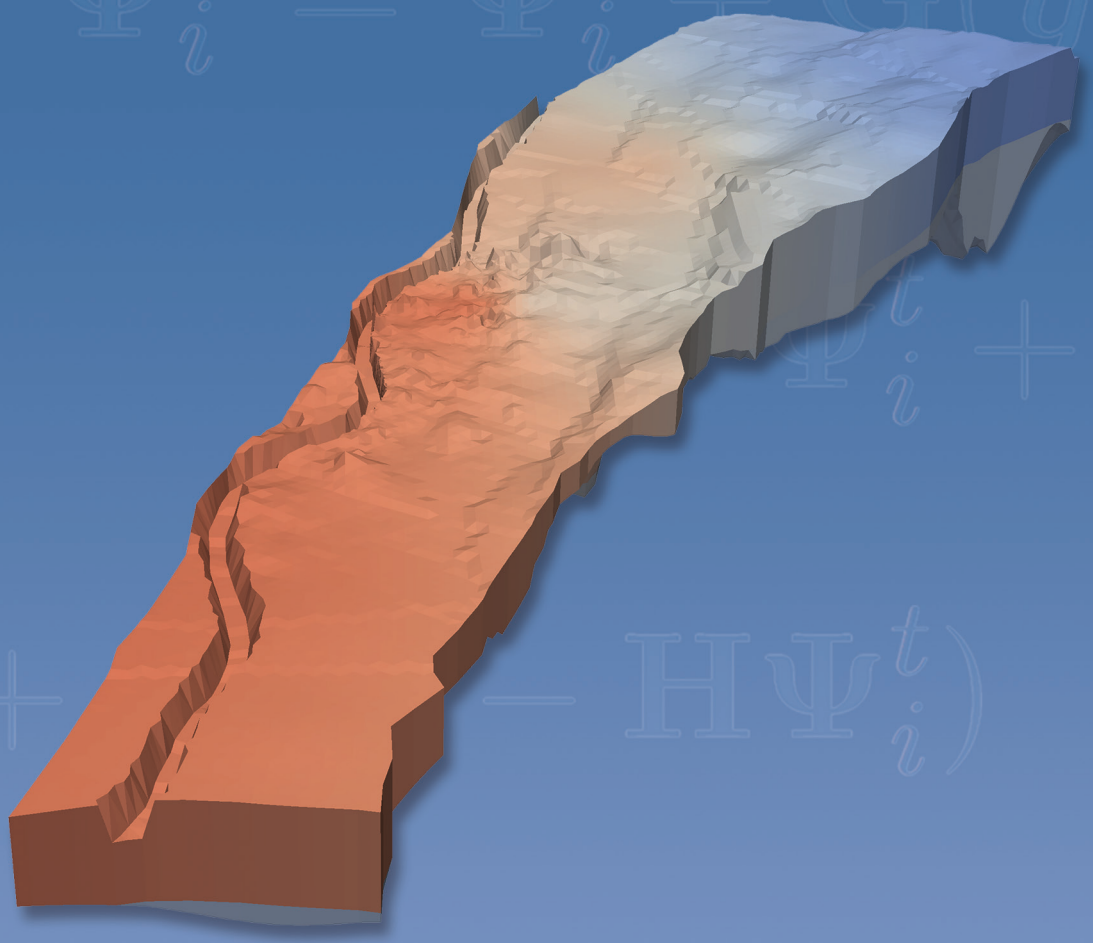

Improved characterization of river-aquifer interactions through data assimilation with the Ensemble Kalman Filter

Wolfgang Kurtz

JÜLICH
FORSCHUNGSZENTRUM

Member of the Helmholtz Association

Schriften des Forschungszentrums Jülich
Reihe Energie & Umwelt / Energy & Environment Band / Volume 199

Forschungszentrum Jülich GmbH
Institute of Bio- and Geosciences (IBG)
Agrosphere (IBG-3)

Improved characterization of river-aquifer interactions through data assimilation with the Ensemble Kalman Filter

Wolfgang Kurtz

Schriften des Forschungszentrums Jülich
Reihe Energie & Umwelt / Energy & Environment Band / Volume 199

ISSN 1866-1793 ISBN 978-3-89336-925-6

Bibliographic information published by the Deutsche Nationalbibliothek.
The Deutsche Nationalbibliothek lists this publication in the Deutsche Nationalbibliografie; detailed bibliographic data are available in the Internet at http://dnb.d-nb.de.

Publisher and Distributor: Forschungszentrum Jülich GmbH
Zentralbibliothek
52425 Jülich
Tel: +49 2461 61-5368
Fax: +49 2461 61-6103
Email: zb-publikation@fz-juelich.de
www.fz-juelich.de/zb

Cover Design: Grafische Medien, Forschungszentrum Jülich GmbH

Printer: Grafische Medien, Forschungszentrum Jülich GmbH

Copyright: Forschungszentrum Jülich 2013

Schriften des Forschungszentrums Jülich
Reihe Energie & Umwelt / Energy & Environment, Band / Volume 199

D 82 (Diss., RWTH Aachen University, 2013)

ISSN 1866-1793
ISBN 978-3-89336-925-6

The complete volume is freely available on the Internet on the Jülicher Open Access Server (JUWEL) at www.fz-juelich.de/zb/juwel

Neither this book nor any part of it may be reproduced or transmitted in any form or by any means, electronic or mechanical, including photocopying, microfilming, and recording, or by any information storage and retrieval system, without permission in writing from the publisher.

"Wahrlich es ist nicht das Wissen, sondern das Lernen, nicht das Besitzen sondern das Erwerben, nicht das Da-Seyn, sondern das Hinkommen, was den grössten Genuss gewährt."

C. F. Gauß

Contents

List of Figures vii

List of Tables xiii

List of Symbols xv

List of Acronyms xix

Abstract xxi

Zusammenfassung xxiii

1 Introduction 1

2 Theory 5
2.1 Flow and heat transport in porous media 5
2.2 Data assimilation with the Ensemble Kalman Filter 8
2.3 Usage of EnKF in subsurface characterization 11

3 Identification of time-variant river bed properties 15
3.1 Introduction 15
3.2 Methodology 18
3.3 Model description 21
3.4 Synthetic experiments 23
3.5 Results 25
3.5.1 Increase of L (scouring event) 25
3.5.2 Decrease of L (sedimentation event) 27
3.5.3 Performance of EnKF for combined flooding and sedimentation events 29
3.5.4 Temperature dependency of L 30
3.5.5 Influence of spatial patterns 31
3.5.6 Influence of uncertain hydraulic conductivities 32
3.5.7 Influence of ensemble bias 33
3.5.8 Sensitivity on updating strategy 35
3.5.9 Use of covariance inflation to improve filtering results of EnKF . . 37
3.6 Discussion 40
3.7 Conclusions 44

4 Characterization of heterogeneous river bed properties 47
4.1 Introduction . . . 47
4.2 Data assimilation with the Ensemble Kalman Filter . . . 51
4.2.1 General description of the data assimilation algorithm . . . 51
4.2.2 Specific usage of EnKF for river-aquifer interactions . . . 53
4.3 Model description . . . 53
4.4 Synthetic experiments . . . 55
4.4.1 Reference fields . . . 56
4.4.2 Zonation . . . 57
4.4.3 Ensemble generation . . . 57
4.4.4 Settings for data assimilation with EnKF . . . 58
4.4.5 Performance assessment of simulations . . . 59
4.5 Results . . . 60
4.5.1 Strongly heterogeneous case (scenario A) . . . 60
4.5.2 Strongly heterogeneous case with lower observation density . . . 62
4.5.3 Mildly heterogeneous case (scenario B) . . . 64
4.5.4 Strongly heterogeneous case with a predefined zonation (scenario C) . . . 65
4.6 Discussion . . . 66
4.7 Conclusions . . . 69

5 Assimilation of groundwater temperatures 71
5.1 Introduction . . . 71
5.2 Materials and Methods . . . 74
5.2.1 Joint assimilation of piezometric head and temperature data . . . 74
5.2.2 Parallelization of the assimilation code EnKF3d-SPRING . . . 76
5.2.3 Localization . . . 77
5.2.4 Synthetic aquifer model . . . 78
5.2.5 Model and input data for real-world case . . . 79
5.3 Results . . . 84
5.3.1 Synthetic experiments . . . 84
5.3.2 Assimilation of groundwater temperature data for real-world case . 90
5.3.2.1 Assimilation period . . . 90
5.3.2.2 Validation period . . . 96
5.3.2.3 Zonation of leakage coefficients for heat transport simulations . . . 100
5.4 Discussion . . . 101
5.5 Conclusions . . . 104

6 Summary and outlook 107

A Algorithm for adaptive covariance inflation 111

Bibliography 115

Acknowledgements 125

List of Figures

3.1 Schematic representation of model domain. River Sihl corresponds to leakage zone V and river Limmat corresponds to leakage zones I-IV. . . . 22

3.2 Temporal evolution of zonal leakage coefficients (period January 2004 - August 2005) for reference run and update with the Ensemble Kalman Filter for simulation scenario A (Table 3.1). 26

3.3 Temporal evolution (period January 2004 - August 2005) of root mean square error of piezometric heads ($RMSE_h$) at observation points for an unconditional simulation ('unconditioned', no update of piezometric heads and leakage coefficients), an update of piezometric heads every 10 days ('update h') and for a joint update of piezometric heads and leakage coefficients every 10 days ('update h+L'). 26

3.4 Temporal evolution (period January 2004 - August 2005) of fluxes between river and aquifer for an unconditional simulation ('unconditioned', no update of piezometric heads and leakage coefficients), an update of piezometric heads every 10 days ('update h') and for a joint update of piezometric heads and leakage coefficients every 10 days ('update h+L'). Fluxes in the upper (positive) part of each diagram are from river to aquifer and fluxes in the lower part (negative) are from aquifer to river. . 28

3.5 Spatial distribution of river-aquifer exchange fluxes for an unconditional simulation ('unconditional', no update of piezometric heads and leakage coefficients), an update of piezometric heads every 10 days ('update h') and for a joint update of piezometric heads and leakage coefficients every 10 days ('update h+L'). 28

3.6 Temporal evolution of zonal leakage coefficients (period January 2004 - April 2007) for reference run and update with the Ensemble Kalman Filter for simulation scenario B (Table 3.1). 29

3.7 Temporal evolution of zonal leakage coefficients (period January 2004 - August 2005) for reference run and update with the Ensemble Kalman Filter for simulation scenario C (Table 3.1). 30

3.8 Temporal evolution of zonal leakage coefficients (period January 2004 - August 2005) for reference run and update with the Ensemble Kalman Filter for simulation scenario D (Table 3.1). 31

3.9 Temporal evolution of zonal leakage coefficients (period January 2004 - August 2005) for reference run and update with the Ensemble Kalman Filter when the zonal leakage coefficient of zone III in the reference run is increased by one log unit at day 155. 32

3.10 Temporal evolution of zonal leakage coefficients (period January 2004 - August 2005) for reference run and an update of either leakage coefficients alone ('ensemble mean L') or a joint update of leakage coefficients and hydraulic conductivities of the aquifer ('ensemble mean L+K') for simulation scenario A (Table 3.1). 33
3.11 Ensemble mean of $\log(K)$ for initial ensemble (left) and at time step 600 (right) for model layer 4 when hydraulic conductivities and leakage coefficients are jointly updated every 10 days. 34
3.12 Temporal evolution of zonal leakage coefficients (period January 2004 - August 2005) for reference run and update with the Ensemble Kalman Filter for scenario A when the initial ensemble mean of leakage coefficients was biased compared to the initial values of the reference run. 34
3.13 Temporal evolution (period January 2004 - August 2005) of ensemble mean (upper row) and ensemble standard deviation (lower row) of zonal leakage coefficients for different updating frequencies of piezometric heads and leakage coefficients (simulation scenario A). 36
3.14 Temporal evolution (period January 2004 - August 2005) of root mean square error of leakage coefficients for different numbers of observation points (simulation scenario A). 37
3.15 Comparison of temporal evolution of zonal leakage coefficients without (upper row) and with (lower row) adaptive covariance inflation for scenario A (damping factor $\alpha = 0.1$). 39
3.16 Comparison of temporal evolution of zonal leakage coefficients without (upper row) and with (lower row) adaptive covariance inflation for scenario A (damping factor $\alpha = 0.2$). 39
3.17 Temporal evolution of zonal leakage coefficients with adaptive covariance inflation for scenario B (upper row), C (middle row) and D (lower row) (damping factor $\alpha = 0.2$). 40
3.18 Temporal evolution (period January 2004 - August 2005) of ensemble mean (upper row) and ensemble standard deviation (lower row) of zonal leakage coefficients for different updating frequencies of piezometric heads and leakage coefficients with covariance inflation (simulation scenario A). 41

4.1 Schematic representation of model domain and boundary conditions. . . . 54
4.2 Forcing data for synthetic experiments. Represented are total amounts of artificial recharge, extraction from bank filtration and extracted drinking water (left), as well as river discharges (middle) and total recharge amount over the model domain (right), for a period of 609 days (January 2004 - August 2005). 55
4.3 Reference fields of leakage coefficients for scenario A. The x-axis shows the x-coordinate according to the Swiss coordinate system. In the eastern part of the model domain the rivers Limmat and Sihl have overlapping x-coordinates and therefore for this part two leakage values are given. . . 56
4.4 Spatial representation of heterogeneity for four parameter ensembles. In the fully heterogeneous case (Z_{het}) an individual leakage coefficient is assigned to each river node. For the zonated ensembles (Z_5, Z_3 and Z_2) each color corresponds to a separate leakage zone. The river nodes within a leakage zone share the same leakage coefficient. 58

4.5 Initial ensembles of leakage coefficients (colored) and reference field I (black) for scenario A for all river nodes (rivers Limmat and Sihl) along x-axis of model domain. 59
4.6 $RMSE_h$ of conditional simulations with EnKF for ten reference fields of leakage coefficients (scenario A). Four different ensembles are compared. EnKF jointly updated hydraulics heads and leakage coefficients with measurement data from 100 observation points. 60
4.7 Cumulative directional fluxes between river and aquifer for conditional simulations with EnKF for four representations of spatial heterogeneity (scenario A). Results are shown for reference I. Fluxes from river to aquifer have a positive sign. 61
4.8 Total amount of water exchanged between river and aquifer over the whole simulation period (609 days) for scenario A. Red lines mark the water exchange for the different reference runs. On the right hand side the description of the boxplots is illustrated. 62
4.9 Fluxes between river and aquifer along x-axis of model domain for conditional simulations with EnKF at simulation day 300 (scenario A, reference IV). Fluxes from river to aquifer have a positive sign. 63
4.10 Ensembles of leakage coefficients (colored) and reference field (black) along x-axis of model domain at day 1 (upper row) and at day 600 (lower row) for scenario A. 64
4.11 Ensembles of leakage coefficients (colored) and reference field (black) along x-axis of model domain at day 600 (lower row) for scenario A when only 10 observation points are available. 64
4.12 Total amount of water exchanged between river and aquifer over the whole simulation period (609 days) for conditional simulations with EnKF (scenario B). Red lines mark the water exchange for the different reference runs. 65
4.13 Total amount of water exchanged between river and aquifer over the whole simulation period (609 days) for conditional simulations with EnKF (scenario C). Red lines mark the water exchange for the different reference runs. 66
4.14 Ensembles of leakage coefficients (colored) and reference field (black) along x-axis of model domain at day 1 (upper row) and at day 600 (lower row) for scenario C. 67

5.1 Localization function $\gamma(d, \eta)$ for a length scale η of 500 m. 78
5.2 Model setup for synthetic experiments. 79
5.3 Forcing data for synthetic experiments. 79
5.4 Position of observation points for piezometric heads and groundwater temperatures. The upper plot shows the distribution of observation points over the whole Limmat aquifer model and the lower plot illustrates the distribution of observation points in the Hardhof area. 82
5.5 Forcing data of the model for the years 2006 and 2007 (initial model spinup and assimilation period). 84
5.6 Forcing data of the model for the hydrological year 2011 (verification period). 84
5.7 Root mean square error of piezometric heads (left) and groundwater temperatures (right) for scenarios in Table 5.2. 85

5.8 Average T fields at time step 200 for updating scenarios in Table 5.2. . . . 86
5.9 Root mean square error for updated hydraulic conductivities (left) and updated leakage coefficients (right) for scenarios SY_{hKL}, SY_{hTKL} and SY_{TKL} (Table 5.2). . . . 86
5.10 Updated fields of hydraulic conductivities (end of simulation period) for scenarios SY_{hKL}, SY_{hTKL} and SY_{TKL} (Table 5.2). . . . 88
5.11 Updated fields of leakage coefficients (end of simulation period) for scenarios SY_{hKL}, SY_{hTKL} and SY_{TKL} (Table 5.2). . . . 88
5.12 Root mean square error of groundwater temperatures (left) and hydraulic conductivities (right) for different localization distances (scenario SY_{hTKL} in Table 5.2). . . . 89
5.13 Updated fields of hydraulic conductivities (end of simulation period) for different localization distances (scenario SY_{hTKL} in Table 5.2). . . . 89
5.14 Temporal evolution of Root Mean Square Error (RMSE) (left panels) and statistics of residuals for the whole assimilation period (right panels) of h and T for different updating scenarios. The red line in the right panels shows the median of residuals for scenario RW_{hTKL}. . . . 91
5.15 Evolution of groundwater temperatures during the assimilation period for one observation point with partly missing data. Red lines display measured groundwater temperatures and gray lines display different realizations of the ensemble. . . . 91
5.16 Initial (left) and updated fields of leakage coefficients after the last assimilation cycle. Updated leakage coefficients are shown for a scenario without (middle) and with (right) assimilation of groundwater temperatures. . . . 92
5.17 Temporal evolution of RMSE (left panels) and statistics of residuals for the whole assimilation period (right panels) of h and T for different measurement errors. $\epsilon \times 5$ and $\epsilon \times 10$ means a five or ten times higher measurement error compared to the settings give in Table 5.3. The red line in the right panels shows the median of residuals for scenario RW_{hTKL}. . . 93
5.18 Temporal evolution of RMSE (left panels) and statistics of residuals for the whole assimilation period (right panels) of h and T for different observation density with and without parameter update. The red line in the right panels shows the median of residuals for scenario RW_{hTKL}. . . . 94
5.19 Temporal evolution of RMSE (left panels) and statistics of residuals for the whole assimilation period (right panels) of h and T for different values of the localization length scale η. The red line in the right panels shows the median of residuals for scenario RW_{hTKL}. . . . 95
5.20 Examples for the spatial distribution of covariances for piezometric heads (left) and groundwater temperatures (right). Covariances were derived from data of scenario RW_{uc} for time step 200 of the assimilation period. Data are shown for one observation point of piezometric heads and groundwater temperatures respectively. . . . 95
5.21 Updated fields of leakage coefficients after the last assimilation cycle. Data are shown for a scenario without localization and two scenarios with localization with a different localization length scale η (2000 and 3000 m). 96
5.22 Mean fields of hydraulic conductivity after the last assimilation cycle for parameter update without localization and with localization with two localization length scales η (2000 and 3000 m). As a comparison the average initial field of hydraulic conductivities is shown. . . . 97

5.23 Cross-sections (y-z plane) of the ensemble mean of hydraulic conductivities for the drinking water well most close to river Limmat. Coordinates of the subfigures are given relative to this drinking water well. Data are shown for one scenario without localization, two scenarios with different localization length scales η (2000 and 3000 m) and the initial ensemble mean. 98
5.24 Temporal evolution of RMSE (left panels) and statistics of residuals for the whole validation period (right panels) of h and T for different updating scenarios. The red line in the right panels shows the median of residuals for scenario $\mathrm{RW_{hTKL}}$. 99
5.25 Temporal evolution of RMSE (left panels) and statistics of residuals for the whole validation period (right panels) of h and T for different updating scenarios and measurement errors. The red line in the right panels shows the median of residuals for scenario $\mathrm{RW_{hTKL}}$. 99
5.26 Temporal evolution of RMSE (left panels) and statistics of residuals for the whole validation period (right panels) of h and T for different values of localization length scale η. The red line in the right panels shows the median of residuals for scenario $\mathrm{RW_{hTKL}}$. 100
5.27 Exchange fluxes between river and aquifer for the validation period of different localization scenarios. The right hand diagram additionally shows statistics for the total amount of exchanged water for the whole validation period. 100
5.28 Initial (upper diagram) and updated (lower diagram) ensembles of leakage coefficients for four different zonation approaches. Values are shown along the x-axis of the model domain. Note that in the eastern part of the model domain there is an overlap of river Sihl and Limmat with respect to x-coordinates. 101
5.29 Temporal evolution of RMSE (left panels) and statistics of residuals for the whole validation period (right panels) of h and T for four different zonation approaches. The red line in the right panels shows the median of residuals for scenario $\mathrm{RW_{hTKL}}$. 102

List of Tables

3.1 Employed reference scenarios for the temporal evolution of leakage coefficients (L) 24
3.2 Different updating scenarios for zonal leakage coefficients. 35

4.1 Predefined zonal leakage values for generation of reference fields for scenario C. Leakage zones are numbered from west to east. 57
4.2 Default settings for data assimilation with Ensemble Kalman Filter (EnKF). 58

5.1 Parameters for heat transport simulations and for data assimilation with EnKF for synthetic experiments. 80
5.2 Simulation scenarios for synthetic case. Multiple column entries indicate that the scenario was simulated with varying values for this variable. . . . 80
5.3 Parameters for heat transport calculations and data assimilation with EnKF for real-world case. 81
5.4 Simulation scenarios for real-world case. Multiple column entries indicate that the scenario was simulated with varying values for this variable. . . . 83
5.5 Time periods for heat transport simulations. 84

List of Symbols

A_{leak}	$[\mathrm{L}^2]$	Surface area of leakage flux
c_s	$[\mathrm{L}^2\mathrm{T}^{-2}\Theta^{-1}]$	Specific heat capacity of solid material
c_w	$[\mathrm{L}^2\mathrm{T}^{-2}\Theta^{-1}]$	Specific heat capacity of water
$c_v{}^*$	$[\mathrm{MT}^{-2}\mathrm{L}^{-1}\Theta^{-1}]$	Combined volumetric heat capacity of solid material and water
$\mathbf{C}$	$[*]$	Covariance matrix
d	$[\mathrm{L}]$	Euclidean distance
D	$[\mathrm{L}^2\mathrm{T}^{-1}]$	Dispersion coefficient
D_y	$[*]$	Absolute difference between ensemble mean and measurement at observation points
g	$[\mathrm{LT}^{-2}]$	Gravitational acceleration
$\mathbf{G}$	$[-]$	Kalman gain matrix
h	$[\mathrm{L}]$	Piezometric head
h^{gw}	$[\mathrm{L}]$	Groundwater level underneath river
h^{river}	$[\mathrm{L}]$	River stage
$\hat{\boldsymbol{h}}$	$[\mathrm{L}]$	Vector of piezometric heads at observation points
$\boldsymbol{h}$	$[\mathrm{L}]$	Vector of piezometric heads
$\mathbf{H}$	$[-]$	Matrix for mapping simulated states to observation points
j_a	$[\mathrm{MT}^{-3}]$	Advective heat flux
j_d	$[\mathrm{MT}^{-3}]$	Dispersive heat flux
j_m	$[\mathrm{MT}^{-3}]$	Conductive heat flux
k	$[\mathrm{L}^2]$	Permeability
$k_r(\theta)$	$[-]$	Relative permeability
K	$[\mathrm{LT}^{-1}]$	Hydraulic conductivity
$\boldsymbol{K}$	$[\mathrm{LT}^{-1}]$	Vector of hydraulic conductivities
l	$[-]$	Empirical parameter for Mualem-van Genuchten model
L	$[\mathrm{T}^{-1}]$	Leakage coefficient
$\boldsymbol{L}$	$[\mathrm{T}^{-1}]$	Vector of leakage coefficients

n	$[-]$	Porosity
n_p	$[-]$	Pore size index
$\mathrm{N_{leak}}$	$[-]$	Number of leakage nodes
$\mathrm{N_{obs}}$	$[-]$	Number of observation points
$\mathrm{N_{nodes}}$	$[-]$	Number of model nodes
$\mathrm{N_{real}}$	$[-]$	Number of realizations
$\mathrm{N_{param}}$	$[-]$	Number of uncertain model parameters
p	$[\mathrm{ML^{-1}T^{-2}}]$	Pressure
q_f	$[\mathrm{ML^{-3}T^{-1}}]$	Source/ sink term for groundwater flow
q_h	$[\mathrm{ML^{-1}T^{-3}}]$	Source/ sink terms for heat transport
Q_{leak}	$[\mathrm{L^3T^{-1}}]$	Leakage flux between river and aquifer
$\mathbf{R}$	$[*]$	Covariance matrix of observations
S_s	$[\mathrm{L^{-1}}]$	Specific storativity
T	$[\Theta]$	Temperature
$\boldsymbol{T}$	$[\Theta]$	Vector of groundwater temperatures
$\hat{\boldsymbol{T}}$	$[\Theta]$	Vector of groundwater temperatures at observation points
v	$[\mathrm{LT^{-1}}]$	Groundwater flow velocity
$\boldsymbol{y}^0$	$[*]$	Vector of measurements
$\boldsymbol{y}^h$	$[\mathrm{L}]$	Measurement vector for piezometric heads
$\tilde{\boldsymbol{y}}$	$[*]$	Perturbed measurement vector
$\boldsymbol{y}^T$	$[\Theta]$	Measurement vector for groundwater temperatures
z	$[\mathrm{L}]$	Height above datum
α	$[-]$	Damping factor for EnKF-update of model parameters
δ	$[\mathrm{L}]$	Dispersivity
ϵ	$[*]$	Measurement error
$\tilde{\boldsymbol{\epsilon}}$	$[*]$	Perturbation vector
η	$[\mathrm{L}]$	Length scale for localization function
$\gamma(d, \eta)$	$[-]$	Localization function
κ_s	$[\mathrm{ML\Theta^{-1}T^{-3}}]$	Thermal conductivity of solid material
${\kappa_v}^*$	$[\mathrm{ML\Theta^{-1}T^{-3}}]$	Combined thermal conductivity of solid material and water
κ_w	$[\mathrm{ML\Theta^{-1}T^{-3}}]$	Thermal conductivity of water
λ	$[-]$	Inflation factor
μ	$[\mathrm{ML^{-1}T^{-1}}]$	Dynamic viscosity
$\boldsymbol{\Omega}$	$[-]$	Localization matrix
$\boldsymbol{\phi}$	$[*]$	Vector of model parameters
$\boldsymbol{\psi}$	$[*]$	State vector
$\boldsymbol{\psi}^t$	$[*]$	Forecasted state vector

$\hat{\boldsymbol{\psi}}$	$[*]$	State vector at observation points
$\hat{\boldsymbol{\psi}}_m$	$[*]$	Forecasted ensemble mean of state vector at observation points
$\hat{\boldsymbol{\psi}}^t$	$[*]$	Forecasted state vector at observation points
$\boldsymbol{\Psi}$	$[*]$	State-parameter vector
$\boldsymbol{\Psi}^t$	$[*]$	Forecasted state-parameter vector
χ	$[*]$	Variability of residuals for covariance inflation
ρ_s	$[\mathrm{ML}^{-3}]$	Density of solid material
ρ_w	$[\mathrm{ML}^{-3}]$	Density of water
$S(\theta)$	$[-]$	Saturation
σ^2_λ	$[-]$	Variance of inflation factor
$\sigma^2_{y^0}$	$[*]$	Variance of measurements
$\sigma^2_{\hat{\psi}}$	$[*]$	Variance of state-vector at observation points
θ	$[\mathrm{L}^3\mathrm{L}^{-3}]$	Water content
$\hat{\theta}$	$[\mathrm{L}^3\mathrm{L}^{-3}]$	Normalized water content
θ_r	$[\mathrm{L}^3\mathrm{L}^{-3}]$	Residual water content
θ_s	$[\mathrm{L}^3\mathrm{L}^{-3}]$	Saturated water content
∇	$[\mathrm{L}^{-1}]$	Nabla operator
$\boldsymbol{\zeta}$	$[*]$	Vector of model forcings

* unit depends on application

List of Acronyms

DEnKF	Deterministic Ensemble Kalman Filter
DTS	Distributed Temperature Sensing
EKF	Extended Kalman Filter
EnKF	Ensemble Kalman Filter
EnKS	Ensemble Kalman Smoother
ES	Ensemble Smoother
KF	Kalman Filter
MC	Monte Carlo
NN	Newtonian Nudging
PF	Particle Filter
RMSE	Root Mean Square Error
SGS	Sequential Gaussian Simulation
SSC	Sequential Self Calibration

Abstract

Exchange processes between rivers and groundwater are an important driver for the hydrological, chemical and ecological environment around streams and the cycling of water at the catchment scale. Management decisions for such systems are very often derived on the basis of model predictions and it is therefore essential to properly estimate the relevant model parameters that govern the interaction between river and aquifer. Various field studies indicate that hydraulic parameters in and around streams are associated with a considerable uncertainty regarding their temporal and spatial distribution. These uncertainties have to be regarded in the estimation of hydraulic parameters and different stochastic inversion methods are available for that task. Among these methods, the Ensemble Kalman Filter (EnKF) has been proven to work well for the characterization of subsurface parameters where its advantage over other stochastic inversion techniques is the calculation of a full posterior probability density function without linearization around an optimum, its computational efficiency and its ability to be used for real-time predictions.

In this work, EnKF was applied to a 3D groundwater model of a well field within the Limmat aquifer in Zurich (Switzerland) which is strongly influenced by river-aquifer interactions. The specific aim was to investigate different aspects of the spatio-temporal characterization of river bed properties with EnKF and to explore the worth of different conditioning data for this site. In a first study, the model was used in synthetic experiments where reference runs with temporally varying river bed hydraulic conductivities were generated. Then it was tested, to what extend state-parameter updates with EnKF are able to detect these changes in river bed properties based on a limited set of piezometric head measurements from the reference simulations. In a second study, it was investigated how the spatial representation of heterogeneity influences the updating behavior of EnKF. In this case, synthetic references with spatially heterogeneous fields of river bed permeabilities were generated and piezometric head data from these references were used to update four different parameter ensembles that varied in the spatial representation of heterogeneity (i.e., fully heterogeneous versus zonated leakage parameters). In a third study, the value of a joint assimilation of piezometric head

and groundwater temperature data was first examined with a simple synthetic model of a river-aquifer system under well defined conditions. Then, the extended assimilation scheme was also tested for a historic real-world data set of the Limmat aquifer model where up to 87 piezometric head and 22 groundwater temperature measurements were available as conditioning data for EnKF on a daily basis.

Results for the assimilation experiments on the temporal variability of river bed hydraulic conductivities showed that EnKF is able to adapt time-varying model parameters under different conditions. However, the response of EnKF to changes in river bed properties was relatively slow which is related to the weighting of prediction and observation uncertainty in the EnKF updating scheme. An extension of the data assimilation algorithm with adaptive covariance inflation, a methodology to increase the ensemble variance dependent on the mismatch between simulations and observations, led to a decrease in the adaptation time and to a lower bias between true and updated parameter values.

Data assimilation experiments on the spatial variability of leakage parameters showed that EnKF is also able to identify the spatial structure of heterogeneous reference fields of leakage parameters even when there is a considerable variability in the geostatistical parameters of the initial ensemble. Results for this study also revealed that data assimilation with different ensembles of effective (i.e., spatially aggregated) leakage parameters leads to a biased estimation of exchange fluxes between river and aquifer even if groundwater levels are continuously updated. Therefore, the usage of a stochastic field approach is recommended for representing heterogeneous river bed structures as this approach was never outperformed by any of the coarser parameterizations.

Results for a joint assimilation of hydraulic and thermal data with EnKF for the synthetic river-aquifer model suggest that the additional assimilation of temperature data can generally improve the estimation of hydraulic subsurface parameters. Here, the most significant improvement was found for the reconstruction of the spatial structure of leakage parameters. Experiments with the real-world data of the Limmat aquifer showed that the prediction of groundwater temperatures could be improved by the use of thermal observation data compared to a use of hydraulic data only. However, the results did not reveal significant differences between the estimation of subsurface parameters with and without thermal data because the state predictions after the calibration for both cases were very similar.

In summary, these results show that EnKF is well suited for the characterization of spatially and temporally variable river bed hydraulic properties. Using temperature data as additional conditioning data for EnKF generally improved predictions of groundwater states which demonstrates the feasibility of EnKF for the application to real-time predictions of groundwater temperatures although the effect on parameter updates was relatively limited compared to hydraulic data.

Zusammenfassung

Austauschprozesse zwischen Flüssen und dem Grundwasser stellen eine wichtige Einflussvariable für die flussnahen hydrologischen, chemischen und ökologischen Gegebenheiten dar und beeinflussen zudem den Wasserkreislauf auf Einzugsgebietsebene. Managemententscheidungen für solche Systeme werden häufig auf der Grundlage von Modellvorhersagen getroffen, was eine adäquate Bestimmung der relevanten Modellparameter für Fluss-Grundwasser-Interaktionen unabdingbar macht. Verschiedene Studien haben gezeigt, dass die hydraulischen Eigenschaften des Flussbettes durch ein hohes Maß an Unsicherheit bezüglich ihrer zeitlichen und räumlichen Verteilung geprägt sind. Diese Unsicherheiten müssen bei der Abschätzung hydraulischer Parameter mit in Betracht gezogen werden, wobei verschiedene stochastische Inversionsverfahren für diese Aufgabe zur Verfügung stehen. Unter diesen Methoden hat der Ensemble Kalman Filter (EnKF) seine Tauglichkeit hinsichtlich der Charakterisierung von Untergrundparametern bewiesen, wobei seine Vorzüge gegenüber anderen stochastischen Verfahren darin begründet sind, dass er die vollständige a posteriori Wahrscheinlichkeit ohne eine Linerarisierung um ein Optimum bestimmt, weniger rechenintensiv ist und für Echtzeitanwendungen verwendet werden kann.

In dieser Arbeit wurde EnKF für ein 3D Grundwassermodell eines Brunnenfeldes innerhalb des Limmat Aquifers in Zürich (Schweiz) verwendet, welches sehr stark durch Fluss-Grundwasser-Interaktion beeinflusst wird. Ein wesentliches Ziel dieser Arbeit war die Untersuchung verschiedener Aspekte der räumlich-zeitlichen Charakterisierung von Flussbetteigenschaften durch EnKF sowie die Erfassung des Informationsgewinns verschiedener Konditionierungsdaten für das Untersuchungsgebiet. In einer ersten Studie wurde das Modell für synthetische Experimente verwendet, in denen Referenzsimulationen mit zeitlich variablen hydraulischen Flussbettleitfähigkeiten erstellt wurden. Dabei wurde untersucht, in welchem Maße Aktualisierungen der Zustandsvariablen und Parameter durch EnKF in der Lage sind, diese Änderungen der Flussbettleitfähigkeiten durch

eine limitierte Anzahl von Piezometerdaten aus den Referenzsimulationen nachzuvollziehen. In einer zweiten Studie wurde untersucht, wie die räumliche Repräsentation von Heterogenität das Anpassungsverhalten von EnKF beeinflusst. In diesem Fall wurden synthetische Referenzen mit räumlich heterogenen Flussbettpermeabilitätsfeldern erzeugt und Piezometerdaten dieser Referenzen wurden im Weiteren verwendet, um vier verschiedene Ensemble zu aktualisieren, die sich hinsichtlich der räumlichen Repräsentation der Heterogenität (vollkommen heterogen vs. zoniert) unterschieden. In einer dritten Studie wurde der Informationsgewinn einer simultanen Assimilierung von Piezometer- und Grundwassertemperaturdaten zunächst für ein synthetisches Fluss-Aquifermodell unter wohldefinierten Bedingungen getestet. Im Folgenden wurde dieses erweiterte Assimilierungsschema auch für historische reale Daten des Limmatgrundwassermodells getestet, wobei bis zu 87 Grundwasserspiegel- und 22 Grundwassertemperaturmessungen als Konditionierungsdaten auf täglicher Basis zur Verfügung standen.

Die Ergebnisse für die Assimilierungsexperimente zur zeitlichen Variabilität der Flussbettleitfähigkeiten konnten zeigen, dass EnKF dazu in der Lage ist, zeitlich variable Modellparameter unter verschiedenen Bedingungen anzupassen. Die Anpassungszeiten waren dabei jedoch relativ lange, was auf die Gewichtung von Vorhersage- und Messfehlern in der Anpassungsroutine von EnKF zurückzuführen ist. Eine Erweiterung des Assimilierungsschemas von EnKF durch adaptive Kovarianzinflation, einer Methode zur Erhöhung der Ensemble-Varianz anhand der Residuen zwischen Vorhersage und Messung, führte zu einer Verringerung der Anpassungszeit und einem geringeren Fehler zwischen angepassten und wahren Parameterwerten.

Datenassimierungsexperimente bezüglich der räumlichen Variabilität von Leakageparametern zeigten, dass EnKF auch in der Lage ist, die räumliche Struktur heterogener Referenzfelder zu identifizieren, selbst wenn eine beträchtliche Variabilität bezüglich der geostatistischen Parameter des Anfangsensembles vorhanden war. Die Ergebnisse dieser Studie zeigten zudem, dass Datenassimilierung mit verschiedenen Ensemblen effektiver (räumlich aggregierter) Leakageparameter zu einer systematischen Fehlinterpretation der Austauschflüsse zwischen Fluss und Grundwasserleiter führen kann, selbst wenn die Grundwasserstände kontinuierlich angepasst werden. Aus diesem Grund wird empfohlen, heterogene Flussbettstrukturen durch stochastischen Felder zu repräsentieren da dieser Ansatz im Vergleich zu niedriger aufgelöster Parametrisierungen stets die besten Ergebnisse erzielte.

Ergebnisse für die gleichzeitige Assimilierung hydraulischer und thermischer Daten mit EnKF für das synthetische Fluss-Grundwasser-Modell lassen darauf schließen, dass die zusätzliche Assimilierung von Temperaturdaten generell zu einer verbesserten Schätzung von hydraulischen Aquifereigenschaften führen kann. Dabei wurden die signifikantesten Verbesserungen bei der Rekonstruktion der räumlichen Struktur der Leakagaparameter beobachtet. Experimente mit den realen Daten des Limmatgrundwasserleiters zeigten,

dass die Vorhersage von Grundwassertemperaturen durch die Verwendung der thermischen Beobachtungsdaten, im Vergleich zur ausschließlichen Verwendung von hydraulischen Daten, verbessert werden konnte. Jedoch konnten keine signifikante Unterschiede bezüglich der Abschätzung hydraulischer Parametern hinsichtlich der Verwendung/ Nichtverwendung von thermischen Daten gefunden werden, da nach der Kalibrierung in beiden Fällen die Vorhersage der Zustandsgrößen relativ ähnlich war.
Zusammenfassend lässt sich feststellen, dass EnKF sehr gut dazu geeignet ist, räumlich und zeitlich variable Flussbetteigenschaften zu charakterisieren. Die Verwendung von Temperaturdaten als eine zusätzliche Informationsquelle führte zu einer verbesserten Vorhersage der Zustandsgrößen des Grundwassers. Dies zeigt, dass diese Methode prinzipiell für die Verwendung in Echtzeitsystemen zur Abschätzung von Temperaturfeldern geeignet ist, obwohl im Vergleich zur Assimilierung hydraulischen Daten nur ein begrenzter Einfluss auf die Parameterabschätzung festgestellt werden konnte.

Chapter 1

Introduction

Water resources are increasingly threatened by pollution and overexploitation. In order to cope with the challenges for maintaining healthy water resource conditions there is an increasing need for a deeper understanding of processes that drive the terrestrial water cycle and the ability to properly predict the future evolution of the quantity and quality of available water resources. In this sense, surface water bodies, like rivers and lakes, as well as groundwater are of special interest. These two compartments of the terrestrial water cycle have long been treated as separate entities but in the last decades there was growing awareness that they are closely linked (Bouwer and Maddock, 1997; Winter, 1999; Sophocleous, 2002) which is also reflected in the increasing research interest in this area (Fleckenstein et al., 2010). The interaction between streams and the groundwater body is driven and influenced by different variables which include the hydraulic gradient between river level and groundwater, dynamics and spatial distribution of the river bed sediments (Schälchli, 1992; Blaschke et al., 2003; Genereux et al., 2008), geomorphological aspects of the river bed (Boano et al., 2006; Cardenas et al., 2004) as well as the state of hydraulic connection between river and groundwater (Brunner et al., 2009). The increasing research interest in river-aquifer exchange is owed to the various processes that occur in the transition zone (or hyporheic zone) between surface water and groundwater which influence the hydrological, chemical and biological environment around streams. In the hyporheic zone, water of different chemical composition gets mixed which drives a variety of biogeochemical transformation processes. It has also been shown that various aquatic species adapt their life cycle to the physico-chemical conditions that arise through river-aquifer exchange (e.g., Brunke and Gonser, 1997). The hydraulic connection between rivers and groundwater also facilitates the transfer of contaminants from one compartment to the other. For example, micro pollutants, such as pharmaceuticals, can be detected in rivers because they are not transformed during passage of waste water treatment plants. These contaminants can then pose a thread

to the drinking water supply close to rivers (e.g., Heberer, 2002). The opposite contamination pathway holds true for nitrate which can be transferred from groundwater to surface water via hyporheic exchange (e.g., Kennedy et al., 2009) which can induce environmental problems for river ecology. Especially for groundwater management also the hydraulic aspects of river-aquifer interactions play an important role because exchange fluxes between surface water and groundwater largely influence the regional water balance and the groundwater flow around streams (Woessner, 2000). For example, river bank filtration is commonly used in Europe to maintain a sustainable use of groundwater resources and the transition of river water through the river sediment towards pumping wells is also used as a purification step to remove unwanted pathogens and micro pollutants from the river water (e.g., Tufenkji et al., 2002; Schubert, 2002). Such techniques of course depend on the hydraulic properties of the river sediment and river stage fluctuations (Schubert, 2002; Zhang et al., 2011; Wett et al., 2002).

For such medium to large scale systems it is essential to have a reliable estimate on the hydraulic parameters of the river bed and the adjacent aquifer. Although there are different field methods available to estimate hydraulic parameters (see e.g., Kalbus et al., 2006) it is often unaffordable for management authorities to apply such methods for their larger scale systems. A commonly used method for such systems are modeling approaches where the relevant hydraulic model parameters are estimated through calibration and the calibrated model is then used for predicting the system response for future times. However, the morphogenesis of fluvial deposits is usually very complex and can exhibit a high degree of spatial heterogeneity which is often largely unknown for the calibration of groundwater models. Also within an existing river bed there are spatially and temporally varying deposition and erosion processes which also depend on the sediment load and discharge behavior of the river under question. As a result of these various processes, parameter estimation around streams can be highly uncertain. Generally, there are different inversion techniques available for distributed hydrological models (Zimmerman et al., 1998; Hendricks Franssen et al., 2009) which can be roughly divided into two classes: (I) deterministic methods that provide a single best solution for the inversion problem and (II) stochastic inversions which also try to include the uncertainty of different variables in the inversion process. Regarding the high parameter uncertainty that is associated with fluvial systems it would be a natural choice to use stochastic inversion techniques. A very attractive method in this sense is sequential data assimilation with the Ensemble Kalman Filter (EnKF). For this method an ensemble of uncertain parameter sets and model forcings is simulated forward in time. At times when measurements of model variables are available, EnKF adapts the model states and parameters to provide a better fit between predictions and measurements. This method offers a high flexibility for the incorporation of different sources of uncertainty and is

relatively easy to implement. Moreover, through its sequential updating scheme it is well suited for systems in which state variables are continuously monitored which is often the case for groundwater management sites. An example of such a system is the operation of a well field within the Limmat aquifer in Zurich (Switzerland). At this site, different measures are undertaken to ensure a sustainable use of groundwater resources and to prevent a contamination of drinking water wells from diffuse contamination sources. This is done by extracting water close to the river Limmat and recharging this water to the aquifer through several recharge wells and recharge basins. This artificial recharge aims to provide a sufficient water supply to the drinking water wells and to protect them from a diffuse contamination outside the well field. A dense monitoring network of groundwater levels is available for this site which makes it very suitable for the application of EnKF. Only recently, a real-time modeling system was set up for this site where EnKF is used to continuously correct model predictions and parameters with real-time data from the monitoring network (Hendricks Franssen et al., 2011). These real-time predictions are then also used for the real-time control of the well field (Bauser et al., 2010). As this system is strongly influenced by river-aquifer exchange it provides an excellent test bed to investigate the capability of EnKF to deal with the spatio-temporal variability of river bed hydraulic properties and will be used throughout this work. Apart from piezometric head observations also groundwater temperatures are monitored continuously at this site. Especially for river-groundwater systems temperature data have recently gained attention as a valuable source of information regarding the exchange processes between rivers and aquifers. The reason is that river temperatures typically follow a seasonal cycle with a high amplitude whereas groundwater temperatures are usually rather constant throughout the year. As a consequence, a temperature signal from the river is propagated into the aquifer in case of infiltrating conditions (with respect to the aquifer). For the opposite case when the aquifer discharges into the river, the temperature contrasts underneath the river bed will be dampened compared to infiltrating conditions. Therefore, measured temperature profiles underneath the river can be deployed to characterize the exchange fluxes as well as relevant material properties of the river bed and the adjacent aquifer (Anderson, 2005; Constantz, 2008). As it is relatively straightforward to incorporate additional types of measurements in EnKF the monitored groundwater temperatures at the Limmat aquifer could be utilized as an additional source of information for the characterization of subsurface parameters. For this site there is also an interest from groundwater authorities to gain reliable predictions of the temperature distribution around the drinking water wells. This is of special interest because the extraction of water that is too warm can negatively influence drinking water quality due to microbial contamination which then needs to be accounted for by disinfection measures.

The general aim of this work is to explore the possible advantages and limitations of using sequential data assimilation with EnKF to improve the prediction of groundwater states close to streams and to estimate the relevant hydraulic parameter that drive the exchange between rivers and groundwater. Before presenting the different conducted numerical experiments in detail, Chapter 2 gives a short overview over the governing equation of groundwater flow, heat transport and river-aquifer exchange. Furthermore, this chapter introduces the basic data assimilation scheme of EnKF and provides a short literature review on the application of EnKF in groundwater hydrology. In Chapter 3 the capability of EnKF to detect and adapt to temporal changes of hydraulic subsurface parameters is investigated with synthetic experiments. For these numerical experiments different virtual realities for temporal changes of river bed properties are generated on the basis of the 3D groundwater model of the Limmat aquifer. Piezometric head data from these synthetic realities (or references) are then used in data assimilation experiments with EnKF and it is evaluated to which extend EnKF is able to correct model parameters towards the temporal dynamics of river bed properties that were assigned in the synthetic reference runs. In Chapter 4 a similar model setup as in Chapter 3 is used but the focus is more on the spatial variability of river bed properties. Here, the aim is to explore whether EnKF is able to identify the heterogeneous spatial structure of leakage parameters through the assimilation of piezometric head data. A further goal is to investigate the consequences of using effective leakage parameters to characterize highly heterogeneous streambeds with EnKF. In Chapter 5 it is tested to what extent the additional assimilation of groundwater temperatures with EnKF can provide further information for the characterization of subsurface parameters. This is done with coupled flow and heat transport calculations for two types of experiments. First, synthetic experiments with a relatively simple model setup for a river-aquifer system are used to identify the principal capabilities of a joint assimilation of hydraulic and thermal data with EnKF. In a second step, assimilation experiments with real-world data for the Limmat aquifer are conducted. Finally, Chapter 6 synthesizes the outcomes of the different experiments and provides some thoughts for further research directions.

Chapter 2

Theory

2.1 Flow and heat transport in porous media

The following section tries to give a short overview over the governing equations of flow and heat transport in porous media and the coupling of groundwater and surface water. This short summary is based on information from Domenico and Schwartz (1990) and Bear and Chen (2010).

Groundwater flow

Groundwater flow is governed by potential gradients where the potential is usually expressed as piezometric head:

$$h = z + \frac{p}{\rho_w g} \tag{2.1}$$

where h is piezometric head [L], z is height above datum [L], p is pressure [$\mathrm{ML^{-1}T^{-2}}$], ρ_w is density of water [$\mathrm{ML^{-3}}$] and g is gravitational acceleration [$\mathrm{LT^{-2}}$].

Groundwater flux can be calculated according to Darcy's law as:

$$v = -K\nabla h = -\frac{\rho_w g k}{\mu}\nabla h \tag{2.2}$$

where v is groundwater flow velocity [$\mathrm{LT^{-1}}$], K is hydraulic conductivity [$\mathrm{LT^{-1}}$], μ is dynamic viscosity [$\mathrm{ML^{-1}T^{-1}}$], k is permeability [$\mathrm{L^2}$] and ∇ is Nabla operator in three dimensions [$\mathrm{L^{-1}}$].

The mass balance for an infinitesimal control volume is given as:

$$\frac{1}{\rho_w}\frac{\partial(n\rho_w)}{\partial t} = S_s\frac{\partial h}{\partial t} = -\nabla v + \frac{q_f}{\rho_w} \tag{2.3}$$

where q_f is a source/ sink term [$\mathrm{ML^{-3}T^{-1}}$], n is porosity [$-$] and S_s is specific storativity [$\mathrm{L^{-1}}$].

Inserting Equation 2.2 into Equation 2.3 gives the groundwater flow equation for saturated conditions:

$$S_s\frac{\partial h}{\partial t} = \nabla\left(\frac{\rho_w g k}{\mu}\nabla h\right) + \frac{q_f}{\rho_w} \tag{2.4}$$

Unsaturated flow

For unsaturated conditions Equation 2.4 has to be modified in order to account for the saturation dependent reduction of hydraulic conductivity:

$$\frac{\partial(n\rho_w S(\theta))}{\partial t} = \nabla\left(\frac{\rho_w k k_r(\theta)}{\mu}(\nabla p + \rho_w g \nabla z)\right) + q_f \tag{2.5}$$

where θ is water content [$\mathrm{L^3L^{-3}}$], $S(\theta)$ is saturation [$-$] and $k_r(\theta)$ is relative permeability [$-$].

In hydrology the most common parameterization to derive $k_r(\theta)$ is the Mualem-van Genuchten model (van Genuchten, 1980):

$$k_r(\theta) = \hat{\theta}^l\left(1 - (1 - \hat{\theta}^{\frac{n_p}{n_p-1}})^{\frac{n_p-1}{n_p}}\right)^2 \tag{2.6a}$$

$$\hat{\theta} = \frac{\theta - \theta_r}{\theta_s - \theta_r} \tag{2.6b}$$

where $\hat{\theta}$ is a normalized water content [$\mathrm{L^3L^{-3}}$], θ_r is residual water content [$\mathrm{L^3L^{-3}}$], θ_s is saturated water content [$\mathrm{L^3L^{-3}}$], l is an empirical parameter [$-$] and n_p is pore size index [$-$].

Heat transport

Heat transport in porous media is driven by three processes: heat conduction, hydrodynamic dispersion and heat advection. For reasons of simplicity, heat transport in the gas phase is neglected in the following description. Heat conduction through a porous medium is then described by Fourier's law as:

$$j_m = -((1-n)\kappa_s + \theta\kappa_w)\nabla T \tag{2.7}$$

where j_m is heat flux through molecular conduction [MT^{-3}], κ_s is thermal conductivity of solid material [$\mathrm{ML\Theta}^{-1}\mathrm{T}^{-3}$], κ_w is thermal conductivity of water [$\mathrm{ML\Theta}^{-1}\mathrm{T}^{-3}$], θ is water content [$\mathrm{L}^3\mathrm{L}^{-3}$], n is porosity [$-$] and T is temperature [Θ].

Advective heat transport is given as:

$$j_a = c_w \rho_w T v \tag{2.8}$$

where j_a is advective heat flux [MT^{-3}], v is groundwater flow velocity [MT^{-1}] and c_w is specific heat capacity of water [$\mathrm{L}^2\mathrm{T}^{-2}\Theta^{-1}$].

Hydrodynamic dispersion can be expressed as:

$$j_d = -\rho_w c_w D \nabla T \tag{2.9}$$

where j_d is heat flux due to hydrodynamic dispersion [MT^{-3}] and D is the dispersion coefficient [$\mathrm{L}^2\mathrm{T}^{-1}$].

Balancing the given heat fluxes j_m, j_a and j_d for a control volume and taking into account other source/sink terms and storage of heat, the heat transport equation is derived as:

$$\frac{\partial {c_v}^* T}{\partial t} = -\nabla(\rho_w c_w v T) + \nabla({\kappa_v}^* \nabla T) + \nabla(\rho_w c_w D \nabla T) + q_h \tag{2.10a}$$

$${c_v}^* = (1-n)\rho_s c_s + \theta \rho_w c_w \tag{2.10b}$$

$${\kappa_v}^* = (1-n)\kappa_s + \theta \kappa_w \tag{2.10c}$$

where q_h are thermal source/ sink terms [$\mathrm{ML}^{-1}\mathrm{T}^{-3}$], ρ_s is substance density of solid material [ML^{-3}] and c_s is specific heat capacity of solid material [$\mathrm{L}^2\mathrm{T}^{-2}\Theta^{-1}$].

Coupling of surface water and groundwater

A very common approach for calculating the exchange between river and aquifer is a Cauchy-type boundary condition:

$$Q_{leak} = A_{leak} L (h^{river} - h^{gw}) \tag{2.11}$$

where Q_{leak} is the leakage flux between river and aquifer [$\mathrm{L}^3\mathrm{T}^{-1}$], A_{leak} is the surface area through which the leakage flux occurs [L^2], h^{river} is river stage [L], h^{gw} is groundwater level underneath the river [L] and L is leakage coefficient [T^{-1}] which is a lumped parameter for the hydraulic conductivity and the thickness of the river bed.

This approach is implemented in many popular groundwater modeling codes and often certain restriction can be applied to this type of boundary conditions. For example, a maximal infiltration rate can be specified either directly or by restricting the maximal head difference between river and aquifer. This is often done to account for the development of an unsaturated zone underneath the river bed. Another type of modification is to apply an anisotropy ratio for the fluxes with respect to flux direction. In recent years the development of model codes also moved towards more physically based coupling of surface and subsurface equations where the routing of surface water flow is directly linked to the Richards equation in the subsurface compartment (e.g., VanderKwaak and Loague, 2001; Panday and Huyakorn, 2004; Kollet and Maxwell, 2006). Brunner et al. (2010) compared the popular groundwater modeling software MODFLOW (which basically utilized the leakage principle of Equation 2.11) and the physically based coupled surface-subsurface model HydroGeoSphere with respect to the coupling of surface water and groundwater. They point out that the discretization of model cells, the representation of connectivity between surface water and groundwater and the disregarding of negative pressure heads in MODFLOW can bias the prediction of river-aquifer exchange fluxes compared to the physically based coupling approach of HydroGeoSphere.

2.2 Data assimilation with the Ensemble Kalman Filter

The Ensemble Kalman Filter (EnKF) is a sequential data assimilation approach which can be utilized to improve the prediction capability of a particular model in a stochastic framework. EnKF is an advancement of the famous Kalman Filter (KF) (Kalman, 1960) which overcomes some limitations of KF in high-dimensional non-linear geophysical systems. In KF an uncertain model prediction is adjusted with uncertain measurements by weighting both types of uncertainty so that the variance of the adjusted model prediction is minimized. In the KF filtering scheme errors are assumed to be Gaussian and the filter yields the best linear unbiased estimator in case of linear model dynamics. For nonlinear model dynamics the Extended Kalman Filter (EKF) is an alternative. In EKF the forward propagation of the covariance matrix is approximated by a Taylor series and higher order terms are neglected which makes EKF suitable for moderately nonlinear problems. In both filtering schemes (KF and EKF) an explicit forward propagation of the covariance matrix is needed which makes both methods computationally unaffordable for large scale geophysical systems (Evensen, 2003).

In EnKF an ensemble of model realizations (e.g., with different initial conditions, forcings or parameters) is used to approximate the evolution of error statistics. The different ensemble members are propagated forward in time with a model M:

$$\boldsymbol{\psi}_i^t = M(\boldsymbol{\psi}_i^{t-1}, \boldsymbol{\phi}_i, \boldsymbol{\zeta}_i) \tag{2.12}$$

where $\boldsymbol{\psi}_i^t$ is the state vector for the current time step (i.e., the forecast), $\boldsymbol{\psi}_i^{t-1}$ is the state vector for the previous time step, $\boldsymbol{\phi}_i$ are model parameters and $\boldsymbol{\zeta}_i$ are model forcings for realization i.

For each assimilation cycle (i.e., at times when measurements become available) EnKF then performs a Bayesian update on the ensemble of the state vector $\boldsymbol{\psi}^t$:

$$p(\boldsymbol{\psi}^t \mid \boldsymbol{y}^0) \propto p(\boldsymbol{y}^0 \mid \boldsymbol{\psi}^t) p(\boldsymbol{\psi}^t) \tag{2.13}$$

where $p(\boldsymbol{\psi}^t \mid \boldsymbol{y}^0)$ is the posterior (updated) distribution of the state vector $\boldsymbol{\psi}^t$ given the observations $\boldsymbol{y}^0$, $p(\boldsymbol{y}^0 \mid \boldsymbol{\psi}^t)$ is the likelihood of measurements $\boldsymbol{y}^0$ given $\boldsymbol{\psi}^t$ and $p(\boldsymbol{\psi}^t)$ is the prior distribution of $\boldsymbol{\psi}^t$.

The prior of the states $\boldsymbol{\psi}^t$ in Equation 2.13 is obtained by advancing each realization i of the ensemble with the model M of Equation 2.12 assuming a first-order Markov process. The posterior distribution of $\boldsymbol{\psi}^t$ in Equation 2.13 is then calculated with the EnKF analysis scheme which consists of the following steps: First, the forecasted values of $\boldsymbol{\psi}^t$ at observation points have to be extracted from the ensemble for each realization i:

$$\hat{\boldsymbol{\psi}}_{\boldsymbol{i}}^{\boldsymbol{t}} = \mathbf{H}\boldsymbol{\psi}_{\boldsymbol{i}}^{\boldsymbol{t}} \tag{2.14}$$

where $\hat{\boldsymbol{\psi}}^t$ is the state vector at observation points and $\mathbf{H}$ is a matrix that maps or interpolates the whole state vector $\boldsymbol{\psi}^t$ on the observation points.

Next, the measured states $\boldsymbol{y}^0$ have to be perturbed for an optimal functioning of the data assimilation algorithm in order to achieve the correct posterior variance (Burgers et al., 1998). This is done with the perturbation vector $\tilde{\boldsymbol{\epsilon}}$ which is composed of values drawn from a normal distribution $\mathcal{N}(0, \epsilon)$ with a mean of zero and a standard deviation that corresponds to the measurement error ϵ of the assimilated state variable:

$$\tilde{\boldsymbol{y}}_i = \boldsymbol{y}^0 + \tilde{\boldsymbol{\epsilon}}_i \tag{2.15}$$

where $\tilde{\boldsymbol{y}}_i$ is the perturbed measurement vector for realization i, $\tilde{\boldsymbol{\epsilon}}_i$ is the corresponding perturbation vector and $\boldsymbol{y}^0$ is the measurement vector.

Finally, the posterior distribution of $\boldsymbol{\psi}^t$ is found by applying the following equation on each ensemble member i:

$$\boldsymbol{\psi}_i^{\boldsymbol{a}} = \boldsymbol{\psi}_i^{\boldsymbol{t}} + \mathbf{G}(\tilde{\boldsymbol{y}}_i - \hat{\boldsymbol{\psi}}_i^{\boldsymbol{t}}) \tag{2.16}$$

where $\boldsymbol{\psi}_i^{\boldsymbol{a}}$ is the analyzed (updated) state vector for realization i, $\boldsymbol{\psi}_i^{\boldsymbol{t}}$ is the forecasted state vector (from Equation 2.12), $\tilde{\boldsymbol{y}}_i$ is the perturbed measurement vector (from Equation 2.15), $\hat{\boldsymbol{\psi}}_i^{\boldsymbol{t}}$ is the state vector at observation points (from Equation 2.14) and $\mathbf{G}$ is the Kalman gain matrix which is calculated as:

$$\mathbf{G} = \mathbf{C}\mathbf{H}^\top(\mathbf{H}\mathbf{C}\mathbf{H}^\top + \mathbf{R})^{-1} \tag{2.17}$$

where $\mathbf{C}$ is the full covariance matrix of $\boldsymbol{\psi}^t$ and $\mathbf{R}$ is the covariance matrix of observation data $\boldsymbol{y}^0$. The Kalman gain $\mathbf{G}$ is calculated once for all ensemble members and weights the uncertainties in the prediction of $\boldsymbol{\psi}^t$ from the forward simulations with the measurement error of $\boldsymbol{y}^0$. In the analysis step (Equation 2.16) the weighting factors of $\mathbf{G}$ are used to correct each member of $\boldsymbol{\psi}^t$ with the residuals at observation points (bracketed term in Equation 2.16). $\mathbf{R}$ is usually inferred from the measurement error of the state variable that is assimilated. The diagonal elements of $\mathbf{R}$ then represent the variance of the measured state variable for each observation point and the off-diagonal elements represent the covariances of the measured state variables between different observation points. In order to derive $\mathbf{G}$ it is not necessary to calculate the full covariance matrix of $\boldsymbol{\psi}^t$ but it is sufficient to calculate the covariances between $\boldsymbol{\psi}^t$ and $\hat{\boldsymbol{\psi}}^t$:

$$\mathbf{C}\mathbf{H}^\top = \mathbf{C}_{\boldsymbol{\psi}^t\hat{\boldsymbol{\psi}}^t} \tag{2.18}$$

Various variants of the EnKF analysis scheme exist in literature. One important class are smoothers like the Ensemble Smoother (ES) (van Leeuwen and Evensen, 1996) and the Ensemble Kalman Smoother (EnKS) (Evensen and van Leeuwen, 2000). In these applications the information of a specific measurement in time is also used to improve the prediction for previous time steps, i.e. information is also propagated backward in time. Another important variant of EnKF are Deterministic Ensemble Kalman Filters (DEnKFs) (Bishop et al., 2001; Anderson, 2001; Whitaker and Hamill, 2002; Tippett et al., 2003). These filters avoid the perturbation of the measurement vector $\boldsymbol{y}^0$ (Equation 2.15) which has been shown to be superior for some applications.

EnKF has been extensively used in atmospheric and oceanographic applications (for a comprehensive overview see Evensen (2009, p.279ff)). It has also been used in hydrological applications like surface water modeling, radiative transfer modeling, in landsurface-atmosphere modeling and in groundwater modeling (Montzka et al., 2012; Aanonsen et al., 2009). Applications of EnKF in groundwater modeling and subsurface characterization are shortly outlined in the following section.

2.3 Usage of EnKF in subsurface characterization

EnKF and its variants have already been applied successfully for the characterization of uncertain state variables and subsurface parameters. First applications are found in the petroleum engineering literature (e.g., Lorentzen et al., 2003; Naevdal et al., 2005) and EnKF was introduced slightly later in groundwater applications (e.g., Chen and Zhang, 2006; Hendricks Franssen and Kinzelbach, 2008; Nowak, 2009). In subsurface models a high degree of uncertainty comes from the poorly known parameter fields as opposed to atmospheric models where especially initial conditions are uncertain. Therefore, in subsurface models EnKF is also applied to estimate uncertain model parameters. This is usually achieved by an augmented state vector approach (e.g., Chen and Zhang, 2006; Hendricks Franssen and Kinzelbach, 2008), i.e. the state vector $\boldsymbol{\psi}$ is augmented with the unknown model parameters $\boldsymbol{\phi}$ which gives the combined state-parameter vector $\boldsymbol{\Psi}$:

$$\boldsymbol{\Psi} = \begin{pmatrix} \boldsymbol{\psi} \\ \boldsymbol{\phi} \end{pmatrix} \tag{2.19}$$

The analysis equation in the EnKF filtering scheme (Equation 2.16) is then applied with the augmented state vector $\boldsymbol{\Psi}$ instead of the state vector $\boldsymbol{\psi}$:

$$\boldsymbol{\Psi}_i^a = \boldsymbol{\Psi}_i^t + \mathbf{G}(\tilde{\boldsymbol{y}}_i - \mathbf{H}\boldsymbol{\Psi}_i^t) \tag{2.20}$$

The covariance matrix for the simultaneous update of states and parameters is composed of the covariances between simulated states $\boldsymbol{\psi}^t$ and simulated states at observation points $\hat{\boldsymbol{\psi}}^t$ and the covariances between parameters $\boldsymbol{\phi}$ and simulated states at observation points:

$$\mathbf{C}\mathbf{H}^\top = \begin{pmatrix} \mathbf{C}_{\boldsymbol{\psi}^t\hat{\boldsymbol{\psi}}^t} \\ \mathbf{C}_{\boldsymbol{\phi}\hat{\boldsymbol{\psi}}^t} \end{pmatrix} \tag{2.21}$$

In Chen and Zhang (2006) and Hendricks Franssen and Kinzelbach (2008) the assimilation of piezometric head measurements with EnKF led to an improved estimate of

hydraulic conductivity fields with the joint state-parameter update. Nowak (2009) proposed a slightly different approach to estimate hydraulic conductivities with EnKF. In this version of EnKF, which is called p-space EnKF, only the model parameters are updated with measurements of state variables and a rerun step is needed to ensure the consistency between updated parameters and simulated state variables. In Hendricks Franssen et al. (2011) EnKF was applied for a managed river-aquifer system (Limmat aquifer Zurich) where piezometric heads were jointly updated with hydraulic conductivities and leakage parameters. They applied EnKF to real-world data and showed that a combined update of piezometric heads and model parameters provides better predictions of groundwater levels than an assimilation of piezometric head data alone. Synthetic experiments with the same model also emphasized that the estimation of hydraulic model parameters can be improved through the assimilation of piezometric head data.

Besides the assimilation of piezometric heads EnKF has also been applied with other types of measurement data to infer subsurface parameters: Liu et al. (2008) used a joint assimilation of piezometric heads and concentration data to estimate hydraulic conductivities at the MADE site. Li et al. (2012) used piezometric head and tracer data to jointly infer hydraulic conductivity and porosity fields. They found that an additional assimilation of tracer data further improves the estimated parameter fields and that the assimilation of piezometric head data alone has only a limited effect on the estimation of concentration data. In Camporese et al. (2009b) the assimilation of piezometric heads and/or discharge data was compared for a process based coupled surface-subsurface model in terms of prediction of state variables (piezometric heads and discharge). They found that the assimilation of piezometric heads as well as the joint assimilation of piezometric heads and discharge data led to a better prediction of the system state whereas an assimilation of discharge data alone only gave poor results.

The impact of uncertainties in the initial parameter ensemble on the performance of EnKF was investigated by Jafarpour and Tarrahi (2011) and Huber et al. (2011). Jafarpour and Tarrahi (2011) found that a bias in the geostatistical parameters for generating initial parameter ensembles often persist throughout the application of EnKF which was especially pronounced for the direction of major continuity and the integral scale of the parameter fields. They also showed that an overestimation of the variability of geostatistical parameters for the generation of the initial ensemble leads to better filtering results. They also estimated geostatistical parameters directly with EnKF and found that this procedure does not lead to improvements in subsurface characterization. In Huber et al. (2011) the performance of EnKF for state estimation was compared for different initial parameter ensembles. The ensembles were generated on the basis of different deterministic calibrations of the parameter field (no calibration, steady state,

transient with different amounts of observation data) and thus differed in the amount of prior information regarding the parameters. They found that assimilation of piezometer data further improved the predictions of the different ensembles. The best results were obtained for the ensembles where a calibration with transient data was performed and for these ensembles the errors decreased with an increasing number of conditioning data for the inversion.

Several studies compared EnKF with other stochastic inversion techniques. Camporese et al. (2009a) compared EnKF with Newtonian Nudging (NN) (Davies and Turner, 1977) for a coupled surface-subsurface flow model with respect to state estimation. In this application EnKF gave better results than NN but at a higher computational cost. Hendricks Franssen and Kinzelbach (2009) compared EnKF with Sequential Self Calibration (SSC) (Sahuquillo et al., 1992), a Monte Carlo (MC) based inversion technique, and found that both methods yield a similar performance with respect to characterizing heterogeneous hydraulic conductivity fields. In terms of computational efficiency EnKF was about 80 times faster than SSC. Pasetto et al. (2012) compared EnKF with the Particle Filter (PF) (van Leeuwen, 2009) for state estimation of pressure head and discharge for a synthetic tilted V-catchment problem. They observed that both methods achieve good prediction results. However, PF outperformed EnKF for the solely assimilation of stream flow data when a non-linear model response in the vadose zone was present.

Different authors also applied variants of EnKF in groundwater hydrology. For example, Bailey and Bau (2010) and Bailey et al. (2012) applied ES for the estimation of hydraulic conductivity fields. Sun et al. (2009) compared the performance of different DEnKFs for subsurface characterization. Liang et al. (2009) used a variant of EnKF in which the different ensemble members were weighted according to their deviation from the measured states.

An important issue in the application of EnKF in subsurface characterization is the assumption of Gaussian error statistics in the EnKF updating scheme. Aquifer properties are often assumed to follow a multi-Gaussian distribution although this does often not reflect the true aquifer properties, e.g., with respect to the connectivity structure within the aquifer (Gómez-Hernández and Wen, 1998; Zinn and Harvey, 2003; Kerrou et al., 2008). Therefore, the application of more realistic geostatistical models of subsurface structure is often advocated. Zhou et al. (2011) applied EnKF for an ensemble of hydraulic conductivity fields that was generated on the basis of multiple point geostatistics and was composed of two distinct facies. Thus, the initial parameter ensemble followed a bimodal distribution which converged towards a Gaussian distribution through the assimilation with EnKF. They proposed the usage of a normal-score transform which converts the non-Gaussian parameter distribution to a Gaussian one for the assimilation

step. They found that this technique preserves the bimodal parameter distribution and yields better results than the traditional EnKF. Similar results were found by Schöniger et al. (2012) who applied a similar technique to hydraulic tomography with piezometric head and concentration data. However, in this case, parameter fields were Gaussian and only model states were transformed for the EnKF analysis step.

Several authors also stressed the need for applying localization techniques in the updating scheme of EnKF. The rationale behind localization is to restrict the influence of observation points in space because each observation point only has a certain area of influence around itself. Model variables beyond this area are then not updated with measurements from this observation point. When the ensemble size is large enough the area of influence of a single observation point is usually well constrained through the ensemble and covariances for very distant points from a measurement location tend to zero. However, when the ensemble size is limited, spurious correlations may occur in the covariance matrix because the parameter space is not covered well enough by the ensemble. As a consequence, locations that are out of the area of influence of an observation point may be updated by EnKF due to these spurious correlations although there is not a true physical relationship between these locations and the observation point. A very common approach for localization is to apply a Schur product (i.e., an element wise multiplication of two matrices) to the covariance matrix directly before the updating equation. The localization matrix with which the covariance matrix is multiplied contains a value between 0 and 1 for each element of the covariance matrix and these values are calculated from a predefined localization function that defines the influence of a measurement point in space. Nan and Wu (2011) compared six different localization functions and found that localization improves the prediction capability of EnKF especially for small ensembles. Localization also helped to maintain a certain ensemble variance, i.e., the effect of filter divergence was reduced. Chen and Oliver (2010) also found that the application of distance-dependent localization schemes improves data assimilation with EnKF. They also argue that different types of data need different localization functions and that localization is easier for state variables than for parameters. Devegowda et al. (2010) used a localization scheme in which the covariance matrix was tapered according to the stream trajectories around an observation well and also found an improvement in parameter estimation compared to the unlocalized EnKF. They also argue that their methodology is superior to distance-dependent localization schemes in highly heterogeneous media.

Chapter 3

Identification of time-variant river bed properties*

3.1 Introduction

Exchange fluxes between surface water and groundwater can have a profound influence on the chemical environment within the hyporheic zone, the riparian ecology and the local water balance around streams (Woessner, 2000; Sophocleous, 2002; Brunke and Gonser, 1997). For water management activities close to rivers, like bank filtration, the amount of exchanged water between river and aquifer influences the sustainability of groundwater use and also the quality of pumped groundwater. In order to predict the hydrological situation around rivers it is essential to obtain reliable estimates about the parameters that govern these exchange fluxes between river and groundwater namely the river bed conductivities.

Information on exchange coefficients can be inferred experimentally from different methods ranging from small scale measurements like permeameter tests, medium-scale information like temperature data as well as water balance methods for larger scales (Kalbus et al., 2006, and references therein). On the regional scale especially when management of groundwater is present the most common approach is to solve the groundwater flow equation with a numerical model and to calibrate river bed conductivities with observed head (and concentration) data. The calibrated river bed conductivities can then be used for predicting groundwater levels in the post-calibration period.

Different studies have shown that the fluxes between river and groundwater are strongly variable in space and time (e.g., Conant, 2004; Krause et al., 2007; Käser et al., 2009;

*adapted from: Kurtz, W., Hendricks Franssen, H.-J., and Vereecken, H. (2012). Identification of time-variant river bed properties with the ensemble Kalman filter. *Water Resour. Res.*, 48(10):W10534

Rosenberry and Pitlick, 2009b). The spatial variability of exchange fluxes is related to the heterogeneity of the river bed and the heterogeneity of the adjacent aquifer (e.g., Fleckenstein et al., 2006; Kalbus et al., 2009; Frei et al., 2009). Besides their spatial variability river bed characteristics may also change over time. Reasons for changing river bed properties may be flooding events that erode the river bed due to larger shear stress or an enhanced sedimentation during low flow conditions that leads to a colmation of the river bed (Schälchli, 1992).

In a flume experiment Rehg et al. (2005) investigated the effect of clay deposition on exchange fluxes between sediment and surface water. They observed the formation of a thin clogging layer that substantially decreased exchange fluxes when no movement of the bed sediment was present. However, when the bed sediment was slightly moved by the stream current and the particle size of the clay was small enough the formation of a clogging layer was not detected. Rosenberry and Pitlick (2009a) also used flume experiments to investigate the effect of sedimentation of fine particles on seepage fluxes between sediment and surface water. Their results showed that the vertical hydraulic conductivity of the sediment was decreased during downward flux and remained almost constant during upward flux.

Changes in river bed conductivity have also been observed at the field scale with different measurement and modeling techniques. Schubert (2002) investigated the relation between river dynamics and bank filtration activities at the river Rhine and found that the permeability of the clogging layer on top of the river bed varied temporally what was attributed to changes in sediment load of the river, erosion processes in the river bed and different hydraulic gradients between river and groundwater. Blaschke et al. (2003) measured leakage coefficients at an impounded river reach of the Danube and found a decrease of the determined river bed conductivities of about 2 log units within a time frame of 2 years which they attributed to clogging processes. They also found that flooding events led to temporary increases of river bed permeability at their site. Doppler et al. (2007) observed a significant change between model predictions and observations after a major flooding event which they attributed to the scouring of an impounded part of the investigated river. Hatch et al. (2010) used time series thermal methods to quantify the temporal evolution of river bed conductivities along a river reach. They observed changes in river bed conductivities of up to 1 log unit within a sedimentation period of 150 days and also increasing river bed conductivities due to high flow conditions. Zhang et al. (2011) used a 3D model of a managed site for river bank filtration to investigate the behavior of river bed permeabilities in relation to management activities. They calibrated river bed permeabilities at several times during a one year period and observed changes of up to a factor of 3 which they related to high and low flow conditions which were in part induced by management activities. Genereux et al.

(2008) repeatedly measured streambed hydraulic conductivities over a one year period with permeameter tests. At some of their measurement locations they observed nearly no change in river bed conductivities over time whereas for other observation points river bed conductivities followed different temporal patterns during the measurement campaign which they related to erosion and deposition processes of the sediment. They also observed an increase of river bed permeabilities after the reconstruction of a dam which they attributed to a possible scouring of the river bed. Mutiti and Levy (2010) used head and temperature measurements to calibrate river bed conductivities during flooding events. They observed that hydraulic conductivities had to be increased around the discharge peak compared to pre-flood conditions in order to accomplish a good fit between measured and simulated groundwater heads and temperatures. This was also related to river bed erosion associated with increased shear stress during the flooding event.

These observed changes in river bed properties can have a large impact on the prediction of groundwater or concentration levels near a river. For instance, when a groundwater model is calibrated for a certain time period with a specific, possibly spatially variable, river bed conductivity which is assumed to be constant for further time periods this model will not be able to respond to the changes in model parameters. This will result in systematically erroneous predictions of groundwater levels because the fluxes between river and groundwater are calculated with wrong parameter values for the river bed conductivities. In case of transport calculations, e.g., of contaminants, this wrong parameterization may be even more severe and may result in strongly biased predictions of the extent and breakthrough of contamination plumes.

Generally, one possible solution for calibrating time-dependent leakage parameters would be to recalibrate the model whenever deviations between measured and predicted groundwater levels exceed a predefined threshold value. However, these deviations between measurements and model predictions may also arise from measurement errors or predictions errors of the groundwater model (i.e., model structural errors or errors in the forcings terms). One could argue that the measurement errors are constant and known a priori, but the model errors are usually not. Prediction errors depend on many factors and could be temporally variable as well. For example, the uncertainty in timing and magnitude of a precipitation or flooding event could create deviations between measurements and model predictions which would then lead to a recalibration of model parameters although these parameters did not change in reality.

Another approach is to use sequential data assimilation methods like the Ensemble Kalman Filter (EnKF) (Evensen, 1994; Burgers et al., 1998) which has already been

used in various studies in groundwater hydrology (e.g., Chen and Zhang, 2006; Hendricks Franssen and Kinzelbach, 2008; Nowak, 2009; Sun et al., 2009; Huber et al., 2011) and is able to update model states as well as model parameters. EnKF offers a flexible framework to jointly handle different types of errors and uncertainty with respect to forcings and model errors is relatively straightforward to incorporate. Since it is a sequential method it might also be more suitable for assessing the transient behavior of river bed conductivities than other calibration methods. Furthermore, EnKF allows an automatization of the adaptation of model states and parameters which is an important issue for real-time modeling and management systems (e.g. Bauser et al., 2010). Results from Hendricks Franssen et al. (2011) indicate that EnKF is able to adapt to seasonal changes in river bed conductivities caused by the temperature dependency of viscosity (Doppler et al., 2007; Engeler et al., 2011) with a time lag of about 3 months what suggests the principal capability of data assimilation to capture changes in river bed conductivities. However, no systematic investigation of the behavior of EnKF towards time-variant river bed conductivities has been performed so far. Thus, the objectives of this study are to:

1. identify whether EnKF is able to capture temporal changes of river bed conductivities under different conditions
2. identify the most important factors that do affect the update of river bed conductivities with EnKF
3. find out under which conditions the characterization of temporally variable leakage coefficients will yield improved flow predictions in practice and will therefore be recommended

3.2 Methodology

In this chapter EnKF is used to determine time-varying river bed conductivities. EnKF is a Monte Carlo (MC) based method in which an ensemble of different model realizations (e.g., with varying model parameters or forcings) is propagated forward in time and updated whenever measurements of the model states (or parameters) become available. In contrast to other calibration techniques EnKF does not adjust parameter values of a model based on the residuals of the whole calibration period. Instead, it steps through time and only updates the model based on the measurements of one time step. EnKF is therefore an interesting method to calibrate time-dependent leakage values.

The basic elements of EnKF are the forecast step, the observation equation and the analysis step. The forecast step expresses how the states for the current time step are

estimated from the past time step, on the basis of the simulation model (which solves numerically the governing equation), initial conditions, boundary conditions, model forcings and model parameters:

$$\boldsymbol{\psi}_i^t = M(\boldsymbol{\psi}_i^{t-1}, \boldsymbol{\phi}_i, \boldsymbol{\zeta}_i) \tag{3.1}$$

where i is the stochastic realization ($i = 1...\mathrm{N_{real}}$), $\boldsymbol{\psi}_i^t$ is the model state vector for the current time step, $\boldsymbol{\psi}_i^{t-1}$ is the model state vector for the previous time step, $\boldsymbol{\phi}_i$ are model parameters, $\boldsymbol{\zeta}_i$ are model forcings and M is the forward model which in this case solves the 3D groundwater flow equation for variably saturated conditions including river-aquifer interactions (Equations 2.2 to 2.6b and Equation 2.11). $\boldsymbol{\psi}_i^t$ and $\boldsymbol{\psi}_i^{t-1}$ have a length that corresponds to the size of the problem, i.e., the number of nodes of the model $\mathrm{N_{nodes}}$.

Next the observation equation expresses how the simulation results at locations of observation points for the current time step are related to the whole state vector $\boldsymbol{\psi}_i^t$:

$$\hat{\boldsymbol{\psi}}_{\boldsymbol{i}}^{\boldsymbol{t}} = \mathbf{H}\boldsymbol{\psi}_{\boldsymbol{i}}^{\boldsymbol{t}} \tag{3.2}$$

where $\boldsymbol{\psi}_{\boldsymbol{i}}^{\boldsymbol{t}}$ is the simulated state vector for the current time step, $\hat{\boldsymbol{\psi}}_{\boldsymbol{i}}^{\boldsymbol{t}}$ is a vector for the simulated states at observation points with a length corresponding to the number of observations $\mathrm{N_{obs}}$ and $\mathbf{H}$ is a matrix that extracts or interpolates the simulated results at observation points from the simulated state vector with a dimension of $\mathrm{N_{obs}} \times \mathrm{N_{nodes}}$.

The measured states for the current time step $\boldsymbol{y}^0$ are perturbed with the perturbation vector $\tilde{\boldsymbol{\epsilon}}$ which is composed of values drawn from a normal distribution $\mathcal{N}(0, \epsilon)$ with a mean of zero and a standard deviation that corresponds to the measurement error ϵ of the assimilated state variable:

$$\tilde{\boldsymbol{y}}_i = \boldsymbol{y}^0 + \tilde{\boldsymbol{\epsilon}}_i \tag{3.3}$$

where $\boldsymbol{y}^0$ is the measurement vector for the current time step (with length $\mathrm{N_{obs}}$), $\tilde{\boldsymbol{\epsilon}}_i$ is a perturbation vector and $\tilde{\boldsymbol{y}}_i$ is the perturbed measurement vector for realization i.

Finally, the analysis step expresses how the forecasted states are corrected by the measurements. In the simplest configuration EnKF only updates the model states (in this case piezometric heads) for the whole domain. However, EnKF has been reformulated so that also model parameters can be updated with an augmented state vector approach (e.g., Chen and Zhang, 2006; Hendricks Franssen and Kinzelbach, 2008). The augmented

state vector approach implies that the vector with the quantities to be updated in the data assimilation procedure contains not only the model states, but also (part of) the parameters. In this study either piezometric heads $\boldsymbol{h}$ and river bed hydraulic conductivities (expressed as leakage coefficients $\boldsymbol{L}$) or piezometric heads, leakage coefficients and the hydraulic conductivity of the aquifer $\boldsymbol{K}$ are updated. Thus, the most general form of the state-parameter vector $\boldsymbol{\Psi}$ for this setup is given as:

$$\boldsymbol{\Psi} = \begin{pmatrix} \boldsymbol{h} \\ \log(\boldsymbol{K}) \\ \log(\boldsymbol{L}) \end{pmatrix} \tag{3.4}$$

where $\boldsymbol{h}$ is the vector of piezometric heads (i.e., the model state vector), $\log(\boldsymbol{K})$ and $\log(\boldsymbol{L})$ are the model parameters that should be updated and $\boldsymbol{\Psi}$ is the augmented state-parameter vector with a total length of $\mathrm{N_{nodes}} + \mathrm{N_{param}}$.

The analysis step itself is calculated with the following equation:

$$\boldsymbol{\Psi}_i^a = \boldsymbol{\Psi}_i^t + \alpha \mathbf{G}(\tilde{\boldsymbol{y}}_i^h - \mathbf{H}\boldsymbol{\Psi}_i^t) \tag{3.5}$$

where $\boldsymbol{\Psi}_i^t$ is the simulated state-parameter vector of the i^{th} ensemble member, $\boldsymbol{\Psi}_i^a$ is the updated state-parameter vector, $\tilde{\boldsymbol{y}}_i^h$ is the perturbed measurement vector of piezometric heads, $\mathbf{G}$ is the Kalman gain matrix and α is a damping factor that takes values between 0 and 1 and is only used for updates of model parameters. This damping factor is used to reduce filter inbreeding, i.e., the underestimation of ensemble variance in the assimilation process (see Hendricks Franssen and Kinzelbach, 2008). Note also that $\mathbf{H}$ has dimensions of $\mathrm{N_{obs}} \times (\mathrm{N_{nodes}} + \mathrm{N_{param}})$ for joint state-parameter updates.

The Kalman gain $\mathbf{G}$ in Equation 3.5 is the ratio between the simulated uncertainty and the sum of simulated and measurement uncertainty:

$$\mathbf{G} = \mathbf{C}\mathbf{H}^\top(\mathbf{H}\mathbf{C}\mathbf{H}^\top + \mathbf{R})^{-1} \tag{3.6}$$

$$\mathbf{C}\mathbf{H}^\top = \begin{pmatrix} \mathbf{C}_{\boldsymbol{h}\hat{\boldsymbol{h}}} \\ \mathbf{C}_{\log(\boldsymbol{K})\hat{\boldsymbol{h}}} \\ \mathbf{C}_{\log(\boldsymbol{L})\hat{\boldsymbol{h}}} \end{pmatrix} \tag{3.7}$$

where $\mathbf{C}$ is the covariance matrix of the simulated states and parameters and $\mathbf{R}$ is the covariance matrix of the state measurements. The covariance matrix $\mathbf{C}\mathbf{H}^\top$ (Equation

3.7) that is effectively used in calculation of the Kalman gain (Equation 3.6) is inferred from the states and parameters of the whole ensemble ($\boldsymbol{h}$, $\log(\boldsymbol{K})$ and $\log(\boldsymbol{L})$) and the simulated values of $\boldsymbol{h}$ at observation locations ($\hat{\boldsymbol{h}}$) and has a dimension of $(N_{nodes} + N_{param}) \times N_{obs}$. $\mathbf{R}$ is inferred from measurement errors at observation points and has a dimension of $N_{obs} \times N_{obs}$. For the numerical experiments performed in this study, covariances between the measurement errors at different observation points were set to zero. Therefore, only the variances at observation points were considered in $\mathbf{R}$.

3.3 Model description

The updating of time-variant L was tested in a synthetic experiment, but based on real-world data from the Limmat aquifer in Zurich (Switzerland). A schematic representation of the model domain is shown in Figure 3.1. The model domain covers an area of approximately 6×2 km. The rivers Sihl and Limmat are located at the eastern and northern boundaries of the model domain. In the Hardhof area (box in Figure 3.1) groundwater is extracted for drinking water supply. For that purpose, water is pumped from bank filtration wells located near river Limmat which is redistributed to the aquifer through several recharge wells and three recharge basins south of the river. Drinking water is then extracted through four drinking water wells which are located between the recharge basins and the river Limmat. The numerical solution of the groundwater flow equation was calculated with the software SPRING (Delta h Ingenieurgesellschaft mbH, 2006) which uses a finite-element scheme and is capable of simulating variably saturated flow and river-aquifer exchange fluxes. The model domain was discretized into 92015 nodes, 173599 elements and 25 layers. The average element size was ∼50 m but a higher spatial discretization was present in the Hardhof area where the average element size was ∼20 m and refined up to ∼1 m near wells. Vertical discretization was 1.6 m.

Forcing data for the simulations (river stages, recharge, pumping schedules, lateral inflows) were taken from real-world measurements. A detailed description of how these forcing data are calculated can be found in Hendricks Franssen et al. (2011). As a brief overview, recharge was calculated on the basis of data from the meteorological station in Zurich-Affoltern (MeteoSwiss). For this purpose, potential evapotranspiration (ET) was calculated according to the Penman-Monteith equation. Actual ET was then estimated on the basis of calculated potential ET with the help of a soil-water balance model by the FAO56 method (Allen et al., 1998). With the measured precipitation and calculated actual ET the potential recharge was calculated. Recharge was evenly distributed over the first layer of the model domain but only 15% of the calculated recharge was used because most of the model domain is urbanized sealed area. Small lateral inflows exist

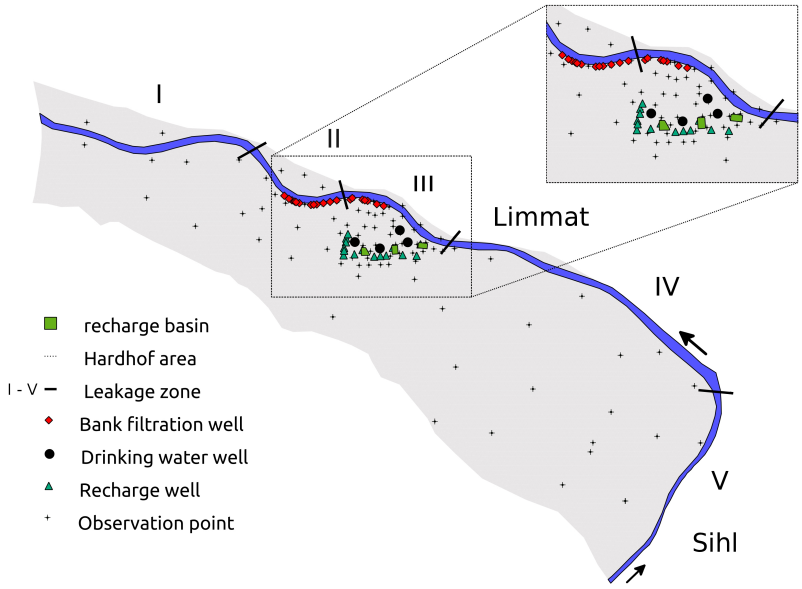

FIGURE 3.1: Schematic representation of model domain. River Sihl corresponds to leakage zone V and river Limmat corresponds to leakage zones I-IV.

on the south face of the model where water drains from the surrounding hill slopes of the Limmat valley. These lateral inflows were calculated on the basis of the estimated recharge rates. For the management activities in the Hardhof area (river bank filtration, artificial recharge) data for the extracted/ redistributed amounts of water were available from Water Works Zurich on a daily basis. River stages were calculated with the help of the hydraulic software FLORIS (Scietec Flussmanagement GmbH, 2000). Used input for these calculations were measured river stages at three locations, daily discharge values for the Limmat and Sihl and the expected geometry of the rivers Limmat and Sihl (interpolated from a large number of registered profiles along the river courses). Exchange fluxes between river and aquifer are incorporated in SPRING according to the leakage principle:

$$Q_{leak} = A_{leak} L (h^{river} - h^{gw}) \tag{3.8}$$

where Q_{leak} is the leakage flux between river and aquifer [L^3T^{-1}], A_{leak} is the area through which the leakage flux occurs [L^2], h^{river} is river stage [L], h^{gw} is groundwater level underneath the river [L] and L is leakage coefficient [T^{-1}] which is a lumped parameter for the hydraulic conductivity and the thickness of the river bed.

The river was implemented into the model with 457 leakage nodes which reside pairwise at the borders of the river. The river nodes were subdivided into five leakage zones with spatially constant L values within each of the zones. These five zones were originally defined for the region in order to capture the possible spatial variability of leakage coefficients. One of the five zones corresponds to the river Sihl whereas the river Limmat is divided in four zones in correspondence with the position of two weirs and management activities.

Basic model parameters were used from a prior calibration of the model. Porosity was set to a constant value of 0.15. Hydraulic conductivity K and leakage coefficients L were pre-calibrated with data from 87 piezometers for two calibration periods (June 2004 and July 2005) with the regularized pilot-point method (de Marsily, 1978; Alcolea et al., 2006). The two calibration periods were chosen because they include some main hydrologic features like one flooding event, intensive pumping activities as well as mean flow conditions.

3.4 Synthetic experiments

Multiple reference runs were simulated with the model described above. These reference runs always had a specific evolution of L values which should mimic certain events in the river bed (see Table 3.1). The starting values of L for the reference runs were always equal to the ones determined in the calibration procedure and simulations were always performed for the period from January 2004 to August 2005 (609 days). From these reference runs daily piezometric head data from 100 observation points were collected which were then used as conditioning data for the data assimilation with EnKF. The distribution of these observation points is shown in Figure 3.1. Observation points are mainly concentrated in the Hardhof area where most of the model dynamics takes place which is related to the pumping and artificial recharge activities in this area. For most of the ensemble runs with EnKF only L was assumed to be uncertain. For these scenarios K values and forcing data were equal to the ones in the reference run. Ensembles of L were generated by perturbing the $\log(L)$-values from the calibration (i.e., the starting values of the reference run) with samples from a normal distribution with mean value of 0 and a standard deviation of 1 $\log(s^{-1})$. A total of 100 ensemble members was generated for the simulations with EnKF. The basic updating scheme for EnKF was to jointly update h and L with data from the 100 observation points every 10 days with a damping factor α of 0.1 and a uniform measurement error of 0.05 m at the observation points.

TABLE 3.1: Employed reference scenarios for the temporal evolution of leakage coefficients (L)

scenario	description	temporal evolution of L
A	flooding event	L constant until day 155; raise of L by one log unit at day 155; L remains constant until day 609
B	sedimentation event	L constant until day 200; linear decrease of $\log(L)$ by one unit until day 400; L remains constant until day 609
C	combined flooding and sedimentation event	L constant until day 155; raise of L by one log unit at day 155; L remains constant until day 200; linear decrease of $\log(L)$ (one log unit) until day 600; L remains constant until day 609
D	temperature dependency of L	L is corrected for daily changes in water viscosity with measured temperatures of the river Limmat

In the second part of this study the setup of the experiments was varied in order to investigate the influence of different factors on the update of L with EnKF. This sensitivity study includes the effect of uncertain hydraulic conductivities, effects of spatially varying L values, the influence of a bias in the initial L ensemble and different updating strategies for EnKF. These different simulations always employed the reference scenario A from Table 3.1. Additionally, simulations with an adaptive filtering approach were performed. This approach has already been used in the atmospheric data assimilation community and could be beneficial for reducing the possible problem of filter inbreeding in the simulations.

The updated ensembles of h and L for the different reference scenarios were mainly evaluated with respect to the temporal evolution of the zonal L ensembles and the temporal evolution of piezometric head errors at the observation points. For the evaluation of errors the Root Mean Square Error (RMSE) of h and L was calculated:

$$\mathrm{RMSE_h} = \sqrt{\frac{1}{\mathrm{N_{obs}N_{real}}} \sum_{i=1}^{\mathrm{N_{obs}}} \sum_{j=1}^{\mathrm{N_{real}}} (h_{ij} - h_i^{ref})^2} \tag{3.9}$$

$$\mathrm{RMSE_L} = \sqrt{\frac{1}{\mathrm{N_{leak}N_{real}}} \sum_{i=1}^{\mathrm{N_{leak}}} \sum_{j=1}^{\mathrm{N_{real}}} (\log(L)_{ij} - \log(L)_i^{ref})^2} \tag{3.10}$$

where $\mathrm{N_{obs}}$ is equal to the number of observation points, $\mathrm{N_{real}}$ is the number of realizations and $\mathrm{N_{leak}}$ is the number of leakage zones.

It has to be noted that the evolution of leakage coefficients was not directly evaluated with the parameter L given in Equation 3.8 but with the slightly modified parameter L^* which is the parameter L multiplied with half of the river width. This was done because

the simulation code internally calculates with L^* but that does not directly influence the outcome of the simulations because the river width in the whole model domain is rather constant (about 50 m) and the emphasis was to compare the response of EnKF to relative changes towards a reference state (i.e., the initial L^* values of the reference runs). Thus, the two parameters L and L^* are used interchangeable in the following sections. As there is no explicit information about the thickness of river sediment in the model domain, river bed characteristics are always treated as effective parameters in the model evaluation, i.e., it is not distinguished whether changes in river bed properties are related to changes in bed thickness or changes in river bed conductivities.

3.5 Results

3.5.1 Increase of L (scouring event)

In order to mimic a scouring of the river bed after a flooding event, L was increased by one log unit for all zones of the reference run after a major flooding event on day 155 (scenario A). The evolution of L values of the reference run for this scenario is shown together with the updated L values in Figure 3.2. For the update head observations were assimilated from the 100 observation points every 10 days and heads and L values were jointly updated at the observation times. It can be seen that the ensemble means remain fairly constant at the beginning of the simulation. These nearly constant values at the beginning would be the expected behavior of EnKF because the initial ensemble mean for each leakage zone is equal to the leakage values of the reference run. After the jump of L in the reference run at day 155 the ensemble mean of updated L values starts to increase for all five leakage zones. This increase is strongest shortly after the flooding event and then slows down markedly within 150 days following the step change, after which L is nearly constant. The final ensemble means of L at the end of the simulation period (609 days) do not exactly match the post-flooding reference values but all L values increase >0.6 log units after the flooding event.

The variability of the ensemble continuously decreases during the course of the simulation (see shaded area in Figure 3.2). For the period before day 155 where the reference values for L are constant this should be the expected behavior of EnKF because the filter trusts the ensemble mean which is close to the true value. However, after the jump in L this process still continues and the variance in the ensemble of L almost vanished for three of the five zones by the end of the simulation period.

In Figure 3.3 the temporal evolution of RMSE of forecasted piezometric heads at observation points ($\mathrm{RMSE_h}$) for this scenario is compared with the one of an unconditional

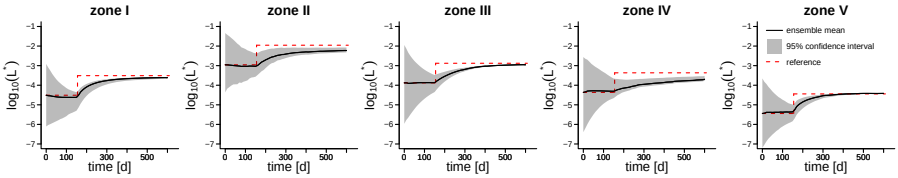

FIGURE 3.2: Temporal evolution of zonal leakage coefficients (period January 2004 - August 2005) for reference run and update with the Ensemble Kalman Filter for simulation scenario A (Table 3.1).

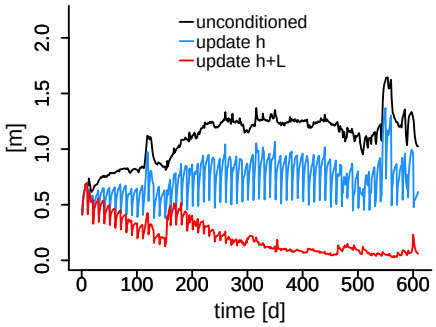

FIGURE 3.3: Temporal evolution (period January 2004 - August 2005) of root mean square error of piezometric heads ($RMSE_h$) at observation points for an unconditional simulation ('unconditioned', no update of piezometric heads and leakage coefficients), an update of piezometric heads every 10 days ('update h') and for a joint update of piezometric heads and leakage coefficients every 10 days ('update h+L').

ensemble simulation (i.e., neither h nor L are updated) and with a simulation run where only h was updated every 10 days. For the unconditional run the error rises by a factor of about 2 during the simulation period compared to the initial error whereas $RMSE_h$ for the simulation where h and L are updated simultaneously reaches a value of about 5 cm by the end of the simulation. The error for the solely update of h remains approximately at the same magnitude as the initial error but shows rather high fluctuations between the times when the ensemble is updated. These fluctuations are related to the higher spread of the ensemble of L compared to the simulation where also L was updated. After the flooding event these fluctuations increase in magnitude caused by the fact that also systematic errors are introduced due to the increase of L in the reference run which cannot be captured when only h is updated. This also leads to relatively high errors around day 550 where pumping rates were temporally increased. In contrast, errors for a joint update of h and L did not increase for this event which is related to the adaptation of L and its decreased ensemble variance.

Figure 3.4 gives an overview over the fluxes between river and aquifer. The diagram for the unconditional simulation shows that the variability of positive and negative

fluxes is very high for the utilized initial ensemble of L. For unconditional simulations the mean fluxes for both directions (gaining and losing conditions of the river) are rather constant throughout the simulation period with the exception of two periods of increased pumping activities around day 120 and day 550. The fluxes for the reference run are markedly increased after the change in L at day 155. When only h is updated especially the ensemble mean for fluxes from river to aquifer are slightly corrected after each assimilation cycle but it is not possible for EnKF to adjust the fluxes solely by correcting h. For a joint update of h and L the ensemble mean of both flux directions is consecutively adjusted to the reference values which are approximated very closely after day 450.

Figure 3.5 additionally shows the spatial distribution of averaged exchange fluxes for different time steps along the x-axis of the model domain (in the Swiss coordinate system). For time step 100 the distribution of fluxes is very similar for all different updating scenarios and also closely corresponds to the one in the reference run. Shortly after the change of river bed properties (time step 200) the spatial distributions for the different scenarios all deviate from the reference run. An update of states and parameters corrects this deviation as the assimilation proceeds (see time step 500). However, an update of states alone does not correct for the biased exchange fluxes.

3.5.2 Decrease of L (sedimentation event)

In a next step a sedimentation event was emulated in order to verify whether EnKF also adapts to slowly decreasing L values. A reference run was generated where L was decreased by one log unit over a period of 200 days (starting from day 200 until day 400) for all five leakage zones (scenario B). The updating strategy was the same as for the scouring test case (scenario A). The evolution of L in the reference run together with the updated L values are shown in Figure 3.6. Again the ensemble means for the different zones remain fairly constant before the change in L. When L starts to decrease after day 200 zonal ensemble means of L also decrease during the EnKF update with the exception of the most western zone in the model domain (zone I). In this part of the aquifer the groundwater levels are rather close to the river bottom and the initial L values are low. As a consequence, the leakage fluxes between river and aquifer are generally low. The modification of L that was simulated in the reference run has a limited impact on the piezometric heads close to the river and therefore piezometric head measurements will not be so effective (compared to other zones) for adapting the value of L. For this experiment, L generally does not adapt so well to the reference L values because the adaptation at the end of the simulation period is worse for three of the five zones (as compared with the scouring experiment). However, when the simulation

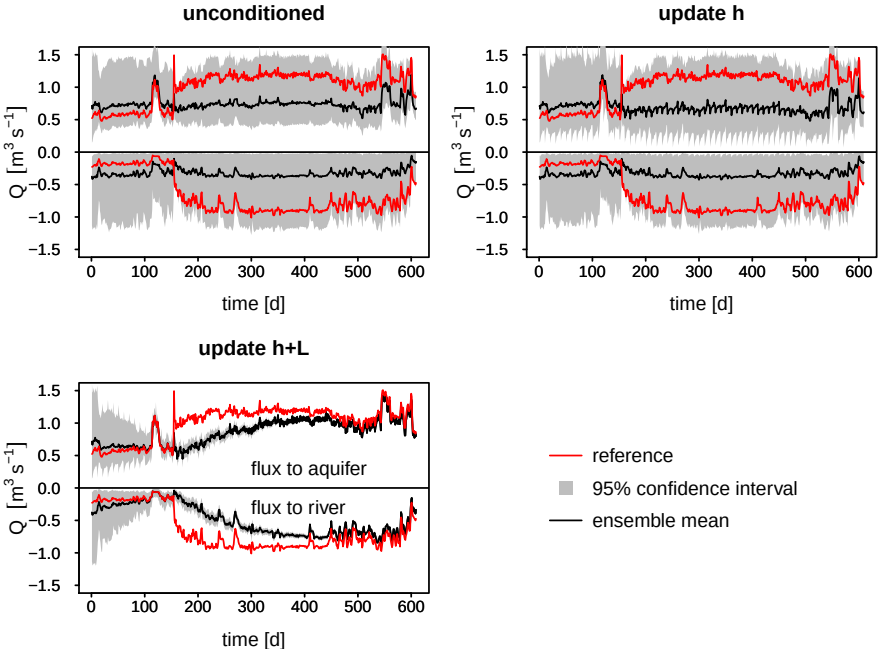

FIGURE 3.4: Temporal evolution (period January 2004 - August 2005) of fluxes between river and aquifer for an unconditional simulation ('unconditioned', no update of piezometric heads and leakage coefficients), an update of piezometric heads every 10 days ('update h') and for a joint update of piezometric heads and leakage coefficients every 10 days ('update h+L'). Fluxes in the upper (positive) part of each diagram are from river to aquifer and fluxes in the lower part (negative) are from aquifer to river.

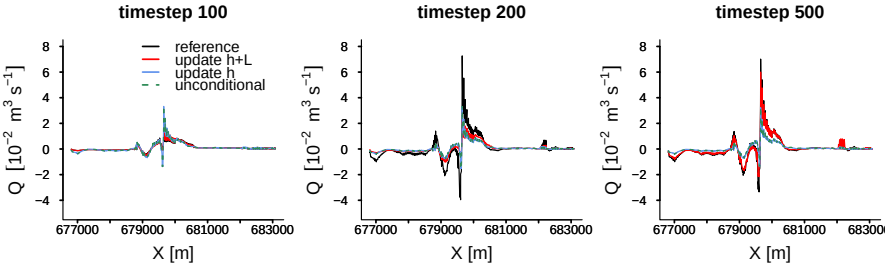

FIGURE 3.5: Spatial distribution of river-aquifer exchange fluxes for an unconditional simulation ('unconditional', no update of piezometric heads and leakage coefficients), an update of piezometric heads every 10 days ('update h') and for a joint update of piezometric heads and leakage coefficients every 10 days ('update h+L').

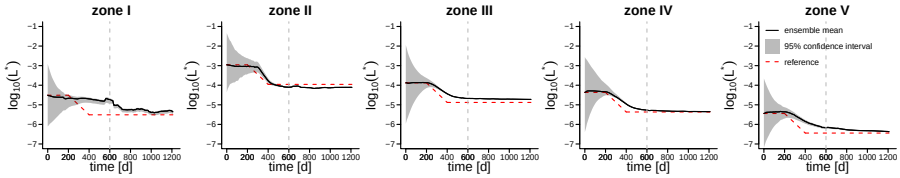

FIGURE 3.6: Temporal evolution of zonal leakage coefficients (period January 2004 - April 2007) for reference run and update with the Ensemble Kalman Filter for simulation scenario B (Table 3.1).

time is expanded to 1200 days a similar adaptation as in scenario A was observed for all of the five zones. The variances of the L ensembles for the different zones behave similar to the flooding scenario, i.e., show a continuous decrease throughout the simulation period. For four of the zones variability within the ensemble has almost vanished at the end of the simulation period.

3.5.3 Performance of EnKF for combined flooding and sedimentation events

The two simulations described above have shown that EnKF is principally capable of adapting towards increases and decreases of L. However, natural sediment dynamics often exhibit a sequence of sedimentation and scouring events (e.g. Blaschke et al., 2003). Therefore, such a scenario was artificially constructed by appending a sedimentation period to scenario A. In this scenario L values for all leakage zones were raised by one log unit at day 155. L is then held constant for 45 days and then again decreased by one log unit from day 200 until day 600 in order to simulate a long lasting sedimentation event (scenario C). The evolution of the updated L ensembles together with the corresponding reference values is depicted in Figure 3.7. From all five leakage zones it becomes obvious that EnKF corrects for both changes of L within the simulation period. After the flooding event the ensemble means of L start to increase. Approximately at day 300 this increase reaches an apex and the ensemble means of L begin to adapt to the decreasing values of the reference run. The zonal ensemble means of L rise between 0.2 and 0.5 log units in the phase after the flooding event. For all five leakage zones the reference value is approximately intersected at these maximal values of the ensemble mean of L. After that peak the ensemble means decrease but only for one zone (which corresponds to the lowest prior increase in L) the reference value is reached within the simulation period. For the other four leakage zones the ensemble means adapt rather slowly towards the reference line. This again shows that the adaptation with EnKF towards changes in L has a rather long response time which does not optimally capture rapid changes in river bed properties.

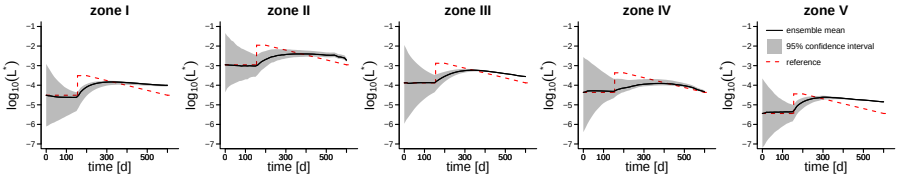

FIGURE 3.7: Temporal evolution of zonal leakage coefficients (period January 2004 - August 2005) for reference run and update with the Ensemble Kalman Filter for simulation scenario C (Table 3.1).

3.5.4 Temperature dependency of L

Apart from mechanically induced changes of the river bed like scouring and sedimentation the hydraulic conductivity of the river bed can also be influenced on a seasonal scale by temperature variations of the river due to the temperature dependency of viscosity as can be seen from Equations 3.11 and 3.12 (Muskat, 1937):

$$K(T) = \frac{k\rho_w g}{\mu(T)} \tag{3.11}$$

$$\mu(T) = 2.414 \cdot 10^{-5} 10^{\frac{247.8}{T-140}} \tag{3.12}$$

where $K(T)$ is temperature dependent hydraulic conductivity [LT^{-1}], k is intrinsic permeability of the porous medium [L^2], ρ_w is density of water [ML^{-3}], g is gravitational acceleration [LT^{-2}], $\mu(T)$ is temperature dependent dynamic viscosity of water [$\mathrm{ML}^{-1}\mathrm{T}^{-1}$] and T is temperature [θ].

Within the simulation period the measured temperatures of the river Limmat varied from 4 °C to 26 °C which translates into a variation of viscosity of up to a factor of 1.7 whereas the change of water density in this temperature range is less than 1%. It has been shown by Engeler et al. (2011) that this temperature dependency of L can have a profound influence on the predicted groundwater dynamics close to rivers. In the simulation model L values are not corrected for temperature variations of the river but usually these variations occur in natural settings. Therefore, a reference run was created in which these natural variations of L occur and it was tested whether EnKF is able to follow these changes. For this purpose, the L values of all leakage nodes of the reference run were corrected with the measured temperature of the river Limmat on a daily basis so that all leakage nodes follow the same variation pattern (scenario D). The temporal evolution of zonal L values of the reference run is shown in Figure 3.8 together with the updated ensemble values. The L values of the reference run follow a seasonal

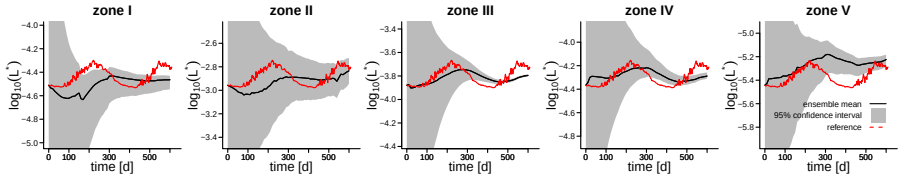

FIGURE 3.8: Temporal evolution of zonal leakage coefficients (period January 2004 - August 2005) for reference run and update with the Ensemble Kalman Filter for simulation scenario D (Table 3.1).

cycle with higher values during the summer months and lower values during winter. The maximal change of L values for the reference run within the simulation period was 0.23 log units and thus is lower than for the previous scenarios. For zones I and II the update of L with EnKF shows some temporal changes but they do not correspond very well with the temporal dynamics of the reference run. For the zones III to V the temporal evolution of updated L values is more close to the reference run especially for zone III. Again a certain time lag is observed between the reference and the updated L values which seems to be a bit higher for zones IV and V than for zone III. The rather high sensitivity of zone III towards the temperature-dependent changes of L may be related to the fact that the highest exchange fluxes between river and aquifer occur in this part of the model domain. As a result, the ensemble of L values for this zone responds well to the low changes of L that are induced by the temperature dependency. For leakage zones I and II the groundwater table is very close to the river bottom and thus the fluxes between river and aquifer are rather low what might be a cause for the rather low sensitivity of these two zones. For leakage zones IV and V the groundwater table is significantly lower than the river bottom but also the L values are low for these two zones what results in lower exchange fluxes compared to leakage zone III and may be a cause for the lower sensitivity towards the relatively small changes in L that are induced by river temperature fluctuations.

3.5.5 Influence of spatial patterns

For the previous simulations the change in L was always realized in a spatial homogeneous fashion, i.e., L was changed for all five zones with the same magnitude. In natural systems changes in L due to sedimentation or scouring are expected to happen in a more spatially inhomogeneous fashion. This may happen for example due to meandering of the river which provides spatial sequences of sedimentation and scouring zones which may proceed downstream over time. Also storm events may cause scouring of the river bed preferentially at certain zones where flow velocities and thus shear stress is higher. Therefore, it was also investigated how EnKF reacts towards changes in L that occur

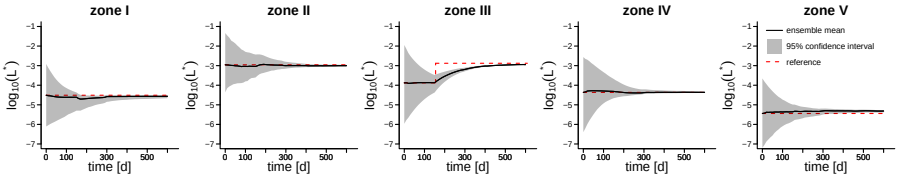

FIGURE 3.9: Temporal evolution of zonal leakage coefficients (period January 2004 - August 2005) for reference run and update with the Ensemble Kalman Filter when the zonal leakage coefficient of zone III in the reference run is increased by one log unit at day 155.

only at a part of the river reach. For this setup the value of L was only increased for leakage zone III while for the other zones L remained constant throughout the simulation period. Results for this setup are shown in Figure 3.9. The ensemble means for the four zones which are not subjected to any changes in L remain almost constant throughout the simulation period. For zone III EnKF adapts the ensemble mean closely to the reference value by the end of the simulation and the course of the adaptation curve is similar to the ones observed when the L values for all zones are increased (see Figure 3.2). This means that EnKF captures the spatially separated evolution of L for the different zones which is possibly due to the fact that correlations between the piezometric heads at the observation points and the L ensemble at the four other leakage zones are rather weak. Beforehand it was expected that at least the two neighboring leakage zones would also be affected by the update with EnKF because the filter might give some weight to them in the updating procedure. However, this was not the case in this scenario. One possible reason could be that the leakage zone is close to the managed site (Hardhof area) where the groundwater pumping and artificial recharge takes place. Therefore, the groundwater levels at the observation points in this area which comprise the major part of all observation points are especially affected by changes of the increasing leakage zone.

3.5.6 Influence of uncertain hydraulic conductivities

In previous simulations L was the only uncertain parameter and hydraulic conductivities of the aquifer were assumed to be known exactly. This assumption was introduced in order to isolate the effect of uncertain L values in the update with EnKF. This simplification is rarely justified for real world examples because the uncertainty regarding K very often governs the uncertainty of model output. Furthermore, it was shown (e.g. Kalbus et al., 2009) that heterogeneity of the underlying aquifer plays a major role for exchange fluxes between river and aquifer and thus should ideally not be neglected for

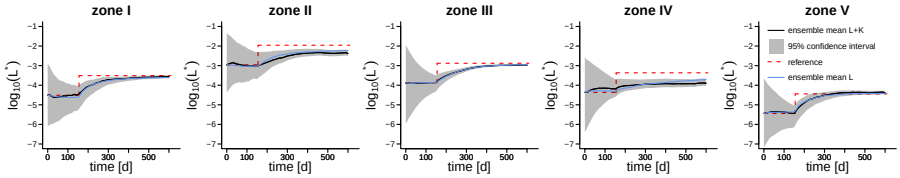

FIGURE 3.10: Temporal evolution of zonal leakage coefficients (period January 2004 - August 2005) for reference run and an update of either leakage coefficients alone ('ensemble mean L') or a joint update of leakage coefficients and hydraulic conductivities of the aquifer ('ensemble mean L+K') for simulation scenario A (Table 3.1).

the simulations. For these reasons simulations were performed in which also the ensemble members of K are different among each other. The ensemble of K was generated by Sequential Gaussian Simulation (SGS) (Gómez-Hernández and Journel, 1993) on a very fine grid which was then upscaled to the simulation grid through simplified renormalization (Renard et al., 2000). For details of the ensemble generation see Hendricks Franssen et al. (2011). For these realizations the variance in $\ln(K)$ was 2.7.

The setup of this experiment was similar to scenario A with the only difference that the ensemble of K showed the described uncertainty and values of K and L were jointly updated together with piezometric heads via EnKF. When comparing the temporal evolution of zonal ensemble means of L (Figure 3.10) only small differences are observable between the runs with and without uncertain K values. The RMSE of piezometric heads at observation points during the first 100 days was higher for the ensemble with uncertain K values compared to the one with deterministic K values which is due to the additional uncertainty for this parameter. In later steps RMSE for both simulations is very similar which is mainly caused by the adaptation of K values with EnKF which decreases the variance of K in the assimilation process. A comparison of the initial and updated mean fields of $\log(K)$ is given in Figure 3.11. It can be seen that the initial mean field of $\log(K)$ is relatively smooth. During assimilation the spatial structure of $\log(K)$ generally gets more patchy because every finite element of the model is allowed to update separately. However, the major distribution of $\log(K)$ values (increasing values from east to west) is preserved.

3.5.7 Influence of ensemble bias

Besides the uncertainty regarding hydraulic conductivities mentioned in the previous section the updating of L with EnKF may also be affected by a bias of the initial ensemble of L. In the previous simulations the zonal mean values of the initial ensemble of L were equal to the true values of the reference run. However, in real-world situations information on river bed conductivities within the model domain often is scarce and

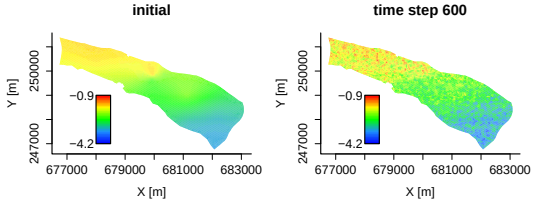

FIGURE 3.11: Ensemble mean of $\log(K)$ for initial ensemble (left) and at time step 600 (right) for model layer 4 when hydraulic conductivities and leakage coefficients are jointly updated every 10 days.

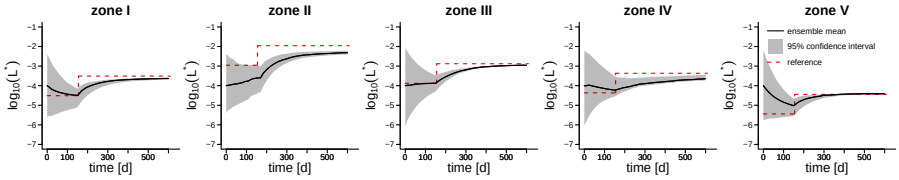

FIGURE 3.12: Temporal evolution of zonal leakage coefficients (period January 2004 - August 2005) for reference run and update with the Ensemble Kalman Filter for scenario A when the initial ensemble mean of leakage coefficients was biased compared to the initial values of the reference run.

the generation of the initial ensemble of L may thus only rely on a few or even no measurement data. Therefore, an initial ensemble of L was created where the ensemble means of all five leakage zones were the same and corresponded to the arithmetic mean of $\log(L)$ values of the reference run (averaged over all five leakage zones). The ensemble variances of the different zones were similar to the ones in the previous simulations. Results for this biased initial ensemble are shown in Figure 3.12. Because all zonal ensemble means of L started with the same value the bias between the initial ensemble mean and the reference value is different among the five leakage zones. During the period before the increase of L in the reference run (up to day 155) the ensemble means of all zones more or less tend to move towards their corresponding reference value. After the jump of L values in the reference run ensemble means of all zones start to increase no matter whether their tendency was to increase or decrease before the flooding event. The evolution of zonal L values looks rather similar to the ones shown before, i.e., a steeper increase at the beginning which flattens after about 100 days. Also the variance of the ensembles behaves similar to the previous examples. Due to the initial bias the absolute performance of EnKF is not as good as for a case where the initial zonal ensemble means are closer to the true values. However, a distinct reaction of EnKF towards the true values is clearly visible.

TABLE 3.2: Different updating scenarios for zonal leakage coefficients.

scenario	update frequency [d]	N_{real}	N_{obs}	α
base	10	100	100	0.1
fupd	1, 2, 5, 10	100	100	0.1
ens	10	100, 200	100	0.1
nobs	10	100	5, 10, 20, 50, 100, 200	0.1
damp	10	100	100	0.1, 0.2, 0.5, 1.0

3.5.8 Sensitivity on updating strategy

The performance of EnKF in part depends on the amount of available observation data and on filter specific settings like the number of ensemble members, the updating interval or the damping factor α. Compared to the base scenarios (100 ensemble members, update frequency of h and L: 10 days, α=0.1, 100 head observations) each of these meta parameters was changed in order to see whether they significantly affect the performance of EnKF for the given setup. The different parameters for each of these scenarios are summarized in Table 3.2 where scenario 'base' serves as a reference for all other scenarios.

An increase of the ensemble size to 200 ensemble members (scenario 'ens_200') did not significantly improve L compared to the 'base' scenario as the performance for one of the leakage zones slightly decreases.

The effect of updating frequency on the evolution of L (scenario 'fupd') can be seen in Figure 3.13 for four different updating frequencies (1, 2, 5 and 10 days). In general, an increase of the updating frequency for h and L did not lead to an improvement of L updates. For an updating frequency of 5 days the adaptation of L was slightly faster for zone III but the performance for the other zones was equal or slightly worse compared to the 'base' scenario. An updating frequency of 1 or 2 days did not increase performance in any of the five leakage zones. Especially for zones II and IV the performance degrades when h and L are updated very frequently. A reason for this behavior may again lie in the fast decrease of ensemble variance in the updating procedure. In Figure 3.13 also the ensemble standard deviation is compared for the different updating frequencies. With decreasing updating intervals the ensemble variance also decreases very rapidly for all leakage zones. For updating frequencies of 1 or 2 days the ensemble variance is almost zero before the change in L at day 155 whereas for lower updating frequencies more variability is maintained in the ensemble.

For a sensitivity analysis on the number of observations points (scenario 'nobs') six different configurations were compared where the number of observation points ranged from 5 to 200. The observation points for the scenarios 'nobs_5' to 'nobs_50' always

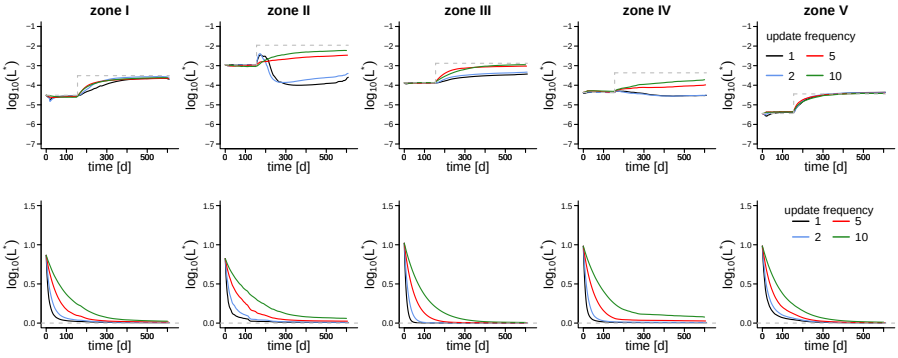

FIGURE 3.13: Temporal evolution (period January 2004 - August 2005) of ensemble mean (upper row) and ensemble standard deviation (lower row) of zonal leakage coefficients for different updating frequencies of piezometric heads and leakage coefficients (simulation scenario A).

were a subset of the scenario 'nobs_100' which is the configuration used in the previous simulations (equal to 'base'). For these scenarios the observation points were coincident, e.g., the observation points for scenario 'nobs_5' were contained in all other scenarios. One exception is the comparability between scenario 'nobs_20' and 'nobs_50' where both scenarios only shared 10 observation points. For the scenario 'nobs_200' 100 additional observation points were added to 'nobs_100' and these were spread over the whole model domain. In Figure 3.14 the temporal evolution of $\mathrm{RMSE_L}$ is compared for the different number of observation points. It is clearly visible that the errors in L are inversely correlated to the number of observation points. For the pre-event period the differences among the scenarios are mostly related to the different decrease in ensemble variance which means that the ensemble variance in case of few observation points does not decrease as fast as for a larger amount of observation points. In the post-event period also the different updating behavior towards L contributes to the differences among the scenarios. At the end of the simulation period the errors in L follow an exponential decrease with the number of observation points. However, it can be observed that even as little as 10 observation points result in a reduction of $\mathrm{RMSE_L}$ of 70% as compared to the open loop simulations. Nevertheless, $\mathrm{RMSE_L}$ is roughly twice as large at the end of the simulation period for 10 observation points compared to 100 observation points. A closer look at the temporal evolution of the zonal ensemble means of L for the different scenarios (data not shown) reveals that the updating capability of EnKF for the two zones close to the Hardhof area (zones II and III) and for the Sihl (zone V) is rather similar among the scenarios whereas for the two other zones the updating capability is more strongly dependent on the number of observation points. This might be an indicator that the observation points which were used for the simulations with a lower number of observation points generally had a lower sensitivity towards these two leakage

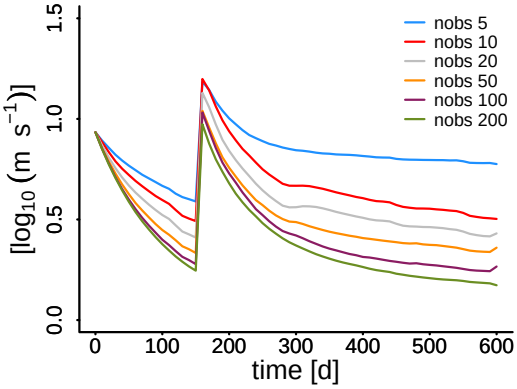

FIGURE 3.14: Temporal evolution (period January 2004 - August 2005) of root mean square error of leakage coefficients for different numbers of observation points (simulation scenario A).

zones. This also means that in order to be able to adapt the L values for all leakage zones a sufficient number and spatial distribution of observation points is needed.

Furthermore, it was tested whether the damping factor α could be raised for the update of L (scenario 'damp') what could possibly lead to a faster adaptation of zonal ensemble means towards reference values. This option was tested for four values of α (0.1, 0.2, 0.5 and 1.0). Results for the different values of the damping factor (data not shown) revealed that higher values than 0.1 (the 'base' updating scenario) generally lead to a worse performance of EnKF in updating the zonal ensemble means towards the reference values which is possibly related to the more rapid decrease in ensemble variance for higher α values which is in accordance with the findings of Hendricks Franssen and Kinzelbach (2008).

3.5.9 Use of covariance inflation to improve filtering results of EnKF

In all different scenarios it became obvious that the response time of EnKF to adapt for changing L values is rather long which is to some part related to the fast decrease in ensemble variance. In order to compensate for this loss of variance which is related to filter inbreeding, covariance inflation was applied. This method could possibly improve the response time of EnKF and is a common approach in atmospheric data assimilation (e.g., Hamill et al., 2001; Anderson, 2007, 2009). For covariance inflation an inflation factor λ is used to spread the ensemble around its mean value before every assimilation step.

$$\mathbf{\Psi}_{ij} = \lambda(\mathbf{\Psi}_{ij} - \overline{\mathbf{\Psi}}_i) + \overline{\mathbf{\Psi}}_i \tag{3.13}$$

Before each assimilation cycle every element i of the state-parameter vector $\mathbf{\Psi}_{ij}$ for the j^{th} realization is inflated around the ensemble mean $\overline{\mathbf{\Psi}}_i$ with the inflation factor λ. This means that the ensemble mean $\overline{\mathbf{\Psi}}_i$ for every element is preserved and only the spread of the ensemble is slightly increased. In atmospheric sciences it was especially in the past common to set the inflation factor λ to a constant value (e.g., Hamill et al., 2001). Recently, it has also been proposed to make λ temporally and spatially variable (e.g., Anderson, 2007, 2009). We used the inflation method proposed in Anderson (2007) in which λ is temporally variable. In this method a Bayesian update is performed on λ every assimilation cycle and the new value of λ is mainly a function of ensemble variance, measurement errors, deviations between observations and simulations and the variance of λ itself (which is kept constant in this case). This approach allows to correct for deficiencies in the assimilation process (i.e., filter divergence) by inflating the ensemble based on the residuals at observation points and the ensemble variance. An outline of the used algorithm is given in Appendix A. For a more detailed insight into the methodology it is referred to Anderson (2007).

Figure 3.15 compares the evolution of L for scenario A without and with adaptive covariance inflation. For the simulations with adaptive inflation L values for all zones reach the reference values more closely than for simulations without inflation. Furthermore, the adaptation time to reach a certain L value is slightly decreased when covariance inflation is used. The evolution of ensemble variance for covariance inflation also shows the expected behavior. Before the flooding event the decrease in variance is comparable to the simulations without inflation. When L is increased in the reference run λ values increase due to the higher residuals at the observation points which also leads to an increasing ensemble variance which allows to update L more closely (and faster) to the reference values.

It was already mentioned that an increase of α in the simulations without inflation leads to a worse performance of EnKF. This effect can be seen in the upper row of Figure 3.16 where α was set to a value of 0.2. In this case the adaptation time for zones III and V is decreased but the absolute adaptation for zones II and IV were worse compared to α=0.1. However, when covariance inflation is used for this example L is adapted faster and more accurate compared to the base scenario (i.e., no inflation, α=0.1).

Additionally, the simulations for the other three base scenarios (scenario B, C and D) were repeated with covariance inflation for α=0.2 (see Figure 3.17). For scenarios B and C the adaptation time generally decreases and also the accuracy at the end of the

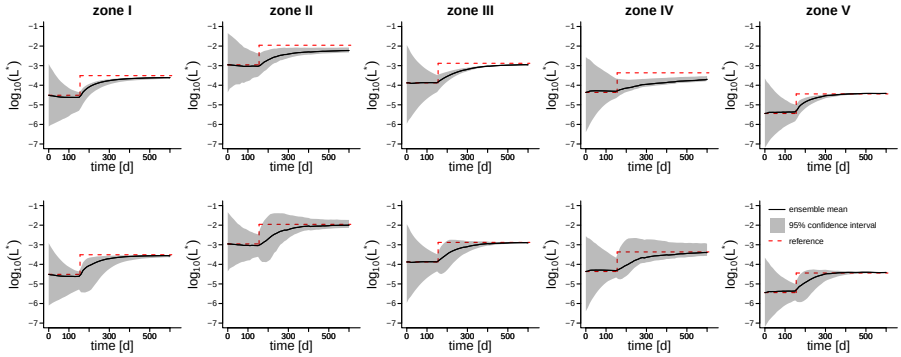

FIGURE 3.15: Comparison of temporal evolution of zonal leakage coefficients without (upper row) and with (lower row) adaptive covariance inflation for scenario A (damping factor $\alpha = 0.1$).

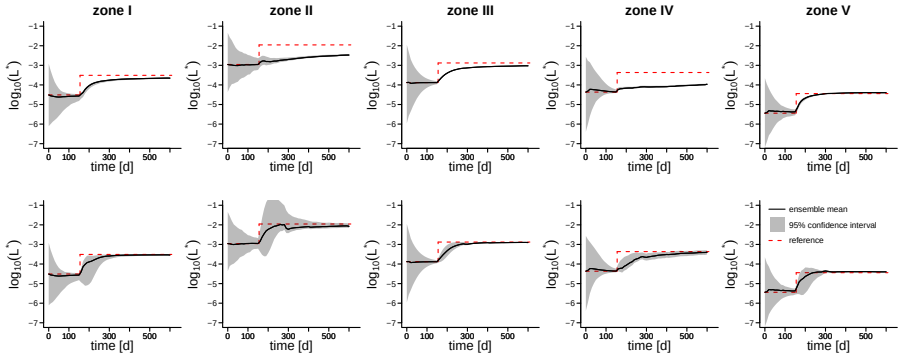

FIGURE 3.16: Comparison of temporal evolution of zonal leakage coefficients without (upper row) and with (lower row) adaptive covariance inflation for scenario A (damping factor $\alpha = 0.2$).

assimilation period is improved although for one zone (zone I in scenario B) some slight instability occurs which again is possibly related to the low sensitivity of this zone for that scenario which was also obvious from the corresponding base scenario. For the variability of L due to temperature changes (scenario D) a positive effect of covariance inflation was not significant which is most likely related to the small changes of L in this scenario.

It has already been mentioned that an increase of updating frequency did not improve the adaptation of L for the base scenario. However, when covariance inflation is used (see Figure 3.18) the adaptation time can generally be decreased with a higher updating frequency. This can be observed for all of the five leakage zones where updating frequencies of 2 or 5 days consistently performed better than an updating frequency of 10 days. The ensemble standard deviation (lower row in Figure 3.18) increases after the

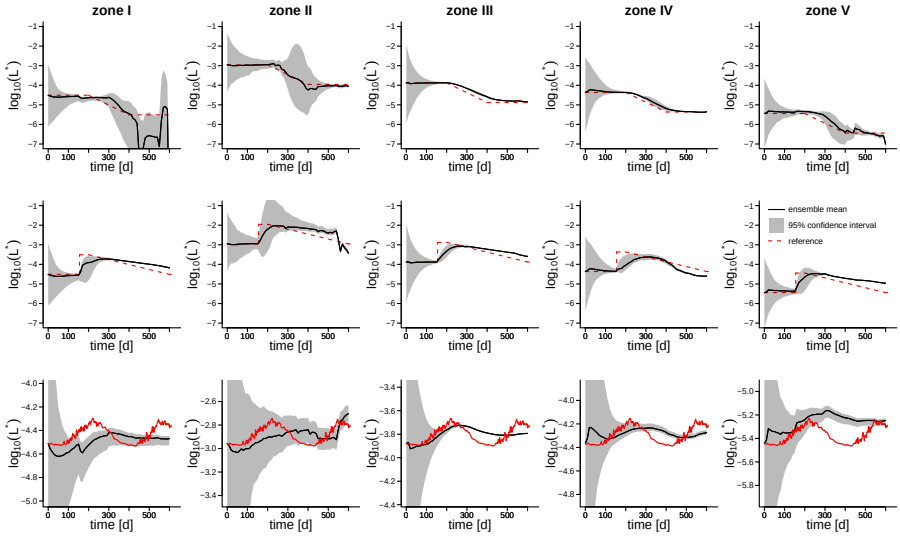

FIGURE 3.17: Temporal evolution of zonal leakage coefficients with adaptive covariance inflation for scenario B (upper row), C (middle row) and D (lower row) (damping factor $\alpha = 0.2$).

change in L at day 155 due to covariance inflation. Especially for an updating frequency of 2 days this increase in ensemble variance is already rather high for certain leakage zones. For an updating frequency of 1 day (data not shown) this increase in ensemble variance is even higher which leads to numerical problems in the groundwater model due to rather extreme L values. Hence, a simulation with an updating frequency of one day could not be performed successfully. Nevertheless, updating frequencies of 2 or 5 days together with covariance inflation improved the adaptation of L considerably in terms of response time.

3.6 Discussion

The update of L with EnKF showed some general characteristics among all scenarios. In almost every case all zonal mean values of L were updated by EnKF in order to follow the trend of the reference run. For the scenario with either an increase or decrease of L the updated zonal ensemble means were quite close to the reference values at the end of the simulation period. However, the adaptation time to achieve this improvement was somewhat high within all scenarios. This also became obvious in the scenario where a flooding and a sedimentation event were combined within the simulation period. Here, the slow adaptation led to the effect that the changes in zonal ensemble means were within a smaller margin and the extreme values of the reference run were never reached.

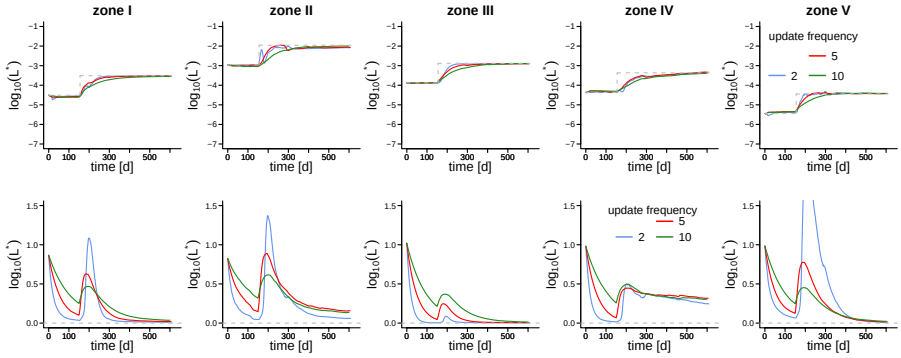

FIGURE 3.18: Temporal evolution (period January 2004 - August 2005) of ensemble mean (upper row) and ensemble standard deviation (lower row) of zonal leakage coefficients for different updating frequencies of piezometric heads and leakage coefficients with covariance inflation (simulation scenario A).

A reason for the slow adaptation may lie in the rather rapid decrease of ensemble spread during the simulations. The decrease of variance is already obvious in the time before a change happens in the L values of the reference run and proceeds as the L values are adapted by EnKF. The lowering of the ensemble spread before a change in L occurs in the reference run is a native feature of EnKF. In this case the zonal ensemble means are close to the reference values and because of this the errors in piezometric heads are rather small. Therefore, the filter 'trusts' the ensemble means and adapts the extreme values of the ensemble towards the ensemble mean what consecutively lowers the ensemble spread. However, this decrease of variance during the period of constant L values then possibly hampers the adaptation by EnKF towards the changed L values. Directly after the sudden change of L, differences between simulated and measured piezometric heads become larger, but the limited ensemble variance implies that the model predictions have a relatively large weight in the EnKF updating step, limiting the influence of the observations and slowing down the adaptation of L. The use of adaptive inflation leads to a faster adaptation of L towards the reference values and at the same time to a more precise determination of L at the end of the simulation period compared to the use of EnKF without inflation. In general, the adaptive inflation method seems to be robust to time-variant model parameters and it also honors changes in the prediction capability of the forward model by increasing the variance for a larger prediction error.

In the experiments it was also found that increasing the updating frequency is not necessarily a straightforward solution to achieve a shorter response time of EnKF because increasing the updating frequency leads to a faster decrease of ensemble variance especially in periods where the river bed is stable. This leads to some overconfidence of model parameters which influences the update of parameters negatively when there is

a change in river bed conditions. On the contrary, when covariance inflation is used in the EnKF updating scheme a positive effect of updating frequency on the adaptation time of L could be found due to the regulation of ensemble variance by this method. However, even with a higher updating frequency of L together with covariance inflation there is a certain time lag until EnKF responds to instantaneous changes of the river bed. Such instantaneous changes are likely to occur in reality, e.g., as a consequence of flooding events within a typical time period from hours to days. When such changes in the river bed are persistent over a certain time period EnKF will be able to adapt model parameters gradually within several assimilation cycles (depending on the settings for meta parameters such as updating frequency or damping factor). This means that also predictions of states will improve step by step until EnKF adapts to the new parameter values. However, when there are very frequent fluctuations in river bed properties that are faster than the assimilation frequency or even the time step of the model, EnKF will only capture the effective changes of the river bed and smooth them temporally. For such changes one would have to increase the temporal resolution of the forward model in order to reduce the effective response time of EnKF but this would probably also require a higher temporal resolution of measurements which is not possible in many cases.

The performance of EnKF with respect to seasonal variation of L caused by temperature changes of the river showed that the ensemble means of L for three of the five leakage zones principally followed the trend of the reference run although the whole magnitude of the change was not reached through updates with EnKF. For the other two zones changes of the ensemble mean of L were observable but did not correspond well to the evolution of L values of the reference run. The absolute changes of L were far lower for this scenario compared to the flooding and sedimentation cases. As a consequence, the errors at observation points as well as the correlations between the piezometric head data at the observation points and the zonal leakage coefficients were lower what might have led to a lower adaptation for two of the zones. Nevertheless, the results showed that even for small changes of L a correction with EnKF is principally possible.

The results for the influence of spatial patterns on the update with EnKF showed that EnKF is also able to detect changes in L that only occur at a certain location of the river reach. This might be relevant when the flow regime and thus the sedimentation/scouring regime is not homogeneous within the river, e.g., due to dams or weirs or due to a meandering of the river. However, a prerequisite that allows an optimal spatial update of L with EnKF in a real-world case is that the position of leakage zones corresponds to the sediment dynamics in the river bed. Certainly, alternative parameterization methods like pilot points laid out over stochastic fields of L are an interesting alternative which was not investigated in the context of this study.

EnKF was also able to correct for a bias in the initial ensemble which is important for a real-world scenario because it is often difficult to achieve a good initial guess of L values that provide a good agreement between simulated and measured states due to their high variability in natural settings. However, a correction of ensemble bias will require a sufficient initial ensemble spread of L.

Several different other tests were performed for evaluating the performance of EnKF for updating L. The ensemble size was found not to be too small, because results for an ensemble twice as large were not better. The used damping parameter was according to the suggestions of Hendricks Franssen and Kinzelbach (2008) and increasing it gave worse results except for the simulations where adaptive covariance inflation was used.

The sensitivity towards the amount of observation points showed that the ability of EnKF to correct for the time-varying L values generally increased with an increasing number of observation points. However, the results also showed that even with a low number of observation points (e.g., 5 or 10) the time-varying L values of EnKF could be reproduced quite well (150 days after the leakage jump the RMSE for L was reduced 50% for 10 observations and 20% for 5 observations compared to unconditional simulations). This may also be important for real-world applications because usually the amount of available time series of head data for a particular site is rather limited. For the study site the utilization of 100 observation points for the base scenarios was reasonable because for the real world case 87 piezometer data are available for this site on a daily basis. A doubling of the number of observation points from 100 to 200 did not significantly increase the performance of EnKF. This might be related to the fact that the simulations with 100 observation points already had a relatively high information content which was sufficient for the observed adaptations. Thus, the additional 100 observations points possibly only contained redundant information.

In general, the calibration of time-dependent L with EnKF using a limited number of piezometers is possible, with the limitations indicated before. This is probably the first work where a systematic approach to calibrate time-dependent L was proposed, carefully tested and shown to be feasible. A point of criticism could be that this approach only adapts L with help of indirect observations, without trying to predict the changes of L directly. However, both direct observations of modifications of L and deterministic prediction of changes of L are difficult and not possible at large scales. If indirect methods can reliably detect changes of L, this will provide new information at larger scales that can be used to better understand the mechanisms behind the changes of L. An additional limitation of the methodology followed in this study is that L is updated, and not the two parameters which constitute L, the river bed thickness and river bed

hydraulic conductivity. Although it would have been desirable to distinguish between the two parameters, this was beyond the scope of this study:

1. Measurement data most probably do not allow for differentiating between changes in river bed thickness and river bed hydraulic conductivity.
2. A very high resolution modeling of the river bed (on the cm scale) would be needed and many more grid cells would have to be included (now the model already has nearly 100,000 nodes and 173,599 elements).
3. In order to truly represent the dynamics of the river bed, the modeling grid should be adaptive and allowed to change over time. Such an approach is challenging in the context of forward model runs, but in the context of inverse modeling/data assimilation not yet feasible.

It is of course always a question whether the results found in this study are related to specific conditions at this site. It is possible that the groundwater management activities (pumping, artificial recharge) provide additional information which helps to constrain the estimation of L. Some of the simulation scenarios were also repeated without these management activities, but results were very similar.

3.7 Conclusions

In this chapter it was investigated to what extend the Ensemble Kalman Filter is able to correct states and parameters of a groundwater model for temporal changes in the hydraulic properties of a river bed. For this purpose, different synthetic scenarios were created in which the river bed conductivities followed certain temporal patterns that should imitate natural river bed dynamics. Calculations were based on a 3D model of the Limmat aquifer (Zurich) and the updating procedure for the model states and parameters with the Ensemble Kalman Filter was done with piezometric head data of the corresponding synthetic reference simulations.

Results for the different scenarios indicate the principal capability of EnKF to account for changes in river bed conductivity. This was shown for different types of major changes of the river bed (i.e., erosion of the river bed due to a flooding event, sedimentation and a combined scenario) in which EnKF correctly adjusted L values of the ensemble towards the reference values with a good overall performance at the end of the simulations. Also seasonal changes with smaller fluctuations of L related to the temperature dependency of L could in part be compensated by EnKF. Furthermore, EnKF was able to handle and

correct for different types of uncertainty in the assimilation process (uncertain hydraulic conductivities of the aquifer, biased initial ensemble). One drawback is the relatively long adaptation time that is needed by EnKF to adjust to new L values. In the simulations it took about 150 days until EnKF corrected the ensemble for an instantaneous change in L of one log unit. For modifications of L with a longer time duration like a sedimentation event the delayed response of EnKF also was observed. For real-world applications it will depend on the time scale of river bed dynamics whether EnKF reasonably catches changes in L. Frequent changes in river bed characteristics will only in part be captured by data assimilation if L is not updated very frequently which means that EnKF just adjusts L for effective changes within a given time period. However, experiments with an adaptive covariance inflation approach suggest that the performance of EnKF to capture time-variant model parameters can be generally improved by this method as it reduced the total adaptation time and increased the overall accuracy of the parameter update.

In summary, from a practical point of view the use of data assimilation with EnKF seems to be a promising way to account for changes of river sediments in real time models because of its capability to account for different changes of the river bed even if they have a low magnitude and because it is also able to handle different sources of uncertainty within the modeling process. Also the sensitivity analysis with respect to the numbers of observation points underpins the usability of EnKF for real time models because it showed that even with a low number of observations, an often encountered situation in practice, it is possible to capture changes in river bed conductivities.

Chapter 4

Characterization of heterogeneous river bed properties*

4.1 Introduction

It is now well known that rivers and streams closely interact with the adjacent groundwater body (Bouwer and Maddock, 1997; Winter, 1999; Sophocleous, 2002). These interactions have a number of consequences on the hydrological, chemical and biological environment around streams. For example, the resulting exchange fluxes between these two compartments influence the regional water balance and groundwater flow (Woessner, 2000) and thus also affect management activities close to streams, such as river bank filtration (Zhang et al., 2011; Schubert, 2002). Additionally, the different chemical composition of river water and groundwater also has implications on chemical and ecological processes around streams (Brunke and Gonser, 1997; Sophocleous, 2002).

The mechanisms of exchange between river systems and aquifers are complex and mainly depend on the piezometric head difference between stream and aquifer, the form of the river bed, hydraulic properties of the river bed and the adjacent aquifer and the state of hydraulic connection between river and groundwater (Cardenas et al., 2004; Boano et al., 2006; Genereux et al., 2008; Brunner et al., 2009). Exchange fluxes can exhibit a high degree of spatial and temporal variability what makes the prediction of exchange fluxes challenging. This variability of exchange fluxes is often related to the spatial heterogeneity of hydraulic conductivities in the river bed and the adjacent aquifer (Conant, 2004; Rosenberry and Pitlick, 2009b; Genereux et al., 2008). Calver (2001) compared

*adapted from: Kurtz, W., Hendricks Franssen, H.-J., Brunner, P., and Vereecken, H. (2013a). Is inversion based high resolution characterization of spatially heterogeneous river bed hydraulic conductivity needed and possible? *Hydrol. Earth Syst. Sci. Discuss.*, 10(5):5831–5873

literature data on river bed permeabilities which ranged from 10^{-9} to 10^{-2} ms^{-1} with a concentration of values in the range of 10^{-7} to 10^{-3} ms^{-1}. A striking feature in this data compilation is that estimated river bed permeabilities can also vary considerably for a single measurement site. This variability of hydraulic river bed properties can be found at different scales along a river reach. Genereux et al. (2008) determined river bed conductivities with permeameter tests for 46 locations of a 262 m long river reach. They observed a spatial variation in hydraulic conductivity of nearly four orders of magnitude ranging from approximately 1×10^{-7} to 7.5×10^{-4} ms^{-1}. They also found that measured river bed conductivities had a bimodal distribution and tended to be higher in the middle of the stream. Hatch et al. (2010) estimated river bed conductivities along a 11 km long river reach of Pajaro River and determined values ranging from 10^{-6} to 10^{-4} ms^{-1}. Springer et al. (1999) determined hydraulic conductivities for five reattachment bars of Colorado river over a range of 200 miles. Measured hydraulic conductivities varied over 2 orders of magnitude within the reattachment bars and differences between the medians of the five reattachment bars were up to one order of magnitude.

Different modeling studies have already tried to assess the effect of river bed and aquifer heterogeneity on the prediction of exchange fluxes between streams and groundwater. For example, Bruen and Osman (2004) investigated the impact of the heterogeneity of aquifer hydraulic conductivity on river-aquifer exchange fluxes with a synthetic 2D stream-aquifer model. They compared Monte Carlo (MC) simulations using heterogeneous fields of hydraulic conductivity with simulations using homogeneous fields. This comparison was made for different geostatistical parameters and connection regimes between river and aquifer. They found that the uncertainty in fluxes increases with an increasing degree of heterogeneity. They also found that a homogeneous model of hydraulic conductivities gave similar results as their MC simulations under connected conditions whereas it gave different predictions when river and aquifer were disconnected and unsaturated conditions were present below the river bed. Fleckenstein et al. (2006) investigated the effect of large scale aquifer heterogeneity on seepage fluxes. They compared simulation results for six realizations of geostatistically simulated facies distributions with a homogeneous aquifer model and found comparable net seepage fluxes for the different models. However, they also identified that the different facies distributions show considerable variability with respect to the spatial distribution of seepage fluxes and the state of connection between river and aquifer. Kalbus et al. (2009) investigated the effect of heterogeneous conductivities within the streambed and the adjacent aquifer by simulating 2D groundwater flow and heat transport using the leakage concept. They found that the heterogeneity of the aquifer conductivity has more impact on the fluxes than the one of the streambed. However, they also mention that homogeneous streambeds lead to an unrealistic homogenization of water fluxes between river

and aquifer. Frei et al. (2009) simulated the spatio-temporal distribution of seepage fluxes for a losing river reach in a MC framework. They applied a hydrofacies model for the distribution of hydraulic conductivities and found that highly permeable parts of the river reach (∼50% of total length) make up 98% of total seepage within their simulations. They argue that heterogeneity at the hydrofacies scale dominates the spatial pattern of river-aquifer interactions and that within-facies heterogeneity is of minor importance.

These different studies emphasize that the incorporation of heterogeneity in models for river-aquifer exchange can be important for a reliable prediction of exchange fluxes. In practical applications river bed conductivities are mostly estimated through calibration but heterogeneity is often neglected in the calibration procedure. One reason is that measurements of river bed conductivities are usually scarce and an estimation of the corresponding heterogeneity would require intensive field measurements. Especially for larger streams in-situ measurements are difficult to perform because of the higher discharge. As a consequence, in most cases there is only limited prior information about the spatial variability of hydraulic parameters for a specific site. Another reason is that the computational demand for inversions with gradient-based methods and also the complexity of the inversion increases with a higher resolution representation of heterogeneity in the model. Due to a lack of prior knowledge on the magnitude and variability of river bed properties and in order to ease the inversion procedure, leakage parameters are often lumped together, i.e., the underlying heterogeneity of river bed properties is reduced to a few different leakage zones which are used in the inversion. Irvine et al. (2012) carried out a systematic analysis on the simplification of heterogeneity to quantify its implications on the prediction of infiltration fluxes. They simulated infiltration curves (i.e., the relationship between water table depth and infiltration flux) for a variety of heterogeneous distributions of river bed conductivities. Different data points from these synthetic infiltration curves were then used to calibrate models with a homogeneous distribution of river bed conductivities. Forward simulations with the derived homogeneous values of river bed conductivities were subsequently used to compare the simulated infiltration curves with the equivalent ones for the fully heterogeneous medium. They found that the calibrated homogeneous models reproduced exchange fluxes well when the state of connection between river and aquifer was equal for calibration and prediction of the homogeneous models. However, when the state of connection was transitional or differed between calibration and prediction, the homogeneous models could not adequately reproduce the infiltration fluxes of the corresponding heterogeneous references.

One way to account for the underlying heterogeneity of river-aquifer systems in the calibration of groundwater models in a stochastic framework are data assimilation techniques, like Ensemble Kalman Filter (EnKF) (Evensen, 1994). EnKF and its variants

have already been applied successfully for the characterization of heterogeneous subsurface properties in groundwater modeling. Examples are the work of Chen and Zhang (2006); Hendricks Franssen and Kinzelbach (2008) and Nowak (2009) who assimilated piezometric heads with EnKF to improve the estimation of hydraulic conductivity fields. Sun et al. (2009) compared the performance of different deterministic ensemble filters for subsurface characterization. Liu et al. (2008) and Li et al. (2012) used tracer data to infer hydraulic conductivity (and porosity) fields. The studies of Jafarpour and Tarrahi (2011) and Huber et al. (2011) addressed the influence of variogram uncertainty and prior information in the initial parameter ensemble on the estimation of hydraulic conductivity fields with EnKF. Zhou et al. (2011) and Schöniger et al. (2012) investigated techniques to account for non-Gaussianity in the assimilation with EnKF and Camporese et al. (2009b) jointly assimilated piezometric heads and discharge data for subsurface characterization. A general advantage of ensemble based data assimilation with EnKF and its variants is that they are able to calibrate model parameters based on the forward propagation of an ensemble of different parameter fields and therefore explicitly account for the high variability of hydraulic parameters in natural settings. Therefore, this methodology should also be well suited for the characterization of highly variable river bed properties. In this chapter it is focused on the question whether the estimation of a few effective values for river bed hydraulic conductivity can reproduce spatially and temporally strongly variable exchange fluxes between river and aquifer with the use of data assimilation. For this purpose, different ensembles of leakage parameters are compared that either resemble the full heterogeneity of a synthetic reference field or where three different degrees of zonation are used. The specific research questions are:

- To what degree does a zonation of river bed properties change predicted exchange fluxes between river and aquifer compared to a full representation of river bed heterogeneity?
- Is EnKF able to identify the main structural features of a fully heterogeneous field of river bed conductivities through assimilation of piezometric head measurements?
- How does EnKF perform for different parameterization approaches (i.e., detailed representation of heterogeneity versus few zones) under conditions with different amount of observation data?

4.2 Data assimilation with the Ensemble Kalman Filter

4.2.1 General description of the data assimilation algorithm

EnKF is a sequential data assimilation approach which can be utilized to improve the prediction capability of a particular model in a MC framework. The methodology was originally applied for atmospheric and oceanographic models (e.g., Evensen, 1994; Houtekamer and Mitchell, 1998) and later used in modified variants, which include parameter estimation in surface hydrology (e.g., Moradkhani et al., 2005) and subsurface hydrology (e.g., Chen and Zhang, 2006; Hendricks Franssen and Kinzelbach, 2008; Liu et al., 2008; Nowak, 2009). The basic idea of EnKF is that an ensemble of different model realizations (with different forcings and/or parameters) is propagated forward in time until measurements of state variables become available. The prediction of state variables is improved by optimally combining the ensemble of model predictions and measurement data where measurement errors and the uncertainty of model predictions are optimally weighted. EnKF can also be used to estimate model states and model parameters simultaneously. In this case an augmented state vector approach (e.g., Chen and Zhang, 2006; Hendricks Franssen and Kinzelbach, 2008) can be utilized in which the model states $\boldsymbol{\psi}$ and the model parameters $\boldsymbol{\phi}$ are combined in the state-parameter vector $\boldsymbol{\Psi}$:

$$\boldsymbol{\Psi} = \begin{pmatrix} \boldsymbol{\psi} \\ \boldsymbol{\phi} \end{pmatrix} \tag{4.1}$$

For each assimilation cycle (i.e., at times when measurements become available) EnKF then performs a Bayesian update on the ensemble of the state-parameter vector $\boldsymbol{\Psi}$:

$$p(\boldsymbol{\Psi} \mid \boldsymbol{y}^0) \propto p(\boldsymbol{y}^0 \mid \boldsymbol{\Psi}) p(\boldsymbol{\Psi}) \tag{4.2}$$

where $p(\boldsymbol{\Psi} \mid \boldsymbol{y}^0)$ is the posterior (updated) distribution of the state-parameter vector $\boldsymbol{\Psi}$ given the observations $\boldsymbol{y}^0$, $p(\boldsymbol{y}^0 \mid \boldsymbol{\Psi})$ is the likelihood of measurements $\boldsymbol{y}^0$ given $\boldsymbol{\Psi}$ and p($\boldsymbol{\Psi}$) is the prior distribution of $\boldsymbol{\Psi}$. The prior of the states $\boldsymbol{\psi}$ (as part of $\boldsymbol{\Psi}$) is usually obtained by advancing each realization i of the ensemble with a model M

$$\boldsymbol{\psi}_i^t = M(\boldsymbol{\psi}_i^{t-1}, \boldsymbol{\phi}_i, \boldsymbol{\zeta}_i) \tag{4.3}$$

where $\boldsymbol{\psi}_i^t$ is the state vector for the current time step (i.e., the forecast), $\boldsymbol{\psi}_i^{t-1}$ is the state vector for the previous time step, $\boldsymbol{\phi}_i$ are model parameters and $\boldsymbol{\zeta}_i$ are model forcings for realization i.

The posterior distribution of $\boldsymbol{\Psi}$ in Equation 4.2 is then calculated with the EnKF analysis scheme which consists of the following steps: First, the forecasted values of $\boldsymbol{\psi}$ at observation points have to be extracted from the ensemble:

$$\hat{\boldsymbol{\psi}}_i^t = \mathbf{H}\boldsymbol{\Psi}_i^t \tag{4.4}$$

where $\hat{\boldsymbol{\psi}}_i^t$ is the forecasted state vector at observation points for realization i and $\mathbf{H}$ is a matrix that extracts or interpolates $\hat{\boldsymbol{\psi}}_i^t$ from the state-parameter vector $\boldsymbol{\Psi}_i^t$.

Next, the measured states $\boldsymbol{y}^0$ have to be perturbed for an optimal functioning of the data assimilation algorithm in order to achieve the correct posterior variance (Burgers et al., 1998). This is done with the perturbation vector $\tilde{\boldsymbol{\epsilon}}$ which is composed of values drawn from a normal distribution $\mathcal{N}(0, \epsilon)$ with a mean of zero and a standard deviation that corresponds to the measurement error ϵ of the assimilated state variable:

$$\tilde{\boldsymbol{y}}_i = \boldsymbol{y}^0 + \tilde{\boldsymbol{\epsilon}}_i \tag{4.5}$$

where $\tilde{\boldsymbol{y}}_i$ is the perturbed measurement vector for realization i, $\tilde{\boldsymbol{\epsilon}}_i$ is the corresponding perturbation vector and $\boldsymbol{y}^0$ is the measurement vector.

Finally, the posterior distribution of $\boldsymbol{\Psi}$ is found by applying the following equation on each ensemble member i:

$$\boldsymbol{\Psi}_i^a = \boldsymbol{\Psi}_i^t + \alpha\mathbf{G}(\tilde{\boldsymbol{y}}_i - \hat{\boldsymbol{\psi}}_i^t) \tag{4.6}$$

where $\boldsymbol{\Psi}_i^a$ is the analysed (updated) state-parameter vector for realization i, $\boldsymbol{\Psi}_i^t$ is the forecasted state-parameter vector (with forecasted states from Equation 4.3), $\tilde{\boldsymbol{y}}_i$ is the perturbed measurement vector, $\hat{\boldsymbol{\psi}}_i^t$ is the forecasted state vector at observation points, α is a damping factor which is only used for parameter updates in order to decrease the effect of filter inbreeding (see Hendricks Franssen and Kinzelbach, 2008) and $\mathbf{G}$ is the Kalman gain matrix which is calculated as:

$$\mathbf{G} = \mathbf{C}\mathbf{H}^\top(\mathbf{H}\mathbf{C}\mathbf{H}^\top + \mathbf{R})^{-1} \tag{4.7}$$

where $\mathbf{C}$ is the full covariance matrix of $\mathbf{\Psi}^t$ and $\mathbf{R}$ is the covariance matrix of observation data $\boldsymbol{y}^0$. The Kalman gain $\mathbf{G}$ is calculated once for all ensemble members and weights the uncertainties in the prediction of $\mathbf{\Psi}$ from the forward simulations with the measurement error of $\boldsymbol{y}^0$. In the analysis step (Equation 4.6) the weighting factors of $\mathbf{G}$ are used to correct each member of $\mathbf{\Psi}^t$ with the residuals at observation points (bracketed term in Equation 4.6). In order to derive $\mathbf{G}$ it is not necessary to calculate the full covariance matrix of $\mathbf{\Psi}^t$ but it is sufficient to calculate the covariances between $\mathbf{\Psi}^t$ and $\hat{\boldsymbol{\psi}}^t$:

$$\mathbf{CH}^\top = \begin{pmatrix} \mathbf{C}_{\boldsymbol{\psi}^t\hat{\boldsymbol{\psi}}^t} \\ \mathbf{C}_{\boldsymbol{\phi}\hat{\boldsymbol{\psi}}^t} \end{pmatrix} \tag{4.8}$$

4.2.2 Specific usage of EnKF for river-aquifer interactions

In this study the focus is on the investigation of river-aquifer exchange fluxes. Thus, the model states of interest are piezometric heads $\boldsymbol{h}$ and the most relevant model parameters are river bed hydraulic conductivities which are expressed as leakage coefficients $\boldsymbol{L}$. Therefore, the state-parameter vector $\mathbf{\Psi}$ which was introduced in the previous section is composed of $\boldsymbol{h}$ and $\log(\boldsymbol{L})$. The model $M(\boldsymbol{\psi_i}^{\boldsymbol{t-1}}, \boldsymbol{\phi_i}, \boldsymbol{\zeta_i})$ that is used to advance $\boldsymbol{h}$ in time is a groundwater model that is capable of simulating variably saturated flow and that includes a parameterization to simulate river-aquifer exchange fluxes. The observation data $\boldsymbol{y}^0$ consist of measurements of piezometric heads in the aquifer. The covariance matrix $\mathbf{R}$ includes the measurement errors of observation data on the diagonal but covariances between observation points are assumed to be zero (i.e., measurement errors are assumed to be independent).

4.3 Model description

In order to test the role of zonation of river bed properties synthetic numerical experiments were performed with a three-dimensional finite element model that mimics a real-world case of the Limmat aquifer in Zurich (Switzerland). A schematic representation of the study site is shown in Figure 4.1. In this model the aquifer is discretized into 92015 nodes, 173599 elements and 25 layers. The variably saturated flow equation was solved numerically with the groundwater modeling software SPRING (Delta h Ingenieurgesellschaft mbH, 2006).

The boundary conditions for this model are given schematically in Figure 4.1. Groundwater recharge is imposed as a flux boundary condition (forcing) on the first model layer.

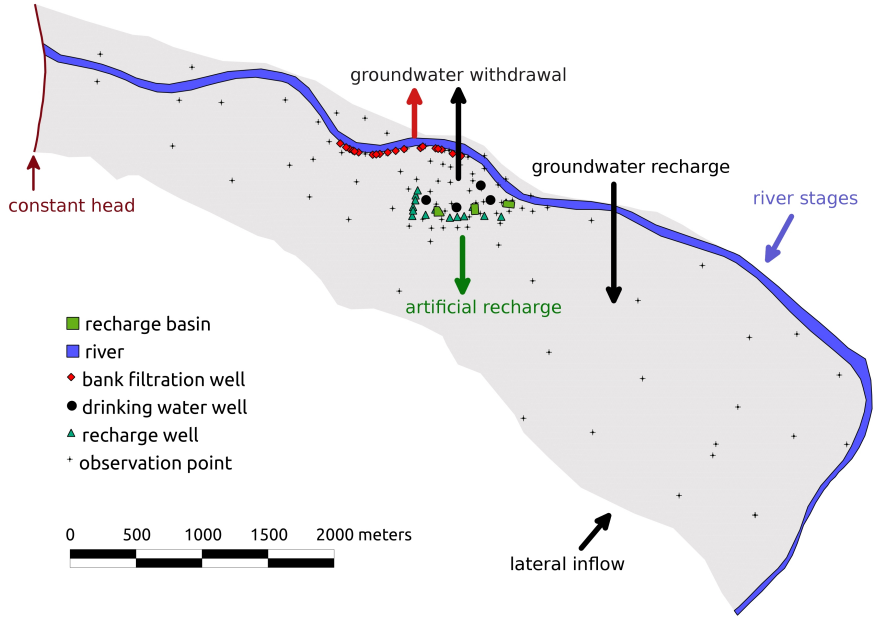

FIGURE 4.1: Schematic representation of model domain and boundary conditions.

Lateral inflows on the south face of the model were also treated as flux boundary conditions. Within the model domain also management activities take place: Groundwater is withdrawn close to the river through several bank filtration and drinking water wells. The pumped water from the bank filtration wells is redistributed to the aquifer through three recharge basins and several recharge wells which are located south of the drinking water wells. On the western face of the model a constant head boundary condition is imposed. The two rivers in the model (Sihl and Limmat) are located at the eastern and northern boundary of the model domain respectively and river stages are imposed on each river node of the model. River-aquifer exchange fluxes are calculated in SPRING according to the leakage principle:

$$Q_{leak} = A_{leak} L (h^{river} - h^{gw}) \tag{4.9}$$

where Q_{leak} is the leakage flux between river and aquifer [L^3T^{-1}], A_{leak} is the area through which the flux occurs [L^2], h^{river} is river stage [L], h^{gw} is groundwater level underneath the river [L] and L is leakage coefficient [T^{-1}] which is a lumped parameter for the hydraulic conductivity and the thickness of the river bed.

All model forcings (recharge, lateral inflows, river stages, pumping rates) are transient and based on real-world data and details on the calculation of these forcing data can

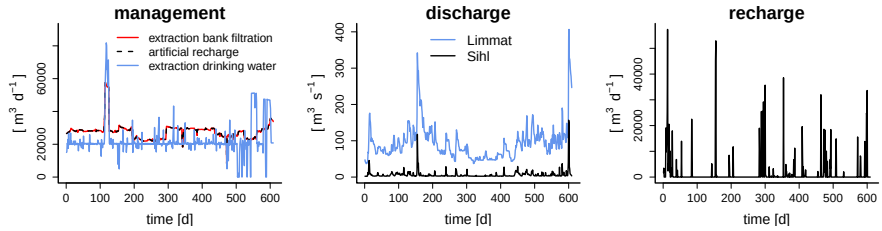

FIGURE 4.2: Forcing data for synthetic experiments. Represented are total amounts of artificial recharge, extraction from bank filtration and extracted drinking water (left), as well as river discharges (middle) and total recharge amount over the model domain (right), for a period of 609 days (January 2004 - August 2005).

be found in Hendricks Franssen et al. (2011). Figure 4.2 summarizes the corresponding values.

4.4 Synthetic experiments

The general setup of the synthetic experiments consists of the following steps:

1. Generation of ten spatially heterogeneous distributions of $\log(L)$ with Sequential Gaussian Simulation (SGS).
2. Finite elements solution of the transient variably saturated flow equation (for 609 days) using SPRING. A solution is calculated for each of the ten generated $\log(L)$-fields of step 1. The calculated piezometric heads and river-aquifer exchange fluxes for these ten simulations serve as the ten "true" reference solutions.
3. Generation of $\log(L)$ ensembles (100 realizations) for a fully heterogeneous case and three different zonations (5, 3 and 2 leakage zones)
4. For each of the ten references (step 1 and 2): assimilation of hydraulic head data from step 2 with EnKF for the four $\log(L)$ ensembles of step 3.

This procedure is used for three scenarios which differ in the degree of heterogeneity of $\log(L)$ reference fields and in the information content of the initial ensemble:

A strongly heterogeneous $\log(L)$-field for reference and initial ensemble

B moderately heterogeneous $\log(L)$-field for reference and initial ensemble

C strongly heterogeneous $\log(L)$-field with prior information in the initial ensemble

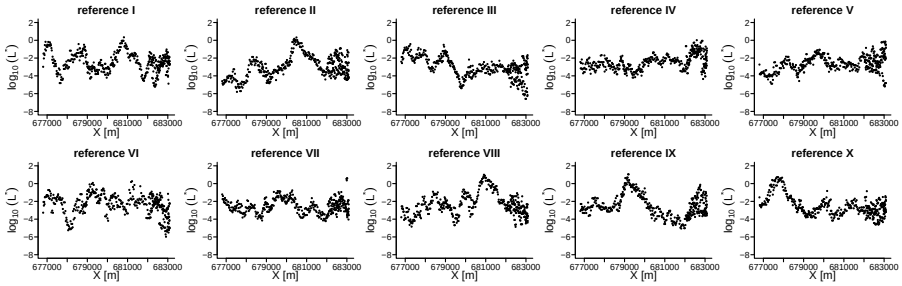

FIGURE 4.3: Reference fields of leakage coefficients for scenario A. The x-axis shows the x-coordinate according to the Swiss coordinate system. In the eastern part of the model domain the rivers Limmat and Sihl have overlapping x-coordinates and therefore for this part two leakage values are given.

Scenario A serves as a base scenario for which the relevant results of the simulation experiments are presented in detail. The results for scenarios B and C are then discussed with respect to deviations from scenario A. In this sense, Scenario B is utilized to assess the performance of data assimilation for different degrees of heterogeneity and scenario C should give insight into the value of prior information for the data assimilation with EnKF.

4.4.1 Reference fields

The reference fields of leakage coefficients for scenario A were generated by adding perturbation fields to a predefined mean value of -2.78 $\log(\mathrm{ms}^{-1})$. The perturbation fields were generated by SGS with the code GCOSIM3D (Gómez-Hernández and Journel, 1993) for rivers Sihl and Limmat. These perturbation fields have a grid size of 50 m. A spherical variogram was chosen for geostatistical simulations of the ten perturbation fields. The nugget was set to 0 $\log(\mathrm{ms}^{-1})$ for all simulations. The range of the variograms was sampled from a uniform distribution with values ranging from 1000 to 2000 m for each reference field. Values for the sill were also sampled from a uniform distribution ranging from 1 to 2 $\log(\mathrm{m}^2\mathrm{s}^{-2})$. The simulated fields were directed onto the main axis of the rivers and the leakage coefficient for each river node $\log(L)$ was determined by the overlying grid block of the geostatistically simulated perturbation field plus the predefined mean value of -2.78 $\log(\mathrm{ms}^{-1})$. The different reference fields of leakage coefficients are shown in Figure 4.3 along the x-axis of the model domain.

For the creation of reference fields for scenario B a similar methodology as for scenario A was applied. The only difference between these two scenarios is that for scenario B a sill between 0.1 and 0.5 $\log(\mathrm{m}^2\mathrm{s}^{-2})$ was used what results in a lower degree of variability for these references.

TABLE 4.1: Predefined zonal leakage values for generation of reference fields for scenario C. Leakage zones are numbered from west to east.

leakage zone	$\log(L^*)$ $[\log(\mathrm{ms}^{-1})]$
I	-5.51
II	-1.96
III	-3.88
IV	-5.37
V	-6.44

For scenario C the reference fields of $\log(L)$ have a predefined zonation with five leakage zones whose spatial location corresponds to the one of ensemble Z_5 (see below). The predefined zonal values for $\log(L)$ are summarized in Table 4.1. Similar to scenario A, perturbation fields were added to these predefined zonal values. These perturbation fields were created in a similar way as scenario A with a nugget of 0 $\log(\mathrm{ms}^{-1})$, a sill of 1 $\log(\mathrm{m}^2\mathrm{s}^{-2})$ and a range of 600 m. Compared to scenario A these reference fields include a higher contrast between different parts of the river reach (realized through the predefined zonation) and an additional component of interzonal variability (realized through the perturbation fields).

4.4.2 Zonation

For the assimilation experiments four ensembles of leakage coefficients were generated which differed in their spatial representation of heterogeneity. The first ensemble Z_{het} represents the full heterogeneity of the reference fields and the number of zones is equal to the number of river nodes (i.e., 457). The second ensemble Z_5 only represents 5 leakage zones which were positioned according to the main hydrological features of the river reach (i.e., position of two weirs, confluence of rivers Sihl and Limmat, management activities) which results in four leakage zones for river Limmat and one leakage zone for river Sihl. For the third ensemble Z_3 river Limmat is divided into two leakage zones and river Sihl is the third leakage zone. For the fourth ensemble Z_2 river Limmat is aggregated to one leakage zone and again river Sihl serves as a separate leakage zone. The spatial arrangement of leakage parameters for the fully heterogeneous case (Z_{het}) and the three zonation approaches (Z_5, Z_3 and Z_2)is depicted in Figure 4.4.

4.4.3 Ensemble generation

The generation of the ensembles for Z_{het} for the three scenarios corresponded closely to the generation of the respective reference fields. However, a higher degree of uncertainty

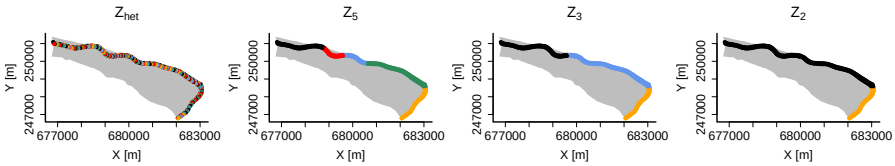

FIGURE 4.4: Spatial representation of heterogeneity for four parameter ensembles. In the fully heterogeneous case (Z_{het}) an individual leakage coefficient is assigned to each river node. For the zonated ensembles (Z_5, Z_3 and Z_2) each color corresponds to a separate leakage zone. The river nodes within a leakage zone share the same leakage coefficient.

TABLE 4.2: Default settings for data assimilation with EnKF.

parameter	value	unit
N_{real}	100	
N_{obs}	100 (10)	
α	0.1	
update frequency	10	d
$\epsilon(\boldsymbol{h})$	0.05	m

with respect to geostatistical parameter was used for the ensembles. For scenario A the range parameter varied between 50 and 5000 m and the sill value between 0.1 and 3.0 $\log(m^2s^{-2})$. For scenario B the sill for Z_{het} has values between 0.1 and 1.5 $\log(m^2s^{-2})$ and the range between 50 and 5000 m. For scenario C the ensemble for Z_{het} was generated with the same geostatistical parameters as for scenario A.

The ensembles for Z_5, Z_3 and Z_2 for each scenario were generated on the basis of the respective ensemble for Z_{het} by calculating the arithmetic average of $\log(L)$ values for each realization of Z_{het} according to the respective zonation scheme. For example, the value of $\log(L)$ for one of the five leakage zones of Z_5 for a single realization is calculated from the corresponding realization of Z_{het} by averaging the $\log(L)$ of Z_{het} that are within the respective zone of Z_5. This procedure is then repeated for all leakage zones and all realizations of Z_5. In Figure 4.5 the generated ensembles for scenario A are compared to reference field I.

4.4.4 Settings for data assimilation with EnKF

The meta parameters for data assimilation experiments for scenario A, B and C with EnKF are summarized in Table 4.2. For all three scenarios 100 observation points were used as input data for EnKF. Scenario A was additionally simulated with a lower amount of observations (10 measurements). The other settings for assimilation with EnKF were held constant for all scenarios.

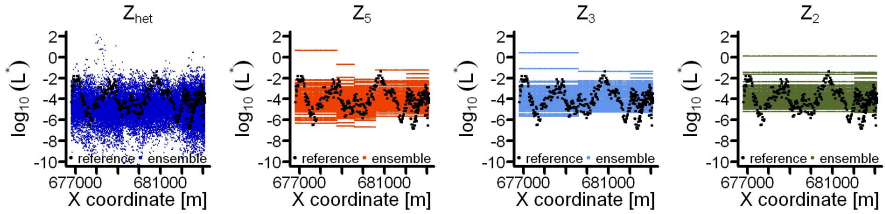

FIGURE 4.5: Initial ensembles of leakage coefficients (colored) and reference field I (black) for scenario A for all river nodes (rivers Limmat and Sihl) along x-axis of model domain.

4.4.5 Performance assessment of simulations

The performance of the data assimilation experiments is assessed by the prediction error of piezometric heads throughout the model domain, the prediction error of fluxes between river and aquifer and the correction of leakage coefficients during the update. For the prediction error of piezometric heads the Root Mean Square Error between the predicted mean piezometric head and the piezometric head of the reference ($\mathrm{RMSE_h}$) is calculated using:

$$\mathrm{RMSE_h(t)} = \sqrt{\frac{1}{\mathrm{N_{nodes}}} \sum_{i}^{\mathrm{N_{nodes}}} \left(\overline{h}_i(t) - h_i^{ref}(t)\right)^2} \tag{4.10}$$

where $\overline{h}_i$ is the mean piezometric head for model node i [L], h_i^{ref} is the piezometric head of the reference simulation for node i [L], $\mathrm{N_{nodes}}$ is the total number of model nodes and t is time step [T].

For the evaluation of river-aquifer exchange, either the evolution of the leakage fluxes over time $Q(t)$ or statistics for the total volume of water that was exchanged between river and aquifer during the whole simulation period ΔV_{tot} are presented:

$$Q(t) = \sum_{i}^{\mathrm{N_{leak}}} Q_i(t) \tag{4.11}$$

$$\Delta V_{tot} = \sum_{j}^{t_{tot}} \sum_{i}^{\mathrm{N_{leak}}} Q_{ij} \Delta t_j \tag{4.12}$$

where $Q(t)$ is the river-aquifer exchange flux over time [$\mathrm{L^3T^{-1}}$], $Q_i(t)$ is the leakage flux for river node i over time, $\mathrm{N_{leak}}$ is total number of leakage nodes, ΔV_{tot} is the volume of water that is exchanged between river and aquifer over the whole simulation period

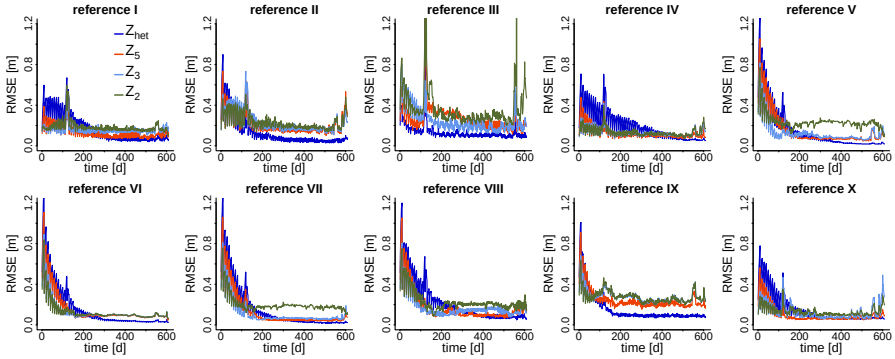

FIGURE 4.6: $RMSE_h$ of conditional simulations with EnKF for ten reference fields of leakage coefficients (scenario A). Four different ensembles are compared. EnKF jointly updated hydraulics heads and leakage coefficients with measurement data from 100 observation points.

$[L^3]$, Q_{ij} is the volumetric flux between river and aquifer for the i^{th} leakage node and the j^{th} time step $[L^3T^{-1}]$, Δt_j is time step [T] and t_{tot} is total number of time steps. $Q(t)$ was calculated direction dependent, i.e., fluxes from river to aquifer (positive) and fluxes from aquifer to river (negative) were summed up separately.

4.5 Results

4.5.1 Strongly heterogeneous case (scenario A)

Figure 4.6 compares $RMSE_h$ of the four $\log(L)$-ensembles for ten highly heterogeneous reference fields (scenario A). The highest improvement is observed for Z_{het} where $RMSE_h$ is consistently reduced to about 0.1 m among all references. For the other ensembles the performance in terms of $RMSE_h$ is more dependent on the specific reference. For example, $RMSE_h$ of Z_5 is similar to the one of Z_{het} for some references (e.g., IV, VIII and X) but is worse for other references (e.g., II and IX). A similar behavior can be observed for Z_3 and Z_2.

The updated net fluxes between river and aquifer are shown in Figure 4.7 for reference field I. For this reference field the updating with EnKF led to an improvement of the prediction of fluxes from river to aquifer for all four ensembles. Fluxes from aquifer to river were well reproduced by Z_{het} and Z_5 whereas for Z_3 and Z_2 a larger deviation between ensemble mean and true values was found. The ensemble variance of leakage fluxes decreases very fast where most of the decrease happens in the first 100 simulation days. One exception is the flux from aquifer to river for Z_{het}. The general decrease of

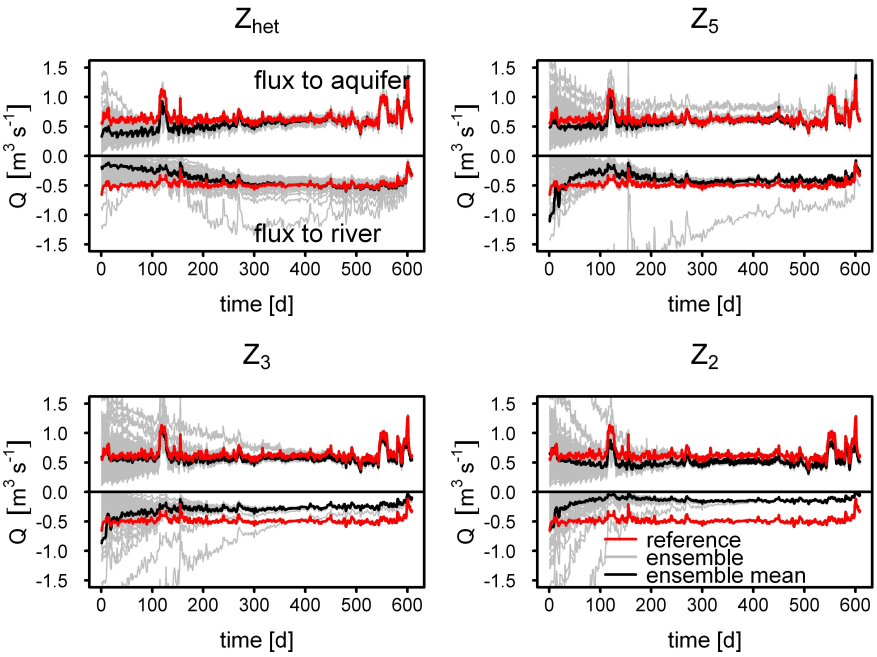

FIGURE 4.7: Cumulative directional fluxes between river and aquifer for conditional simulations with EnKF for four representations of spatial heterogeneity (scenario A). Results are shown for reference I. Fluxes from river to aquifer have a positive sign.

variance within the first 100 days is observable for all ten references whereas the higher variability for Z_{het} was a special feature of reference I.

An overview of the net exchange between river and aquifer for all ten references is given in Figure 4.8. Here the total amount of exchanged water summed over the complete simulation period (ΔV_{tot}) is displayed for each of the reference fields and for each of the zonation approaches. The net exchange for Z_{het} is very close to the net exchange of the respective reference and thus shows the best performance among the four ensembles. Z_5 is usually also very close to the net exchange of the references except for reference III where the net flux is greatly underestimated by this ensemble. Z_3 and Z_2 show a good fit for some references (e.g., reference IV) but the fluxes are significantly over- or underestimated for other references.

Figure 4.9 gives an example of the spatial distribution of exchange fluxes for time step 300 and reference IV. For Z_{het} the spatial distribution of exchange fluxes of the reference run is principally captured by the ensemble and the exchange fluxes of the reference run are within the uncertainty bounds of the ensemble. For Z_5, Z_3 and Z_2 some of the principal features of the reference run, i.e., the river parts with the highest positive

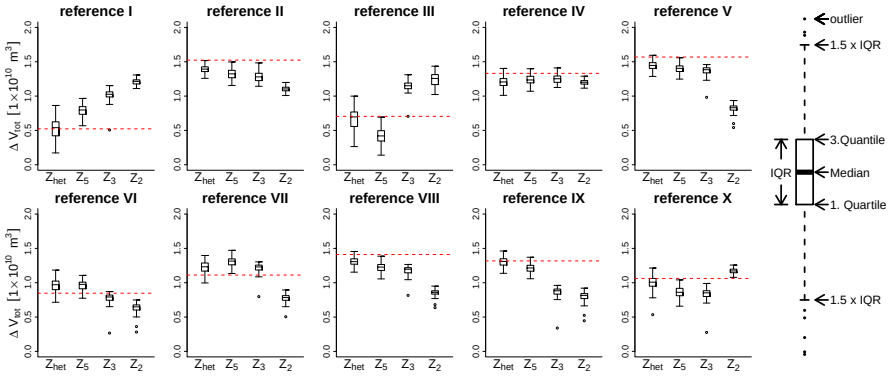

FIGURE 4.8: Total amount of water exchanged between river and aquifer over the whole simulation period (609 days) for scenario A. Red lines mark the water exchange for the different reference runs. On the right hand side the description of the boxplots is illustrated.

exchange fluxes, are also present although the reference fluxes are not any more within the uncertainty bounds of the zonated ensembles. In other parts of the river the exchange fluxes of the reference run are not present in the ensemble calculations of Z_5, Z_3 and Z_2, e.g., the negative fluxes in the western part of the model.

Figure 4.10 compares the initial ensembles of leakage coefficients with the updated ones at day 600 for reference I. In general, the updated ensembles at time step 600 have a smaller variance than the initial ensembles. For Z_{het} the ensemble at the end of the simulation period mostly covers the spatial pattern of the reference field. In some parts of the river Z_{het} still has a relatively high variance while in other parts variance is low and the spatial pattern of the ensemble is close to the pattern of the reference field. For Z_5 the mean values for the different zones remain more or less constant during the updates while the ensemble variance for the different zones strongly decreases for four of the five zones. For Z_3 and Z_2 also a very strong decrease in ensemble variance is visible.

4.5.2 Strongly heterogeneous case with lower observation density

In order to investigate how a lower density of observation points affects the results for the different zonation approaches the assimilation experiments for the first five reference fields of scenario A were repeated with piezometric head time series measured at only 10 points instead of 100. The overall error in terms of $RMSE_h$ for Z_5, Z_3 and Z_2 was comparable to the ones in the assimilation experiments with 100 observation points. For Z_{het} the overall deviations to the reference were slightly higher when only 10 observation

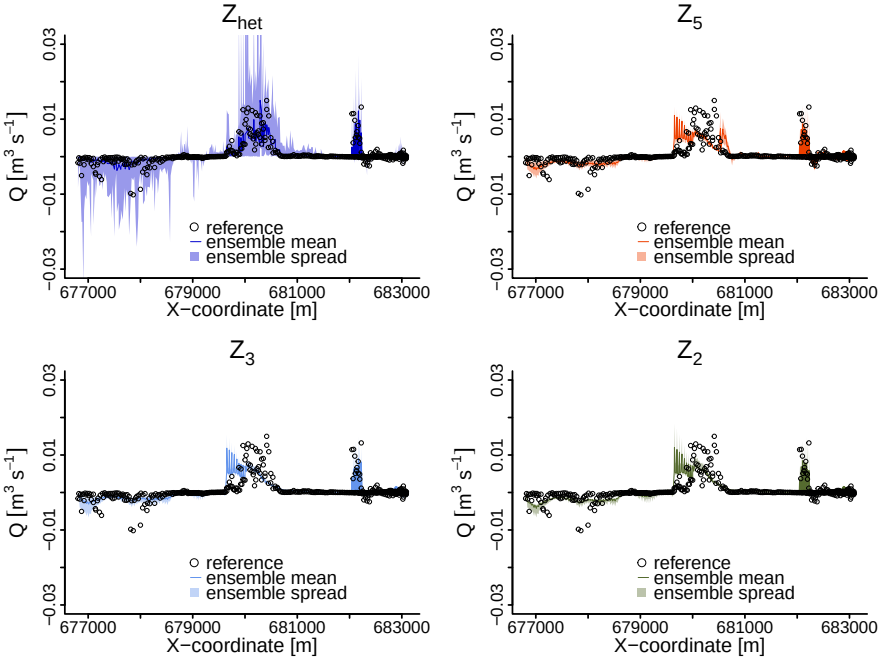

FIGURE 4.9: Fluxes between river and aquifer along x-axis of model domain for conditional simulations with EnKF at simulation day 300 (scenario A, reference IV). Fluxes from river to aquifer have a positive sign.

points were used but predictions were still slightly better than for the zonated ensembles. For Z_{het} the predicted mean fluxes in both directions (i.e., fluxes to river or to aquifer) were underestimated in most cases whereas there were no major differences for the other ensembles. Flux predictions for Z_{het} were also associated with a higher degree of uncertainty compared to the assimilation of 100 observations. Despite an underestimation of both fluxes from river to aquifer and fluxes from aquifer to river for Z_{het} the predicted net fluxes between river and aquifer were comparable to the simulations with 100 observation points, i.e., Z_{het} gave good results for all references. Net fluxes for the other ensembles were also similar to the assimilation of 100 measurements and especially for Z_3 and Z_2 higher deviations occurred for some references. The update of leakage coefficients for Z_{het} was not as good as for the assimilation of 100 observations. The main structural features of the reference fields were captured during the assimilation but the variability of the ensemble at the end of the simulation period was significantly higher when only 10 observations were assimilated (see Figure 4.11). From Figure 4.11 it becomes obvious that there are more extreme values than for the assimilation of 100 observations. This can be seen as a reason for the higher variability of fluxes for Z_{het}. The variability of $\log(L)$ for the other ensembles increased only marginally and also the

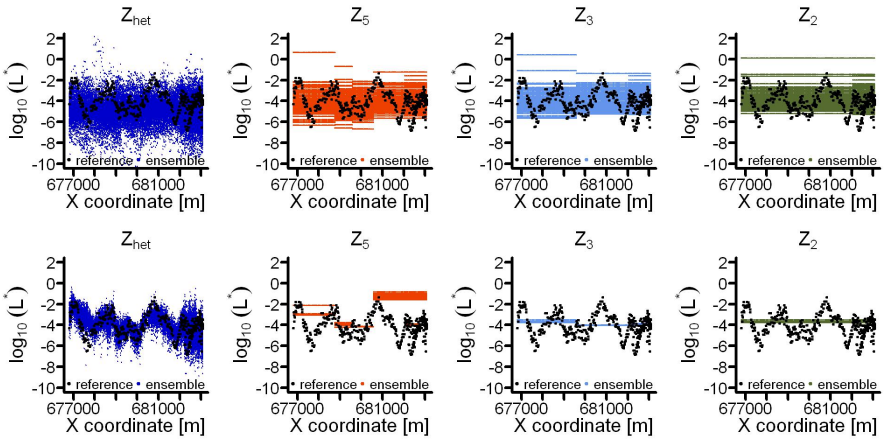

FIGURE 4.10: Ensembles of leakage coefficients (colored) and reference field (black) along x-axis of model domain at day 1 (upper row) and at day 600 (lower row) for scenario A.

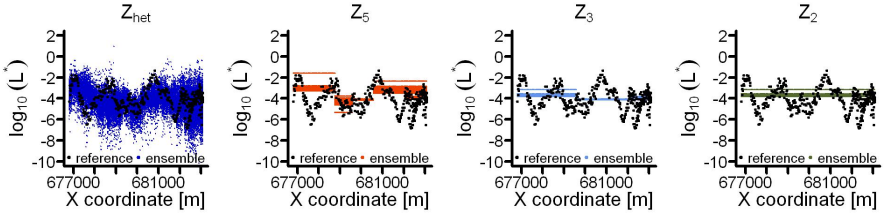

FIGURE 4.11: Ensembles of leakage coefficients (colored) and reference field (black) along x-axis of model domain at day 600 (lower row) for scenario A when only 10 observation points are available.

mean values for Z_3 and Z_2 were similar to the assimilation of 100 measurements.

4.5.3 Mildly heterogeneous case (scenario B)

For scenario B the variability of $\log(L)$-fields for the references and the initial ensembles was reduced. Results for this case show that $RMSE_h$ for Z_5, Z_3 and Z_2 correspond more closely to $RMSE_h$ of Z_{het}. Nevertheless, Z_{het} still shows the best performance in terms of $RMSE_h$ for all ten references. The temporal evolution of leakage fluxes for the ten references is captured well by all four ensembles. Compared to scenario A the systematic differences that occurred between reference fluxes and simulated fluxes were reduced (especially for Z_3 and Z_2). This is also reflected in the cumulative net exchange over the simulation period (Figure 4.12).

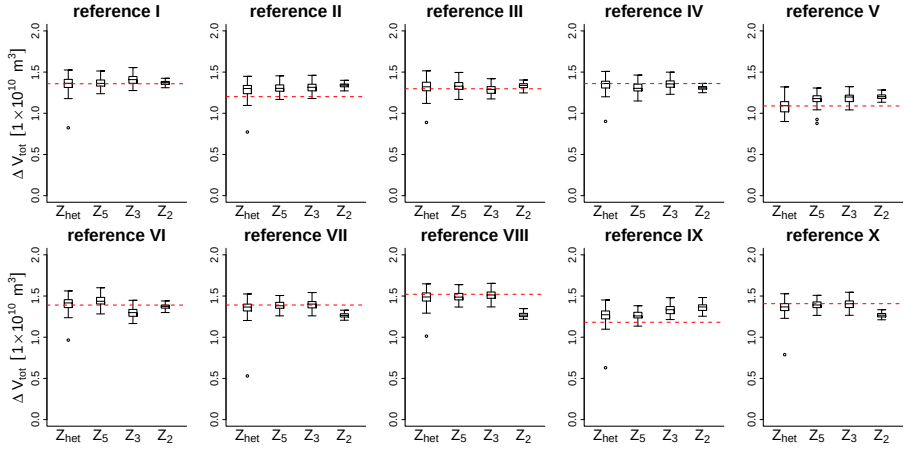

FIGURE 4.12: Total amount of water exchanged between river and aquifer over the whole simulation period (609 days) for conditional simulations with EnKF (scenario B). Red lines mark the water exchange for the different reference runs.

It can be seen that ensembles are generally closer to the reference values and this is especially pronounced for Z_3 and Z_2. But still there are some references where the uncertainty bounds of Z_2 do not cover the reference flux. Although the prediction of cumulative net fluxes for scenario B is better for ensembles with a lower number of leakage zones the spatial representation of fluxes is still worse for Z_2, Z_3 and Z_5 than for Z_{het} where the spatial distribution of leakage fluxes closely corresponds to the reference fluxes.

4.5.4 Strongly heterogeneous case with a predefined zonation (scenario C)

In scenario C the references include a predefined zonation with a relatively high contrast of $\log(L)$ between the individual zones. A second important feature of this scenario is that the location of leakage zones for Z_5 is similar to the ones of the references which means that the initial ensemble of Z_5 includes prior information on the spatial distribution of $\log(L)$.

$RMSE_h$ of Z_{het} and Z_5 are very similar for this scenario with slightly lower errors for Z_{het}. In contrast, Z_3 and Z_2 perform worse in terms of $RMSE_h$ compared to scenario A. For the net fluxes between river and aquifer a similar relation is found. Again Z_{het} and Z_5 show relatively similar values which are very close to the reference values whereas Z_3 and Z_2 consistently underestimate the net exchange what leads to a higher error compared to scenario A (Figure 4.13).

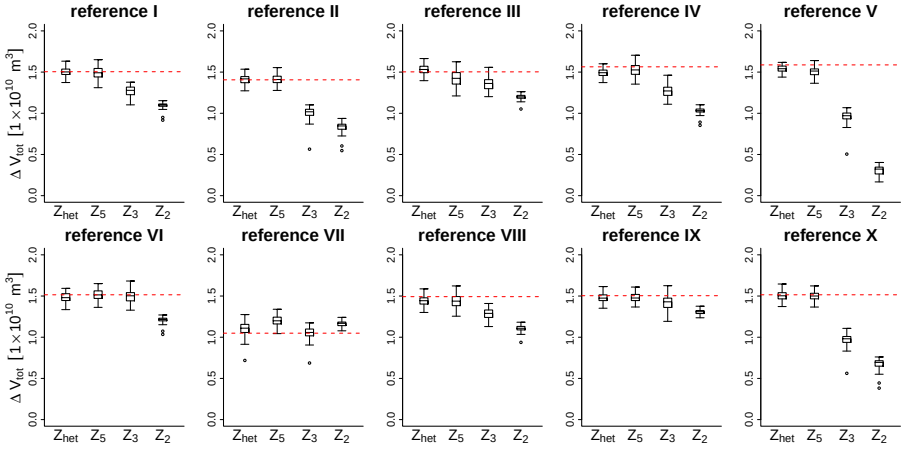

FIGURE 4.13: Total amount of water exchanged between river and aquifer over the whole simulation period (609 days) for conditional simulations with EnKF (scenario C). Red lines mark the water exchange for the different reference runs.

The general worse performance for Z_3 and Z_2 in terms of head and flux predictions is a consequence of the spatial averaging of $\log(L)$. For the ensembles used for scenario C the spatial contrasts for $\log(L)$ are higher due to the predefined zonation in the references and initial ensembles. Therefore, the leakage zones of Z_3 and Z_2 cover parts of the reference fields that have very different $\log(L)$-values. This can be seen in Figure 4.14 where the initial $\log(L)$ ensemble is compared with the updated one at the end of the simulation period. Because Z_3 and Z_2 are not flexible enough to account for the variability of the references due to their limited number of leakage zones the simulated piezometric heads and leakage fluxes deviate more strongly from the reference values than Z_{het} and Z_5.

4.6 Discussion

Simulations with EnKF generally led to an improvement for all four ensembles in terms of $RMSE_h$. It was found that a stochastic field approach (i.e., each discretization point of the model grid has a different leakage value, which results in 457 values in this study) gave the best results. Data assimilation with EnKF made it possible to correct the cumulative fluxes between river and aquifer almost completely. For Z_{het} also the spatial distribution of $\log(L)$ gets quite close to the reference fields during data assimilation and this is also reflected in the spatial distribution of exchange fluxes which closely coincides with those of the reference runs. Data assimilation results in a decrease of the variability of $\log(L)$ especially in regions with high exchange fluxes between river and aquifer. In

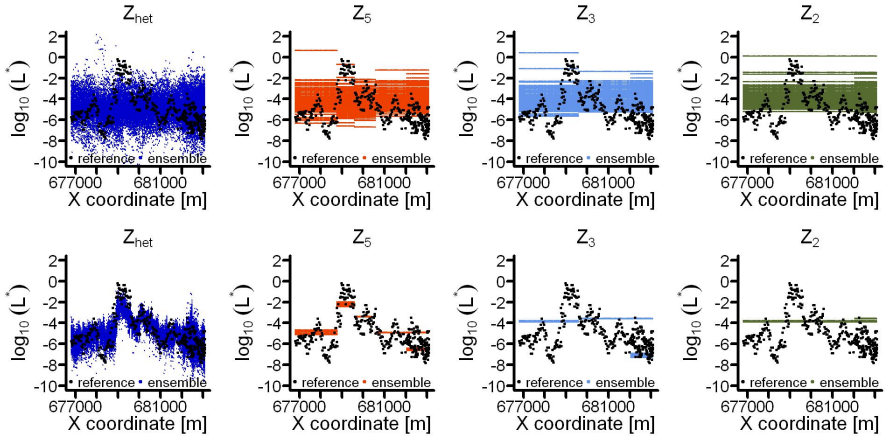

FIGURE 4.14: Ensembles of leakage coefficients (colored) and reference field (black) along x-axis of model domain at day 1 (upper row) and at day 600 (lower row) for scenario C.

other river regions where exchange fluxes are not so high the uncertainty regarding $\log(L)$ was reduced compared to the initial ensemble but not to the same extent as for regions with a higher net flux. The lower adaptation of $\log(L)$ in regions of low exchange fluxes is probably a consequence of the lower sensitivity of the parameter update on head measurements, i.e., for low exchange fluxes the correlation between piezometric heads and $\log(L)$ is low what leads to a lower degree of adaptation for $\log(L)$. The opposite applies for regions with higher fluxes where the adaptation of model parameters is better constrained what leads to a lower variability of model parameters in the end of the simulation period.

For the three zonated ensembles the overall performance was usually slightly worse than for the ensemble with full heterogeneity. Especially the net fluxes showed significant deviations from the true values for Z_3 and Z_2 for several references. This is reflected in the spatial distribution of fluxes along the river where regions with higher fluxes in the reference runs were not adequately represented by the ensembles Z_3 and Z_2. EnKF was only partly able to correct for the systematic errors that arose from the wrong spatial distribution of exchange fluxes and as a result of this the prediction of net fluxes was not as good as for Z_{het}. For Z_5 the predicted net fluxes were often similar to the ones of Z_{het} but the spatial distribution of fluxes was not as good as for Z_{het}. This was also the case when Z_5 closely matched the spatial distribution of $\log(L)$ of the reference runs (scenario C). Even with this prior information only the net fluxes were estimated correctly but not their spatial distribution. This also applies for references with a lower degree of heterogeneity (scenario B). Even in this case the predicted spatial distribution of leakage fluxes was better with Z_{het} than with the different zonation approaches. However, a

precise estimation of high local leakage fluxes is highly relevant for transport calculations in order to determine source regions of contaminants or regions of high biogeochemical turnover. For these applications the usage of effective parameters thus will only lead to averaged concentration levels that are derived from the net exchange between river and aquifer.

For a lower observation density (10 measurement locations) the results were not very different from the ones for 100 observation points. However, for Z_{het} the uncertainty in the $\log(L)$ ensemble was larger than for the case with 100 measurement data. As a result of this also the uncertainty regarding the exchange fluxes was higher. Nevertheless, the error in head and flux predictions was still equal or better than for the zonated ensembles. Generally, a lower information content did not significantly affect the identification of the leakage parameters and the prediction of fluxes and states.

The results from these synthetic studies suggest that the high-resolution characterization of river bed properties is feasible, because even with a limited number of measurements, the high-resolution reconstruction led to better results than an approach where the spatial variability of the river bed was represented with a few effective parameters only. It is expected that in case only very few measurements are available, high-resolution and zonation approaches might give predictions of similar quality, and that in case of more measurements the high-resolution approach will increasingly outperform the approaches where only a few effective parameters are estimated. It can be important to condition multiple equally likely stochastic high-resolution realizations of river bed properties, because the quality of the estimated net exchange fluxes between aquifer and stream are better with this approach than with a zonation approach. Replacing the heterogeneous streambed with few effective parameters results in biased predictions of exchange fluxes. Over long streams such a systematic bias might result in an important under- or overestimation of the groundwater infiltration in the river, as well as an under- or overestimation of the loss of river water to the aquifer under flood conditions. Therefore, the calibration of equally likely stochastic realizations of river bed properties using EnKF together with an augmented state vector approach is recommended for a better characterization of river-aquifer exchange fluxes. This approach is especially needed in case of very heterogeneous streambeds and in case enough conditioning measurements (piezometric head data) are available.

Of course, these findings were derived on the basis of a simplified model which only accounts for uncertainties regarding leakage parameters. In real-world applications uncertainties also arise from the poorly known distribution of aquifer properties, model structural errors and uncertainties in the determination of forcing terms for the model. Thus, the calibration of $\log(L)$-distributions with EnKF in real-world cases will probably

not be as confident as in the presented synthetic simulations due to the higher overall uncertainties. Nevertheless, the principal differences between a heterogeneous ensemble and an ensemble of effective parameters will remain because of the higher flexibility of the heterogeneous approach.

4.7 Conclusions

In this chapter, data assimilation experiments including parameter estimation on the basis of an augmented state-vector approach with EnKF were performed. This approach was used for a synthetic river-groundwater interaction problem to update piezometric heads and river bed properties. In this context, different parametrizations of river bed heterogeneity (full heterogeneity versus different amounts of effective parameters) were tested for its effect on the prediction of groundwater levels and river-aquifer exchange fluxes. Results showed that data assimilation with EnKF in river-aquifer systems benefits from a high spatial resolution of river bed conductivities. When the heterogeneity of the true field of river bed conductivities was represented in the ensemble, EnKF was able to correct the parameter ensemble towards the reference values what led to a correct prediction of the spatial distribution of exchange fluxes. When the river was divided in a relatively limited number of leakage zones (2, 3 or 5) the net exchange between river and aquifer was still predicted accurately for some references but in general the errors increased with a decreasing representation of heterogeneity. Also the spatial distribution of fluxes was less well captured when a zonation was imposed on the river bed conductivities. The observation density mostly affected the prediction for the fully heterogeneous ensemble for which the prediction uncertainty increased when less observations were available for the update with EnKF. However, the errors in head and flux predictions were still lower in this case than for simulations with a zonation of the river bed properties.

In summary, it is concluded that a zonation of river bed conductivities should be avoided because small regions with high exchange fluxes might be averaged out by zonation what affects the local water balance. The simulations performed in this chapter showed that parameter updates with EnKF are able to adapt an ensemble of different fields of river bed conductivity towards the true reference field. Furthermore, the CPU demand for parameter adaptation with EnKF is not dependent on the number of defined leakage zones as opposed to other calibration techniques. Thus, parameter updates with EnKF might be an efficient way to calibrate model parameters for heterogeneous river beds.

Chapter 5

Assimilation of groundwater temperatures*

5.1 Introduction

A special feature of river-aquifer systems is that there can be a distinct cyclic heat exchange between the river and the aquifer. Depending on the climatological conditions, surface water temperatures are subjected to diurnal and seasonal variations whereas groundwater is characterized by relatively constant temperatures. The temperature distribution around streams is therefore governed by the temperature difference and the exchange pattern between river and aquifer. For example, seepage from the river to the aquifer will result in a temperature signal that propagates into the aquifer given a certain temperature difference between both compartments. Vice versa, an aquifer that discharges into the river will also generate a distinct thermal profile within the river bed. This heat exchange between river and aquifer can be deployed to characterize the exchange fluxes as well as relevant material properties of the river bed and the adjacent aquifer (Anderson, 2005; Constantz, 2008). As a tracer, groundwater temperatures are more sensitive to the connectivity patterns within an aquifer and can thus provide additional information on aquifer structure compared to hydraulic data alone. Another feature that makes the utilization of heat as a tracer very attractive is that temperature data can be measured very easily at a low cost.

This technique has for example been used to derive a detailed spatial picture of river-aquifer exchange fluxes under field conditions (e.g., Conant, 2004; Schmidt et al., 2006;

*adapted from: Kurtz, W., Hendricks Franssen, H. J., Kaiser, H.-P., and Vereecken, H. (2013b). Joint assimilation of piezometric heads and groundwater temperatures for improved assessment of river-aquifer interactions. UNDER PREPARATION FOR: *Water Resour. Res.*

Hatch et al., 2010). A common approach for such small scale applications is to measure vertical temperature profiles in the river bed and to apply an analytical solution to the measured temperature profiles to infer the exchange fluxes between river and aquifer (Schornberg et al., 2010). In most cases, only a limited number of point measurements of temperatures are available for the estimation of exchange fluxes. Recently, also temperature measurements with fibre-optic sensors, also called Distributed Temperature Sensing (DTS), has gained interest for the derivation of spatially highly resolved temperature distributions (Vogt et al., 2012).

Thermal data have also been used as an additional information source for different inversion techniques to constrain the estimation of subsurface parameters. For example, Woodbury and Smith (1988) investigated the worth of thermal data for the calibration of steady-state groundwater models. They argue that thermal data can better constrain the calibration of hydraulic conductivities especially for highly permeable aquifers when heat advection is the dominant process. Doussan et al. (1994) calibrated a managed river-aquifer system which included bank filtration with hydraulic and thermal data and found an improved estimation of river bed parameters compared to hydraulic data alone. Bravo et al. (2002) also used hydraulic and thermal data for the inversion of a wetland-aquifer system to derive hydraulic conductivities and wetland inflows. They showed that the inversion gets more stable and accurate when thermal data are used compared to hydraulic data alone. In Jiang and Woodbury (2006), a Bayesian inversion technique was applied to an aquifer model which was conditioned on different combinations of piezometric heads, transmissivities and temperature measurements. They found that the characterization of hydraulic conductivities was improved with temperature data for different inversion scenarios.

For modeling purposes, an important implication of the temperature contrast between rivers and aquifers and the resulting heat transfer is that these temperature changes in the sediment induce a cyclic variation of water density and viscosity which also affects the hydraulic conductivity of the river bed sediments (see Equations 3.11 and 3.12). Changes in water density can usually be neglected for the temperature range that occurs in river-aquifer systems but water viscosity could change up to a factor of 1.7 given a typical temperature range between 5 and 25 °C . For example, Constantz et al. (1994) argue that their measured diurnal variation of river-aquifer exchange fluxes is largely attributed to the temperature-dependency of hydraulic properties of the streambed. Engeler et al. (2011) have shown that considering the temperature dependency of water viscosity in the simulation of river-aquifer exchange can reduce the predictions errors of piezometric heads at individual measurement locations up to 30 %. Ma and Zheng (2010) investigated the effect of regarding temperature-dependent hydraulic parameters for the modeling of heat transport in river-aquifer systems. They concluded that temperature

contrasts up to 15 °C lead to an average error in temperature predictions of about 3% calculated over their whole model domain. However, they did not compare the effects on individual measurement locations.

Apart from river-aquifer systems, heat transfer calculations can also be relevant to other systems of surface water-groundwater exchange. One example is artificial recharge because for such systems also a temperature contrast between surface water and groundwater is given. Vandenbohede and Van Houtte (2012) give an example of such an application were heat transport calculations were made for an artificial recharge system to characterize the transport behavior underneath a recharge basin. Racz et al. (2012) used measured temperature profiles underneath an artificial recharge basin to determine local infiltration fluxes.

An excellent example of a managed groundwater system that includes the effects of river-aquifer exchange and artificial recharge is the Limmat aquifer in Zurich (Switzerland). For the groundwater management at this site, water is pumped from several bank filtration wells close to the river Limmat and this water is then artificially recharged to the aquifer through several recharge basins and wells. This measure is taken to protect drinking water wells from a diffuse contamination that is present close to the well field. These management activities heavily influence the hydraulic and thermal situation in this aquifer. Recently, a real-time modeling system was set up for the management of this site (Hendricks Franssen et al., 2011). In this framework, the Ensemble Kalman Filter (EnKF) is applied to correct the piezometric head predictions and the hydraulic parameters of a 3D groundwater model for this site with data from a dense online-monitoring network for groundwater levels on a daily basis. The updated predictions of this model can then be used to optimize the operation of the well field through a real-time control system (Bauser et al., 2010). In 2005, the monitoring network was additionally equipped with several online-sensors for groundwater temperature which allow a continuous monitoring of the thermal situation within the well field. As already pointed out before, groundwater temperatures are well suited as a tracer for exchange processes between surface water and groundwater which also have a large influence on the operation of the well field in the Limmat aquifer. Thus, the additional online-monitoring of groundwater temperatures can provide important information on the subsurface structure for this site which is until now not utilized in the EnKF data assimilation framework. Another aspect concerning the operation of the well field and the temperature distribution in the aquifer is that groundwater managers usually want to avoid the pumping of drinking water that is too warm because this can negatively influence drinking water quality through bacterial contamination and increases the effort for disinfection measures. As a consequence, also predictions of groundwater temperatures are desired for this well field

and groundwater managers also plan to include measured groundwater temperatures in the real-time control of the well field.

The aim of the following study is to extend the existing EnKF data assimilation framework for the Limmat aquifer, so that also temperature measurements can be used to update the predictions of groundwater states and model parameters. The joint assimilation of piezometric head and temperature data will first be tested with a synthetic river-aquifer model in order to access the worth of the additional temperature assimilation on the estimation of hydraulic parameters under controlled conditions. Afterwards, the extended data assimilation framework will also be applied to the real-world data of the Limmat aquifer and it will be explored how the assimilation of measured groundwater temperatures affects the prediction of heat transport in the model and also how the joint assimilation of hydraulic and thermal data influences the estimation of hydraulic parameters under real-world conditions.

5.2 Materials and Methods

5.2.1 Joint assimilation of piezometric head and temperature data

For the joint assimilation of piezometric heads and groundwater temperatures the data assimilation scheme described in Sections 2.2 and 3.2 was extended so that also measurements of groundwater temperatures are used in the assimilation process. The model states $\boldsymbol{\psi}$ are piezometric heads $\boldsymbol{h}$ and groundwater temperatures $\boldsymbol{T}$ and the relevant parameters $\boldsymbol{\phi}$ for the system under investigation are hydraulic conductivities $\boldsymbol{K}$ and leakage coefficients $\boldsymbol{L}$:

$$\boldsymbol{\psi} = \begin{pmatrix} \boldsymbol{h} \\ \boldsymbol{T} \end{pmatrix} \tag{5.1}$$

$$\boldsymbol{\phi} = \begin{pmatrix} \log(\boldsymbol{K}) \\ \log(\boldsymbol{L}) \end{pmatrix} \tag{5.2}$$

The model $M(\boldsymbol{\psi}_i^{t-1}, \boldsymbol{\phi}_i, \boldsymbol{\zeta}_i)$ that describes the forward propagation of the model states ($\boldsymbol{h}$ and $\boldsymbol{T}$) for each realization i of model parameters ($\boldsymbol{K}$ and $\boldsymbol{L}$) is a groundwater model that solves the coupled equations for variably saturated flow (Equations 2.2 to 2.6b), heat transport (Equations 2.7 to 2.10c) and river-aquifer exchange (Equation 2.11).

The state-parameter vector in the updating scheme of EnKF is given as:

$$\boldsymbol{\Psi} = \begin{pmatrix} \boldsymbol{h} \\ \boldsymbol{T} \\ \log(\boldsymbol{K}) \\ \log(\boldsymbol{L}) \end{pmatrix} \tag{5.3}$$

For the update of $\boldsymbol{\Psi}$ measurement data of piezometric heads $\boldsymbol{y}^h$ and groundwater temperatures $\boldsymbol{y}^T$ are used which are combined in the measurement vector $\boldsymbol{y}^0$:

$$\boldsymbol{y}^0 = \begin{pmatrix} \boldsymbol{y}^h \\ \boldsymbol{y}^T \end{pmatrix} \tag{5.4}$$

For the assimilation of these measurement data with EnKF, $\boldsymbol{y}^0$ is perturbed with the expected measurement errors of $\boldsymbol{h}$ and $\boldsymbol{T}$ ($\epsilon(\boldsymbol{h})$ and $\epsilon(\boldsymbol{T})$). For each realization i a separate perturbation vector $\tilde{\boldsymbol{\epsilon}}$ for $\boldsymbol{y}^0$ is drawn from a normal distribution $\mathcal{N}(0, \epsilon)$ with a mean of zero and a variance that is derived from the expected measurement errors $\epsilon(\boldsymbol{h})$ and $\epsilon(\boldsymbol{T})$. This yields a separate perturbed measurement vector $\tilde{\boldsymbol{y}}$ for each realization:

$$\tilde{\boldsymbol{y}}_i = \begin{pmatrix} \boldsymbol{y}^h \\ \boldsymbol{y}^T \end{pmatrix} + \begin{pmatrix} \tilde{\boldsymbol{\epsilon}}_i(\boldsymbol{h}) \\ \tilde{\boldsymbol{\epsilon}}_i(\boldsymbol{T}) \end{pmatrix} \tag{5.5}$$

The updating equation for the joint assimilation of piezometric heads and groundwater temperatures and the derivation of the Kalman gain are the same as in Sections 2.2 and 3.2 and are repeated here for convenience:

$$\boldsymbol{\Psi}_i^a = \boldsymbol{\Psi}_i^t + \alpha \mathbf{G}(\tilde{\boldsymbol{y}}_i - \mathbf{H}\boldsymbol{\Psi}_i^t) \tag{5.6}$$

$$\mathbf{G} = \mathbf{C}\mathbf{H}^\top(\mathbf{H}\mathbf{C}\mathbf{H}^\top + \mathbf{R})^{-1} \tag{5.7}$$

where $\boldsymbol{\Psi}_i^t$ and $\boldsymbol{\Psi}_i^a$ are the forecasted and updated state-parameter vectors (see Equation 5.3), $\tilde{\boldsymbol{y}}_i$ is the perturbed measurement vector of piezometric heads and groundwater temperatures (see Equation 5.5), $\mathbf{G}$ is the Kalman gain, $\mathbf{H}$ is a matrix that maps/ interpolates the simulated states to the observation points, $\mathbf{C}$ is the covariance matrix of the model states and uncertain model parameters, $\mathbf{R}$ is the covariance matrix of measurement errors and α is a damping factor for the parameter update that takes values between 0 and 1 and is used to reduce the effect of filter inbreeding (Hendricks Franssen and Kinzelbach, 2008).

The following covariance matrix is used in the calculation of the Kalman gain for the joint update of $\boldsymbol{h}$, $\boldsymbol{T}$ and the parameters:

$$\mathbf{CH}^{\top} = \begin{pmatrix} \mathbf{C}_{\boldsymbol{h}\hat{\boldsymbol{h}}} & \mathbf{C}_{\boldsymbol{T}\hat{\boldsymbol{T}}} \\ \mathbf{C}_{\log(\boldsymbol{K})\hat{\boldsymbol{h}}} & \mathbf{C}_{\log(\boldsymbol{K})\hat{\boldsymbol{T}}} \\ \mathbf{C}_{\log(\boldsymbol{L})\hat{\boldsymbol{h}}} & \mathbf{C}_{\log(\boldsymbol{L})\hat{\boldsymbol{T}}} \end{pmatrix} \tag{5.8}$$

where $\hat{\boldsymbol{h}}$ are the simulated piezometric heads at observation points and $\hat{\boldsymbol{T}}$ are the simulated groundwater temperatures at observation points. Note that the cross-covariances between $\boldsymbol{h}$ and $\boldsymbol{T}$ are neglected in this assimilation scheme, i.e., neither $\boldsymbol{h}$ is used to update $\boldsymbol{T}$ nor $\boldsymbol{T}$ is used to update $\boldsymbol{h}$.

5.2.2 Parallelization of the assimilation code EnKF3d-SPRING

The program EnKF3d-SPRING was already applied in Chapters 3 and 4 for the conduction of the data assimilation experiments. EnKF3d-SPRING is a C program that manages the forward calculations of the ensemble and calculates the EnKF updating step for each assimilation cycle. The actual solution of the flow and transport equations is calculated by the groundwater modeling software SPRING (Delta h Ingenieurgesellschaft mbH, 2006) which is called from within EnKF3d-SPRING as a library function for each realization and time step. In order to perform the joint assimilation of hydraulic and thermal data, the data assimilation scheme implemented in EnKF3d-SPRING was extended with the updating equations given above. However, as the computational burden for the calculation of a large number of realizations with a coupled flow and heat transport model is tremendously higher than the calculation of pure groundwater flow, it was necessary to parallelize EnKF3d-SPRING in order to retrieve results in an acceptable computation time. Principally, the parallelization of data assimilation codes can be performed at three levels:

I parallelizing the call of the forward runs

II parallelizing the forward model

III parallelizing the updating step.

As there was no parallel version available for the forward model, only parallelization at the levels I and III could be implemented in EnKF3d-SPRING. Low-order performance tests on the supercomputing platform JUROPA at Forschungszentrum Jülich showed that the parallel version of EnKF3d-SPRING scales well up to 128 processors with an

efficiency of about 70%. More recent changes and optimizations in the code probably increased the efficiency and scalability of the code but further performance tests were not conducted for this version of the program.

5.2.3 Localization

For some of the simulations the effect of distance-dependent localization (Hamill et al., 2001) was tested in the EnKF updating scheme. The rationale behind localization is to restrict the influence of observation points in space because each observation point only has a certain area of influence around itself (which is defined by the length scale variable η). Model variables beyond this area are then not updated with measurements from this observation point. For this purpose, the Schur product (i.e., an element wise multiplication of two matrices) of the covariance matrix $\mathbf{CH}^\top$ and a localization matrix $\mathbf{\Omega}$ is calculated at each assimilation cycle and the so derived localized covariance matrix is then used in the calculation of the Kalman gain:

$$\left(\mathbf{CH}^\top\right)_{ij}^{\text{new}} = (\mathbf{CH}^\top)_{ij} \cdot (\mathbf{\Omega})_{ij} \tag{5.9}$$

where i and j are the matrix indices. The elements of $\mathbf{\Omega}$ were calculated with the following localization function $\gamma(d, \eta)$ (Equation 5.10) (Hamill et al., 2001; Gaspari and Cohn, 1999):

$$\gamma(d,\eta) = \begin{cases} 1 - \frac{1}{4}\left(\frac{2d}{\eta}\right)^5 + \frac{1}{2}\left(\frac{2d}{\eta}\right)^4 + \frac{5}{8}\left(\frac{2d}{\eta}\right)^3 - \frac{5}{3}\left(\frac{2d}{\eta}\right)^2 & 0 \le d \le \eta/2 \\ \frac{1}{12}\left(\frac{2d}{\eta}\right)^5 - \frac{1}{2}\left(\frac{2d}{\eta}\right)^4 + \frac{5}{8}\left(\frac{2d}{\eta}\right)^3 + \frac{5}{3}\left(\frac{2d}{\eta}\right)^2 - 5\left(\frac{2d}{\eta}\right) + 4 - \frac{2}{3}\left(\frac{2d}{\eta}\right)^{-1} & \eta/2 < d \le \eta \\ 0 & d > \eta \end{cases} \tag{5.10}$$

where d is the euclidean distance between the locations of observation points and of the elements of the state-parameter vector $\mathbf{\Psi}$ [L] and η is a certain length scale which has to be defined for the problem [L]. Figure 5.1 illustrates the shape of γ for a length scale η of 500 meters.

This function has a shape similar to a Gaussian bell curve with the major difference that values beyond a fixed value (η) for this function are zero whereas values for a Gaussian distribution are always greater than zero.

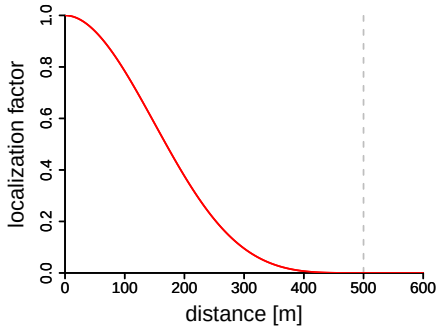

FIGURE 5.1: Localization function $\gamma(d, \eta)$ for a length scale η of 500 m.

5.2.4 Synthetic aquifer model

Assimilation experiments were first performed with a simplified synthetic model of a river-aquifer system. A sketch of the model setup is given in Figure 5.2. The model has a dimension of $500 \times 250 \times 10$ m and is discretized into $50 \times 25 \times 10$ cells. A river was placed in the middle of the model domain and was represented through two rows of leakage nodes. Three extraction wells were placed south of the river and a regular grid of observation wells was lain out over the whole model domain. Hydraulic forcing data for the model are transient discharge of the river (expressed as river stages), transient pumping rates for the three wells and a constant small lateral inflow/ outflow at the eastern /western face of the model (assigned to the three lowest layers). Thermal forcing data are transient river temperatures.

The entire input data were based on real-world measurements for the Limmat aquifer. River stages were calculated from measured discharge data of river Sihl for the year 2006 assuming simple open channel flow. Pumping rates were taken from three bank filtration wells of the Limmat aquifer but withdrawal rates were halved in order to achieve a reasonable mass balance for the small synthetic model. River temperatures were taken from measurements of the river Sihl in 2006. A summary of the forcing data for the synthetic model is given in Figure 5.3.

For the synthetic experiments a reference run with a specific K and L field was integrated for a one year period with the model described above. h and T data sampled from this reference run (at the observation points) were then taken as input data for assimilation experiments with EnKF.

The reference $\log(K)$ field was generated with Sequential Gaussian Simulation (SGS) with a mean of -2 $\log(\mathrm{ms}^{-1})$, a range of 100 m and a sill of 0.5 $\log(\mathrm{m}^2\mathrm{s}^{-2})$. The initial ensemble of K values was created in a similar way but with a mean value of -1 instead of

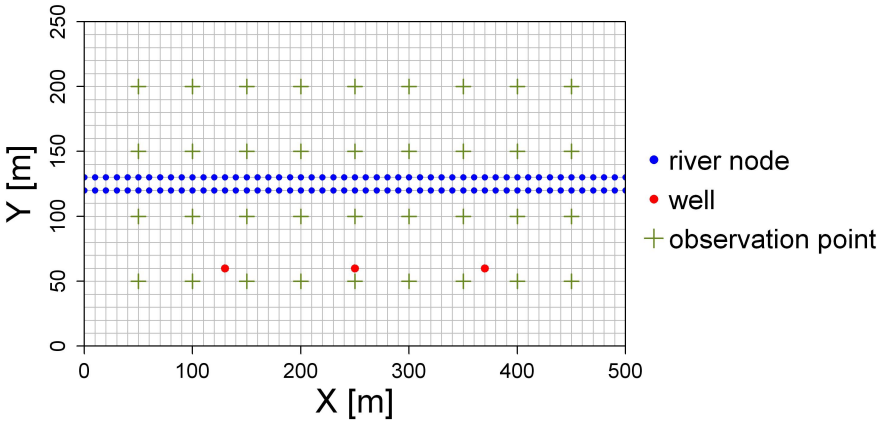

FIGURE 5.2: Model setup for synthetic experiments.

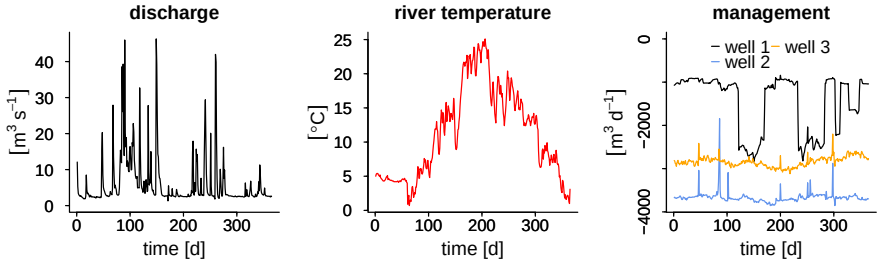

FIGURE 5.3: Forcing data for synthetic experiments.

-2 log(ms^{-1}) (range and sill were the same as for the creation of the reference field). The reference field for leakage coefficients L was created by reducing the K values underneath the river by one log unit and dividing this value by the discharge area of the respective leakage node. The initial ensemble of L was created in a similar way by taking the initial K values underneath the river, multiplying them with 0.5 and also dividing them by the discharge area of the respective leakage node. Note that K and L fields for reference and initial ensemble are slightly biased for this setup. Table 5.1 gives an overview of the settings used for heat transport simulations and for the data assimilation with EnKF. Table 5.2 summarizes the different updating scenarios for the synthetic case.

5.2.5 Model and input data for real-world case

Simulations for the real-world case were performed with the same 3D-model of the Limmat aquifer that was already used in Chapters 3 and 4. Again, transient boundary conditions of the flow model include recharge flux at the top of the model domain, small

TABLE 5.1: Parameters for heat transport simulations and for data assimilation with EnKF for synthetic experiments.

	parameter	value	unit
Parameters for heat transport calculations	δ	25	m
	ρ_s	2600	$\mathrm{kgm^{-3}}$
	ρ_w	1000	$\mathrm{kgm^{-3}}$
	κ_s	3.5	$\mathrm{Js^{-1}m^{-1}K^{-1}}$
	κ_w	0.587	$\mathrm{Js^{-1}m^{-1}K^{-1}}$
	c_s	800	$\mathrm{Jkg^{-1}K^{-1}}$
	c_w	4192	$\mathrm{Jkg^{-1}K^{-1}}$
Settings for EnKF	$\mathrm{N_{real}}$	128	
	$\mathrm{N_{obs}}(\boldsymbol{h})$	36	
	$\mathrm{N_{obs}}(\boldsymbol{T})$	36	
	α	0.1	
	update frequency	10	d
	$\epsilon(\boldsymbol{h})$	0.05	m
	$\epsilon(\boldsymbol{T})$	0.1	K

TABLE 5.2: Simulation scenarios for synthetic case. Multiple column entries indicate that the scenario was simulated with varying values for this variable.

scenario name	update of:				$\mathrm{N_{obs}}(\boldsymbol{h})$	$\mathrm{N_{obs}}(\boldsymbol{T})$	η
	h	T	K	L			[m]
$\mathrm{SY_{uc}}$					0	0	-
$\mathrm{SY_{hT}}$	√	√			36	36	-
$\mathrm{SY_{hKL}}$	√		√	√	36	36	-
$\mathrm{SY_{TKL}}$		√	√	√	36	36	-
$\mathrm{SY_{hTKL}}$	√	√	√	√	36	36	-/100/200/350/500

lateral inflows from surrounding hills on the south and north face of the model, fixed head boundary conditions on the western face, river stages of the rivers Limmat and Sihl as well as infiltration and withdrawal rates of the management wells. Details on the calculation of transient boundary conditions for the flow model can be found in Hendricks Franssen et al. (2011). Transient boundary conditions for the heat transport simulations include river temperatures, the temperature of injected water in infiltration wells/ recharge basins and the temperature of the first model layer which is set equal to the 20 cm soil temperature measured at the meteorological station Reckenholz (MeteoSwiss).

Simulations were performed with 128 different realizations of hydraulic conductivity fields and leakage coefficients. The initial ensemble of hydraulic conductivities was generated on the basis of a pre-calibration of the flow model with 87 piezometric head data for the time periods June 2004 and July 2005 with the pilot point method with a regularization terms (Alcolea et al., 2006). The ensemble of K was generated by perturbing the calibrated $\log(K)$-field with perturbation fields that were generated by

TABLE 5.3: Parameters for heat transport calculations and data assimilation with EnKF for real-world case.

	parameter	value	unit
Parameters for heat transport calculations	δ	25	m
	ρ_s	2600	$\mathrm{kgm^{-3}}$
	ρ_w	1000	$\mathrm{kgm^{-3}}$
	κ_s	3.5	$\mathrm{Js^{-1}m^{-1}K^{-1}}$
	κ_w	0.587	$\mathrm{Js^{-1}m^{-1}K^{-1}}$
	c_s	800	$\mathrm{Jkg^{-1}K^{-1}}$
	c_w	4192	$\mathrm{Jkg^{-1}K^{-1}}$
Settings for EnKF	$\mathrm{N_{real}}$	128	
	$\mathrm{N_{obs}}(\boldsymbol{h})$	87	
	$\mathrm{N_{obs}}(\boldsymbol{T})$	22	
	α	0.1	
	update frequency	10	d
	$\epsilon(\boldsymbol{h})$	0.05	m
	$\epsilon(\boldsymbol{T})$	0.1	K

SGS (Gómez-Hernández and Journel, 1993) on a very fine grid which was then upscaled to the simulation grid through simplified renormalization (Renard et al., 2000). The geostatistical parameters for the creation of these perturbation fields were estimated from about 857 small scale $\log(K)$ measurements that were conducted for this area (see Hendricks Franssen et al., 2011). The ensemble of leakage coefficients was generated in a similar way as the $\mathrm{Z_{het}}$ ensemble in Chapter 4, i.e., the $\log(L)$-values were spatially distributed along the river reach. Geostatistical parameters for the generation of these $\log(L)$-fields were a range sampled from a uniform distribution between 50 and 5000 m and a sill sampled from a uniform distribution between 0.1 and 2 $\log(\mathrm{m^2 s^{-2}})$.

Within the model area 87 observation points for piezometric heads and 22 observation points for groundwater temperatures are available. The spatial position of these observation points is shown in Figure 5.4. Hydraulic head observations are distributed over the whole model domain with the highest density in the Hardhof area where most of the management activities take place. The observation points for groundwater temperatures are only clusters in the Hardhof area mostly between the recharge basins and the river in different depths.

Data assimilation experiments were conducted for different settings of EnKF which include the update of states only, the joint update of states and parameters and the use of localization. Tables 5.3 and 5.4 give an overview of the standard settings for EnKF, heat transport calculations and the performed simulation scenarios.

Online-sensors for measuring groundwater temperature were available since autumn 2005. Therefore, heat transport simulation were performed with data ranging from

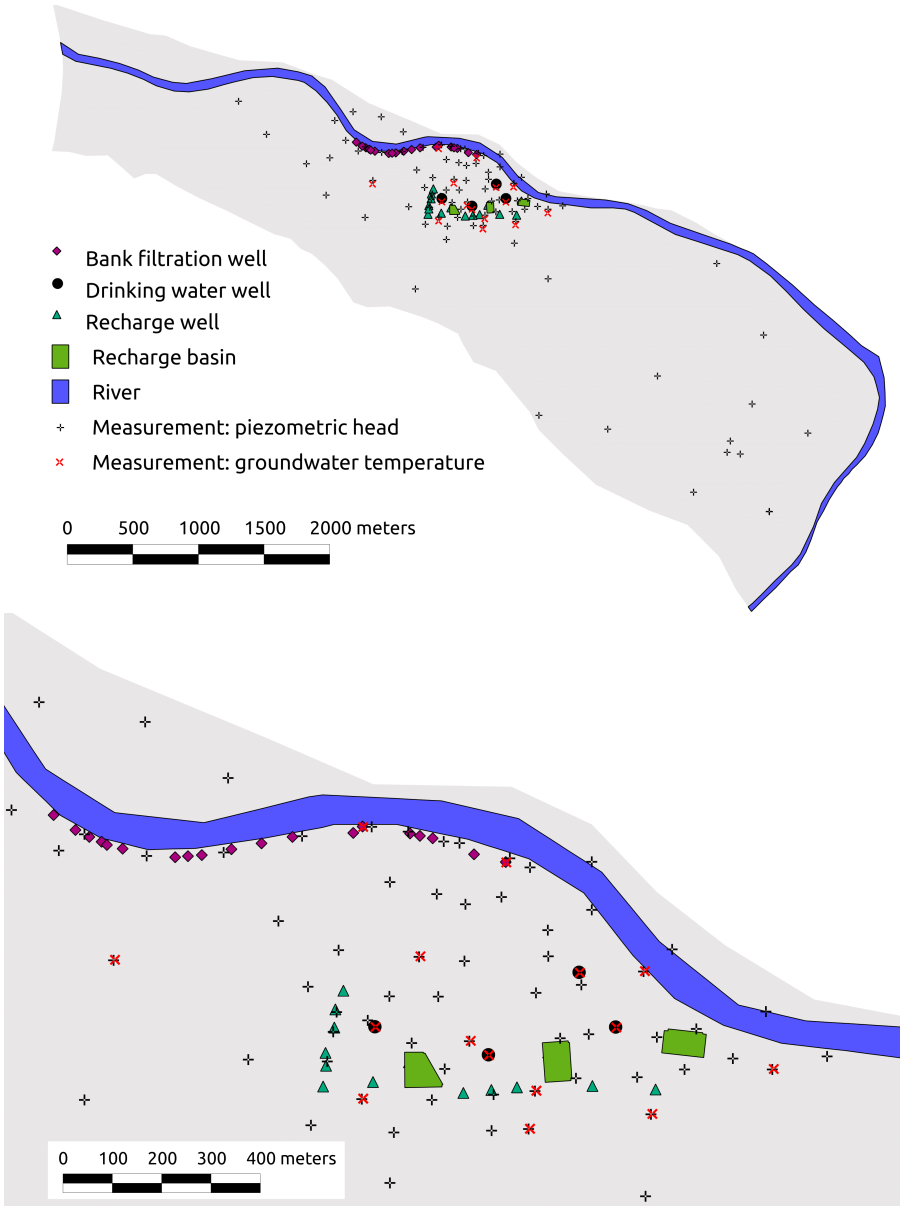

FIGURE 5.4: Position of observation points for piezometric heads and groundwater temperatures. The upper plot shows the distribution of observation points over the whole Limmat aquifer model and the lower plot illustrates the distribution of observation points in the Hardhof area.

TABLE 5.4: Simulation scenarios for real-world case. Multiple column entries indicate that the scenario was simulated with varying values for this variable.

scenario	update of:				$N_{obs}(\boldsymbol{h})$	$N_{obs}(\boldsymbol{T})$	η	$\epsilon(\boldsymbol{h})$	$\epsilon(\boldsymbol{T})$
	h	T	K	L			[m]	[m]	[°C]
RW_{uc}					0	0	-	0.05	0.1
RW_{hT}	√	√			87/40	22/11	-/2000	0.05	0.1
RW_{hKL}	√		√	√	87	22	-	0.05	0.1
RW_{hTKL}	√	√	√	√	87/40	22/11	-/2000/ 3000	0.05/0.25/ 0.5	0.1/0.5/ 1.0

2006 to 2012. Four simulation periods have to be distinguished: The year 2006 was used as a warm-up period for the model in order to have a more realistic estimate of the temperature distribution within the aquifer. This spinup was conducted with the initial parameter ensembles of K and L without data assimilation. The initial h- and T-fields were generated with steady state calculations of the average parameter fields where the initial groundwater temperature were set to 13 °C for the entire aquifer which is roughly the mean groundwater temperature measured further away from the rivers. The final h- and T-fields from this warm-up period for each ensemble member were then used as initial conditions for the different assimilation experiments that were conducted for the year 2007. The updated parameter ensembles for this assimilation period were then used in a subsequent validation period to additionally access the performance of the different assimilation experiments. From January 2008 to October 2010 some major reconstructions were performed in the Hardhof area. These activities included the utilization of additional pumping wells and non-standard management activities. Therefore, this time period was excluded for further heat transport simulations and the validation simulations were done for the hydrological year 2011 (November 2010 - October 2011). The initial conditions for this validation period were estimated by a second spinup of the model that lasted from January 2010 to October 2010. This additional spinup was performed with the initial parameter ensembles (which were also used for the spinup period 2006) and with the final h- and T-fields of unconditional simulations for the assimilation period. The ensemble averages of h and T at the end of this second warm-up period were then used as initial conditions for the validation period. Table 5.5 summarizes the different time periods for the heat transport calculations and Figures 5.5 and 5.6 give an overview on the forcing data that were used for the initial spinup, the assimilation period and the verification period.

TABLE 5.5: Time periods for heat transport simulations.

	period	purpose	initial h/ T	initial K/ L
(I)	01.01.2006 - 31.12.2006	initial spinup	steady state	initial ensemble
(II)	01.01.2007 - 31.12.2007	assimilation period	from unconditional simulation (I)	initial ensemble
(III)	01.01.2010 - 31.10.2010	spinup for verification period	from unconditional simulations (II)	initial ensemble
(IV)	01.11.2010 - 31.10.2011	verification period	mean fields of (III)	updated ensembles from (II)

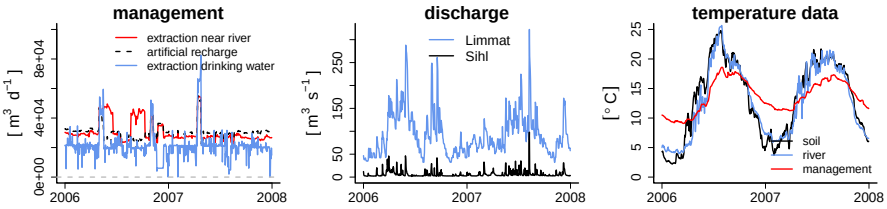

FIGURE 5.5: Forcing data of the model for the years 2006 and 2007 (initial model spinup and assimilation period).

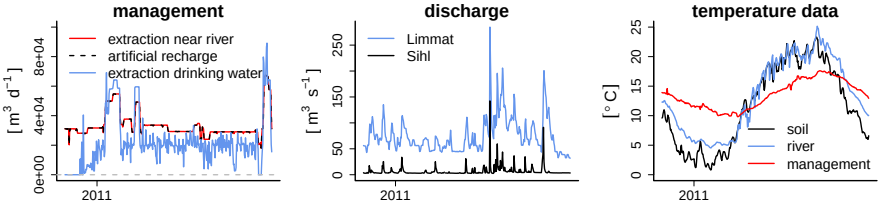

FIGURE 5.6: Forcing data of the model for the hydrological year 2011 (verification period).

5.3 Results

5.3.1 Synthetic experiments

The different updating scenarios of Table 5.2 are first compared with respect to the deviation of state variables from the reference values. Figure 5.7 shows the Root Mean Square Error (RMSE) of piezometric heads and groundwater temperatures for the different scenarios. If only states are updated, there is only a minor improvement compared to unconditional simulations. This is related to the bias in the parameter values of the initial K and L ensembles. When piezometric heads are jointly updated with parameters (scenarios SY_{hKL} and SY_{hTKL}) errors are significantly reduced. For these scenarios

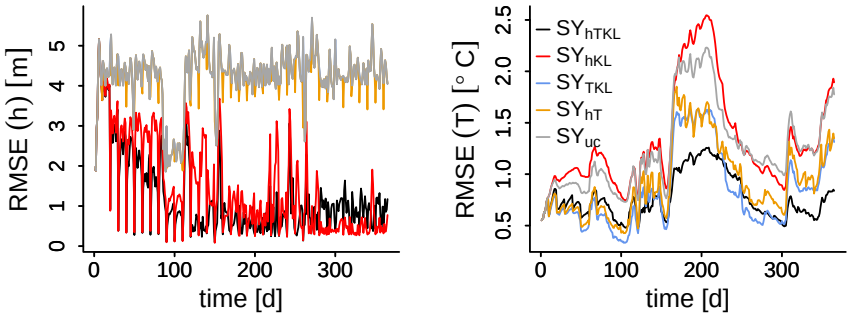

FIGURE 5.7: Root mean square error of piezometric heads (left) and groundwater temperatures (right) for scenarios in Table 5.2.

the joint update of piezometric heads and groundwater temperatures did not lead to a further improvement in the prediction of h.

RMSE(T) shows a seasonal variation for all scenarios as opposed to RMSE(h). The highest values for RMSE(T) are observable during the summer months where the higher temperatures of the river propagate into the aquifer. The temperature contrast between river water and groundwater then leads to the higher deviations between reference and ensemble prediction. The lowest deviation to the reference for T is found for scenario $\mathrm{SY_{hTKL}}$ where all states and uncertain parameters are jointly updated. RMSE(T) for scenarios $\mathrm{SY_{hT}}$ and $\mathrm{SY_{TKL}}$ were very similar and both lower than for the unconditional simulation. This similarity suggests that the parameter update in scenario $\mathrm{SY_{TKL}}$ did not have a significant influence on the prediction of T. For the scenario without an update of T (scenario $\mathrm{SY_{hKL}}$) temperature predictions are similar to unconditional simulation and partly also show a higher RMSE(T). Thus, a parameter update which is only based on hydraulic data can in fact lead to a worse prediction of transport processes.

Figure 5.8 exemplifies the spatial distribution of mean groundwater temperatures for the different scenarios for time step 200. Compared to the reference field the temperature distributions of scenarios $\mathrm{SY_{hT}}$, $\mathrm{SY_{TKL}}$ and the unconditional simulation show a very dispersed heat plume moving from the river into the aquifer whereas the temperature distribution of the reference shows a relatively distinct spatial pattern. In contrast, for scenarios $\mathrm{SY_{hKL}}$ and $\mathrm{SY_{hTKL}}$ the mean temperature field is much closer to the reference field and the dispersion of the heat plume is less pronounced. The dispersion for the scenarios without a parameter update ($\mathrm{SY_{uc}}$, $\mathrm{SY_{hT}}$ and $\mathrm{SY_{TKL}}$) is related to the high uncertainty within the governing parameter fields of K and L. When h data are used to condition the parameter fields the variability in the parameter fields decreases and also the ensemble mean values for the parameter fields are closer to the reference.

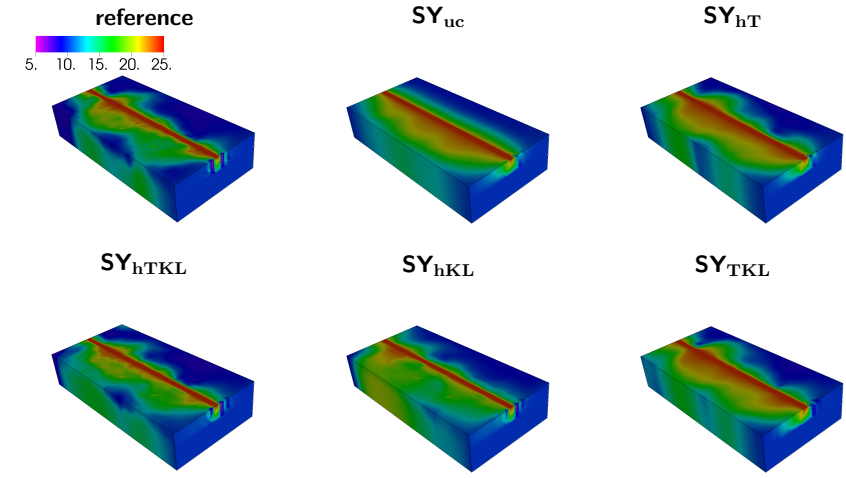

FIGURE 5.8: Average T fields at time step 200 for updating scenarios in Table 5.2.

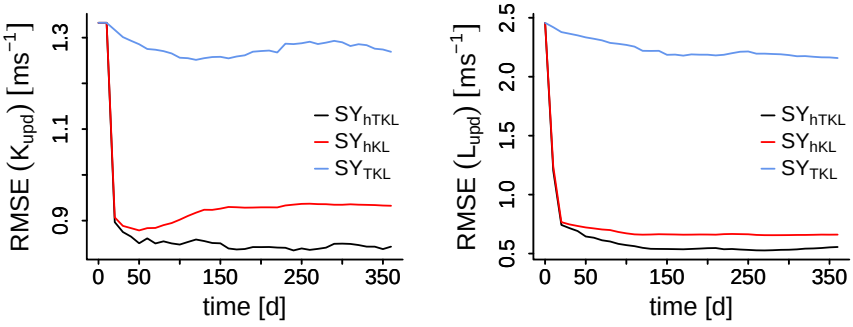

FIGURE 5.9: Root mean square error for updated hydraulic conductivities (left) and updated leakage coefficients (right) for scenarios SY_{hKL}, SY_{hTKL} and SY_{TKL} (Table 5.2).

This can be seen in Figure 5.9 which shows RMSE of K and L for scenarios SY_{hKL}, SY_{hTKL} and SY_{TKL}. When piezometric head data are used to update parameters there is a fast decrease of RMSE within the first assimilation cycles. This decrease is mainly caused by a correction of the bias between the reference fields and the initial ensembles. When only temperature data are used to condition the parameter fields (scenario SY_{TKL}) there is almost no correction of parameter values which explains the similarity between scenario SY_{hT} and SY_{TKL} in terms of temperature distribution and RMSE(T). From Figure 5.9 it can also be seen that the joint assimilation of h and T gives slightly better parameter estimates for K and L than for the scenario where only h data are used.

Figure 5.10 compares the final ensemble means of K for scenarios SY_{hKL}, SY_{hTKL} and

SY_{TKL} with the reference field. For scenario SY_{TKL} there are only minor updates compared to the initial ensemble which do not correspond very well with the distribution of K in the reference field which is the reason for the high RMSE values for this scenario. This means that temperature data alone seem not to be very sensitive on the distribution of K values for this synthetic model setup. When piezometric head data are assimilated with EnKF (scenarios SY_{hKL} and SY_{hTKL}) the structure of the K ensembles is much closer to the reference field. K values are mainly updated along the river reach. So the highest sensitivity of the model seems to be related to river stage fluctuations. Scenario SY_{hKL} tends to assign lower K values along the river reach than scenario SY_{hTKL} which is probably the main reason for the slightly higher RMSE values for scenario SY_{hKL}. The different magnitude of K values along the river reach for scenarios SY_{hKL} and SY_{hTKL} is probably related to their different updating behavior with respect to L (Figure 5.11). Here it can be seen that the uncertainty in the final L ensemble is higher for SY_{hKL} than for SY_{hTKL}, i.e., with assimilation of h data alone the distribution of L could not be constrained as well as with a joint assimilation of h and T. As a result also the residuals for K were higher for scenario SY_{hKL} compared to SY_{hTKL}. From Figure 5.11 it also becomes obvious that the assimilation of h mostly led to a correction of the bias between the initial L ensemble and the reference values whereas an assimilation of temperature data (scenarios SY_{TKL} and SY_{hTKL}) led to a more precise determination of the spatial structure of leakage coefficients. The main advantage of using a joint assimilation of h and T for the synthetic experiments is that both state variables have a different information content which allows a better estimation of leakage parameters. h data provide information on the net exchange between river and groundwater and thus are sensitive to the bias between initial ensemble and the reference values. T data give additional information on the spatial location of exchange fluxes and therefore constrain the spatial structure of leakage parameters.

In addition to the comparison of different updating strategies, the effect of localization on parameter updates was tested with several simulation runs. For this purpose, scenario SY_{hTKL} was rerun with different η values of the localization function (Equation 5.10) ranging from 100 m to 500 m (note that the range parameter for the initial ensemble was 100 m). RMSE of temperature predictions and K values for these simulation runs are shown in Figure 5.12. The simulation with a localization limit of 100 m consistently performed worse compared to the simulation without any localization. In this case the region of influences for the observations is too restricted and only the model cells adjacent to the grid cell of observation points are updated at all. When the localization limit is increased there is no observable effect on simulated groundwater temperatures but the estimation of K values is improved compared to the simulation without localization. It also can be seen from Figure 5.12 that the estimation of K gets slightly worse again

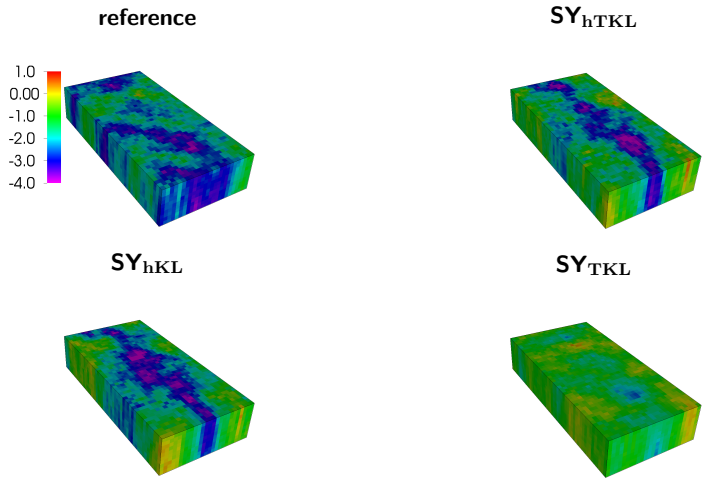

FIGURE 5.10: Updated fields of hydraulic conductivities (end of simulation period) for scenarios SY_{hKL}, SY_{hTKL} and SY_{TKL} (Table 5.2).

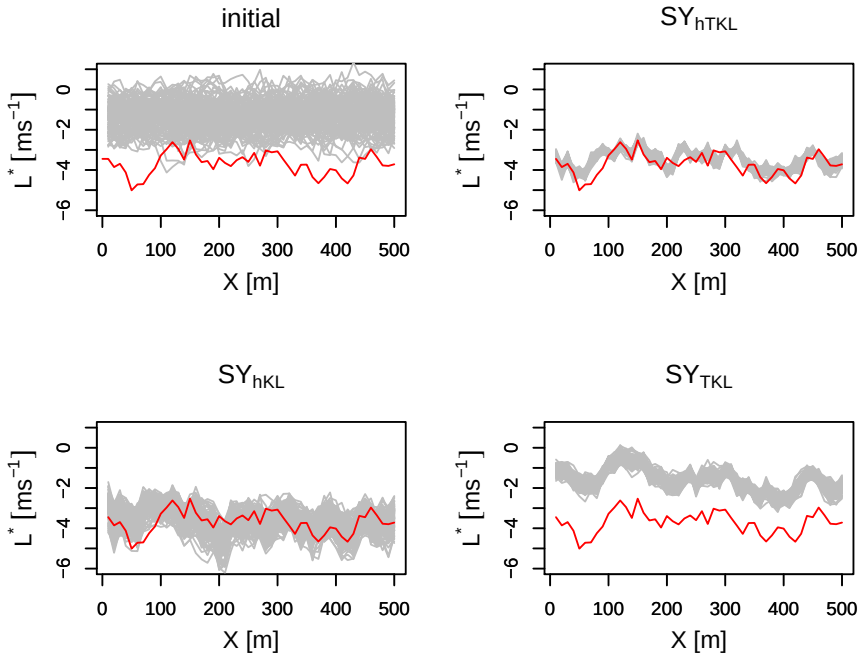

FIGURE 5.11: Updated fields of leakage coefficients (end of simulation period) for scenarios SY_{hKL}, SY_{hTKL} and SY_{TKL} (Table 5.2).

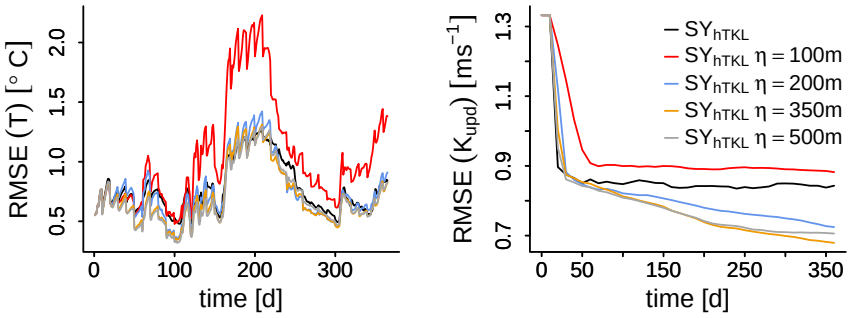

FIGURE 5.12: Root mean square error of groundwater temperatures (left) and hydraulic conductivities (right) for different localization distances (scenario SY_{hTKL} in Table 5.2).

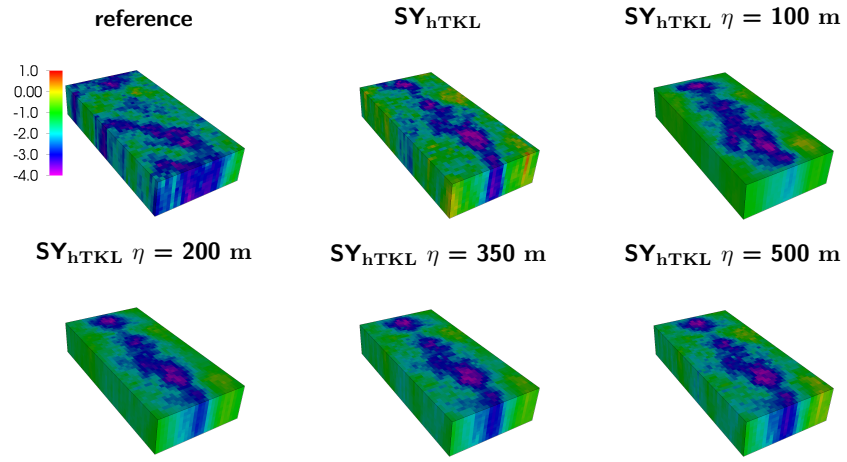

FIGURE 5.13: Updated fields of hydraulic conductivities (end of simulation period) for different localization distances (scenario SY_{hTKL} in Table 5.2).

when the localization limit is increased from 350 to 500 m. The updated K fields for the different localization factors after the last assimilation cycle are compared in Figure 5.13. For the simulation without localization there are some parts where K values were highly increased during the update (e.g., at the most right corner of the model domain). However, these zones with high K values are not present in the reference field and are possibly a cause of spurious correlations related to the limited ensemble size of 128 ensemble members. When localization is used these zones of elevated K values are eliminated or at least reduced during the updating procedure whereby the general structure of updated K values (i.e., reduced values along the river reach) is preserved. This finally leads to lower RMSE values for K for simulations with localization.

5.3.2 Assimilation of groundwater temperature data for real-world case

In this section the results for the assimilation of temperature data for the real-world case are presented. Compared to the synthetic simulations of the previous section the mismatch between ensemble prediction and the reference values of state variables cannot be evaluated for the whole model domain because only data for the measurement locations are available. Additionally, for these simulations the true parameter distribution for K and L is largely unknown and the evaluation of updated parameter values is restricted to visual inspection of the updated parameter fields. Therefore, the errors of h and T are monitored separately for the assimilation period and an additional validation period in which the quality of the updated parameter fields is compared.

5.3.2.1 Assimilation period

Figure 5.14 compares the basic updating scenarios of Table 5.4 in terms of the temporal evolution of RMSE values for h and T at observation points (left panels) and the statistics of residuals at observation points for the whole assimilation period (right panels). For all scenarios and both state variables the assimilation with EnKF improves the prediction of state variables compared to unconditional simulations. Piezometric heads at measurement locations show high fluctuations when only state variables are updated. An additional parameter update leads to relatively constant values of RMSE(h) and there is no observable effect of temperature assimilation on RMSE(h). Similar to results from synthetic experiments, RMSE(T) for unconditional simulations and scenario $\mathrm{RW_{hKL}}$ shows a seasonal cycle. However, for the real-world case this cycle is much less pronounced than for the synthetic case. Also, for RMSE(T) the effect of parameter update is much less pronounced as for RMSE(h) because the mean values of scenario $\mathrm{RW_{hT}}$ are very similar to the mean values of scenario $\mathrm{RW_{hTKL}}$ with respect to RMSE(T). These two scenarios differ mostly with respect to the different magnitude of fluctuations which are higher for scenario $\mathrm{RW_{hT}}$. The different effect of parameter updates for h and T can also be seen in the global error statistics (right panels in Figure 5.14). For piezometric heads there is a significant discrepancy between the median of absolute errors for scenarios $\mathrm{RW_{hT}}$ and $\mathrm{RW_{hKL}}$/$\mathrm{RW_{hTKL}}$. Also the variability of absolute errors is higher when only states are updated. In contrast, for groundwater temperatures there is not so much difference in the error distribution between scenarios $\mathrm{RW_{hT}}$ and $\mathrm{RW_{hTKL}}$. However, the parameter update becomes important also for T when there are gaps in the time series of measurement data for T. This is exemplified in Figure 5.15 which shows the temperature evolution for an observation point with partly missing measurement data. Here, it can be seen that the missing reduction of parameter uncertainty

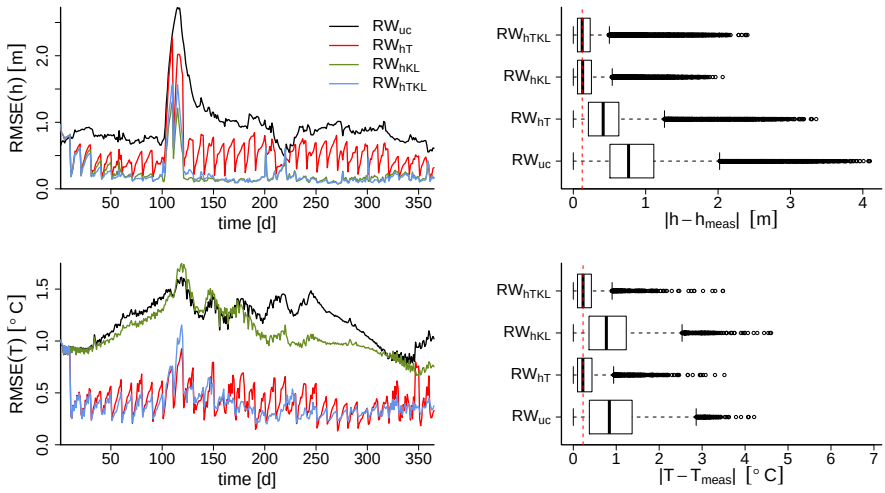

FIGURE 5.14: Temporal evolution of RMSE (left panels) and statistics of residuals for the whole assimilation period (right panels) of h and T for different updating scenarios. The red line in the right panels shows the median of residuals for scenario $\mathrm{RW_{hTKL}}$.

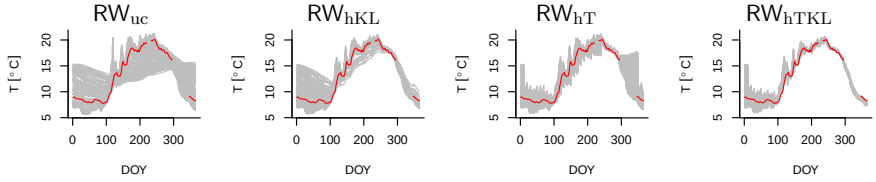

FIGURE 5.15: Evolution of groundwater temperatures during the assimilation period for one observation point with partly missing data. Red lines display measured groundwater temperatures and gray lines display different realizations of the ensemble.

in scenario $\mathrm{RW_{hT}}$ can lead to very biased predictions when no measurement data are available.

Concerning the parameter updates without ($\mathrm{RW_{hKL}}$) and with temperature data ($\mathrm{RW_{hTKL}}$) there are not so much differences in the final fields for hydraulic conductivity (data not shown) but an effect is visible for the final parameter distribution for leakage coefficients (Figure 5.16). Here an additional assimilation of groundwater temperatures led to an overall reduction of uncertainty of the L-ensemble. However, the basic structure of updated L-fields is still very similar to the scenarios without T-assimilation.

In a next step, the effects of observation density and measurement errors on the update of groundwater temperatures and piezometric heads is explored in further detail. The assigned values of measurement errors for h and T that were used for the previous simulations can be seen as optimal values for the measurement devices for that site.

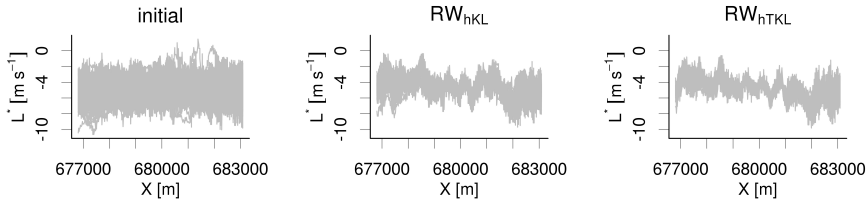

FIGURE 5.16: Initial (left) and updated fields of leakage coefficients after the last assimilation cycle. Updated leakage coefficients are shown for a scenario without (middle) and with (right) assimilation of groundwater temperatures.

However, the accuracy of online-sensors may also decrease over time due to alteration of the measurement device or drifts in the calibration function. Also the flow conditions within the bore hole and the support volume of the measurement device may have an effect on the accuracy of the measurements which are hard to quantify and were not regarded in the previous used values of measurement error. Therefore, the measurement errors for h and T were multiplied with a factor of 5 and 10 and results for the different measurement errors were compared for scenario $\mathrm{RW_{hTKL}}$ (Figure 5.17). Generally, the increase of measurement errors led to higher errors for the estimation of h and T. This is visible from the temporal evolution of RMSE and also from the higher spread of the residuals. This occurs because increasing measurement uncertainty leads to lower weights in the Kalman gain matrix and thus to a decreasing adaptation towards the measurements. However, the effect of measurement errors is slightly different for h and T. For piezometric heads the differences for the three magnitudes of measurement error are not so pronounced as for groundwater temperatures where measurement errors have a higher impact on the assimilation. This discrepancy is related to the different prediction uncertainty for h and T. After the first few assimilation cycles the ensemble spread for groundwater temperatures is very low for most of the observation points and EnKF therefore assigns a high confidence to temperature predictions. Forecasts for piezometric heads show more variability what also leads to higher values in the Kalman gain matrix.

The effect of observation density was investigated for scenarios $\mathrm{RW_{hT}}$ and $\mathrm{RW_{hTKL}}$ by reducing the number observation points for h and T to about half of the values that are principally available for that site. The results for these scenarios are compared in Figure 5.18. For piezometric heads there is not much difference for the scenarios with low and high observation density. Only when parameters are included in the assimilation with EnKF there is some tendency for a higher spread in the error statistics when a lower amount of measurements is used. For groundwater temperatures the situation is very different compared to piezometric heads. In this case the errors rise significantly when only half of the observation points are available for conditioning with EnKF. This relationship can be found for both updating scenarios (states-only and state-parameter

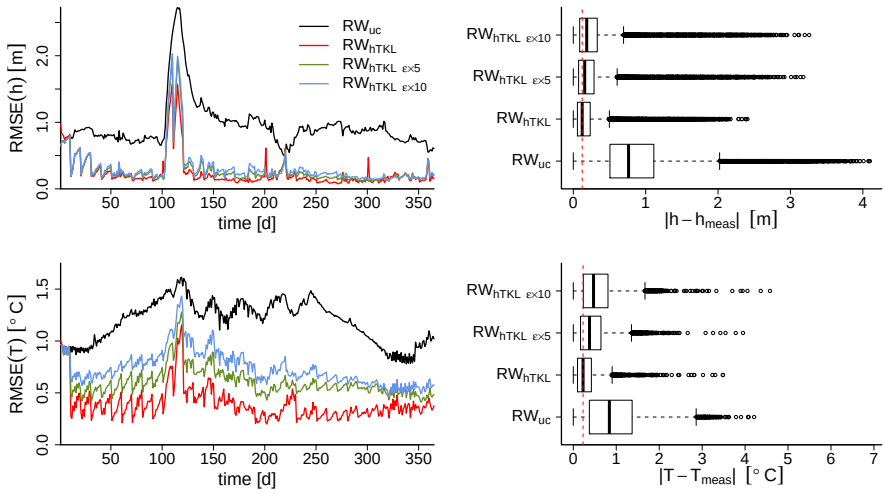

FIGURE 5.17: Temporal evolution of RMSE (left panels) and statistics of residuals for the whole assimilation period (right panels) of h and T for different measurement errors. $\epsilon \times 5$ and $\epsilon \times 10$ means a five or ten times higher measurement error compared to the settings give in Table 5.3. The red line in the right panels shows the median of residuals for scenario $\mathrm{RW_{hTKL}}$.

update) with a slight tendency towards higher errors for the states-only scenario. The relatively low sensitivity towards observation density for piezometric heads is probably an effect of the higher abundance of piezometric head measurements for this site, i.e., there are four times more piezometric head measurements available than measurements of groundwater temperature. Using only 40 piezometric head measurements instead of 87 thus still gives enough information on the system dynamics and there is a certain amount of redundant information for the 87 piezometers. An additional reason for the different error statistics of h and T with respect to observation density could be the different correlation length of both variables. Groundwater levels for that site are relatively smooth due to the high permeability of the unconfined aquifer whereas groundwater temperature is mainly driven by river-aquifer exchange due to pumping and by the artificial recharge which leads to a small scale variability of the temperature distribution within the model domain. As a consequence, a single measurement of piezometric head gives more information on the surrounding area than a measurement of groundwater temperature which affects the critical amount of data that are necessary to constrain the system states with EnKF.

In a next step it was tried to identify the effect of localization on the state-parameter updates with EnKF. Localization with two different η values (2000 m and 3000 m) was compared with the standard assimilation scheme for scenario $\mathrm{RW_{hTKL}}$. Results for the different localization scenarios (Figure 5.19) show that the errors of piezometric

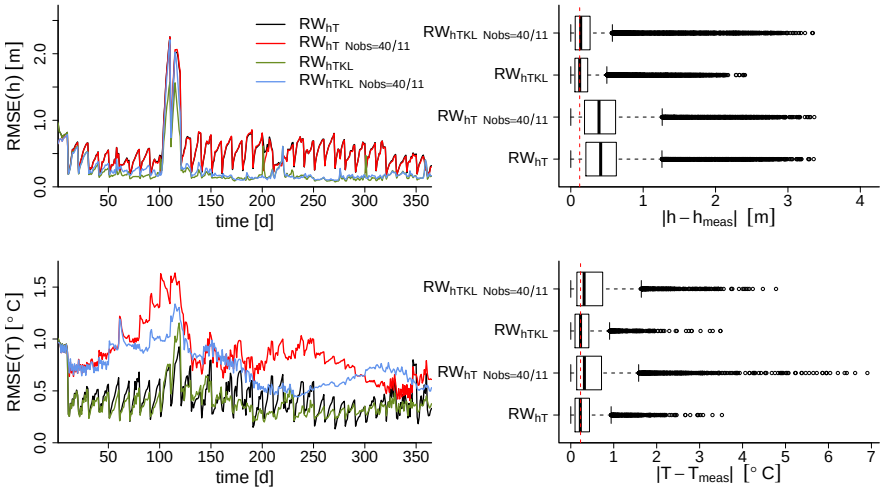

FIGURE 5.18: Temporal evolution of RMSE (left panels) and statistics of residuals for the whole assimilation period (right panels) of h and T for different observation density with and without parameter update. The red line in the right panels shows the median of residuals for scenario $\mathrm{RW_{hTKL}}$.

heads slightly increase when localization is used. In contrast, the observed errors for groundwater temperature are not so sensitive to localization. For a localization length scale η of 2000 m there is a slight decrease in error variance but the median value is approximately the same as for the simulation without localization. The different behavior of h and T with respect to localization could again be related to the different correlation length of both variables. Figure 5.20 shows examples of covariance structures for representative observation points of h and T that were derived from scenario $\mathrm{RW_{uc}}$ for time step 200. It can be seen that the covariances for h have a much longer range than for T. When such a covariance function is then tapered with a localization function that has a smaller spatial extent, information may be lost in the assimilation with EnKF. For groundwater temperatures the spatial correlation is much lower and therefore fits better within the range of the utilized localization function.

The effect of localization on the parameter updates with EnKF can be seen in Figures 5.21 to 5.23. Figure 5.21 shows the final updated fields for L for the different scenarios with localization. Without localization the variability in the L-ensemble decreased for the whole river reach and a distinct spatial pattern is visible in the final ensemble. When localization is used only the part of the river that is close to the management activities shows a significant reduction in ensemble variance because here the highest density of observation points can be found. In addition, the observation points are also much closer to the river in this area than in other parts of the model.

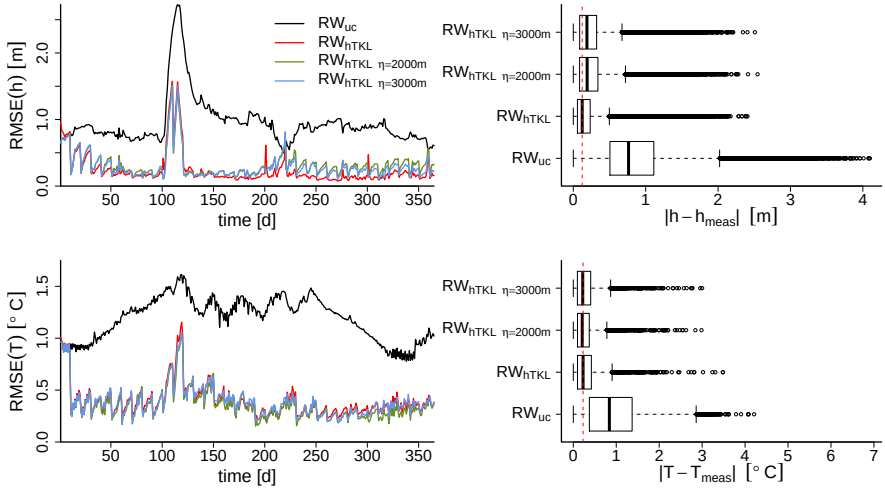

FIGURE 5.19: Temporal evolution of RMSE (left panels) and statistics of residuals for the whole assimilation period (right panels) of h and T for different values of the localization length scale η. The red line in the right panels shows the median of residuals for scenario $\mathrm{RW_{hTKL}}$.

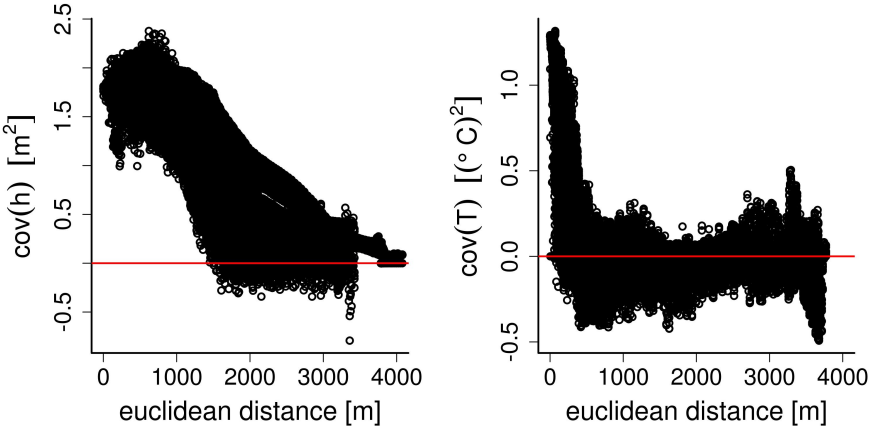

FIGURE 5.20: Examples for the spatial distribution of covariances for piezometric heads (left) and groundwater temperatures (right). Covariances were derived from data of scenario $\mathrm{RW_{uc}}$ for time step 200 of the assimilation period. Data are shown for one observation point of piezometric heads and groundwater temperatures respectively.

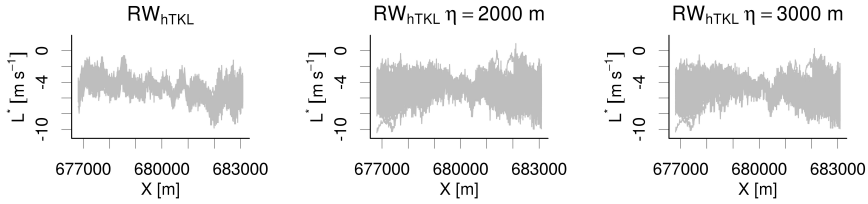

FIGURE 5.21: Updated fields of leakage coefficients after the last assimilation cycle. Data are shown for a scenario without localization and two scenarios with localization with a different localization length scale η (2000 and 3000 m).

The spatial distribution of hydraulic conductivities at the end of the assimilation period is visualized in Figures 5.22 and 5.23. Figure 5.22 displays an overview of the spatial distribution of K-values and Figure 5.23 is a cross-section that is centered in the drinking water well most close to the river which should give additional insight into the vertical distribution of updated K-values close to the river. From both Figures it is obvious that the parameter update for K with unlocalized EnKF leads to a relatively patchy structure and a high degree of spatial variability where neighboring cells can exhibit considerable contrasts in terms of K-values. On the one hand, this is related to the high amount of degrees of freedom for the parameter update with EnKF, i.e., observation data are used to update the parameters of each grid cell separately to reduce the misfit between observations and forecasted state variables. On the other hand, spurious correlations due to the limited ensemble size may also play a role in this context and could emphasize a certain randomness in the assimilation procedure. Localization generally leads to a smoothing of the updated K-fields. From the cross-section of Figure 5.23 it can be seen that the scenarios with and without localization yield approximately the same spatial structure of K-fields at the end of the assimilation period. However, localization reduces the amount of more extreme K-values and the transition between neighboring cells is much more gentle than for the update with unlocalized EnKF.

5.3.2.2 Validation period

In this section the quality of the updated parameter ensembles from the assimilation period is accessed with validation runs for the hydrological year 2011. Figure 5.24 shows the errors for h and T for different updating scenarios (with and without update of groundwater temperatures and unconditional) and a variation of observation density (87/22 versus 40/11 observation points for h and T). Compared to the unconditional simulations the scenarios with updated parameter ensembles show a significant reduction in RMSE(h). Differences between the scenarios with updated parameters are relatively low in terms of RMSE(h) and the range of residuals. For groundwater temperatures

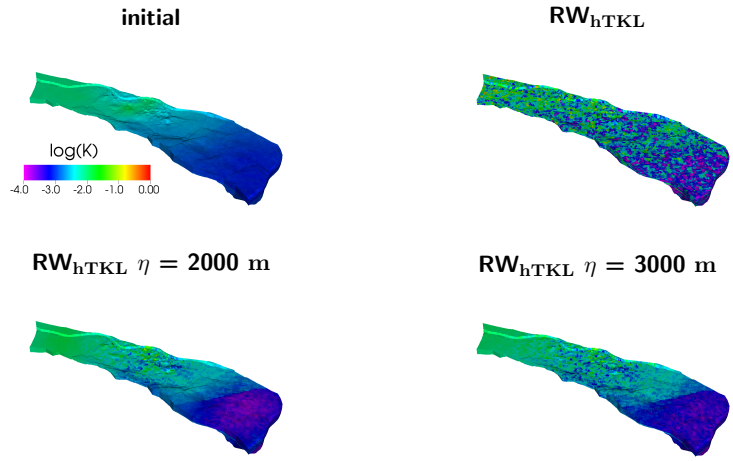

FIGURE 5.22: Mean fields of hydraulic conductivity after the last assimilation cycle for parameter update without localization and with localization with two localization length scales η (2000 and 3000 m). As a comparison the average initial field of hydraulic conductivities is shown.

the updated parameter ensembles do not perform as well as for piezometric heads. An improvement is clearly visible but it is lower in magnitude compared to piezometric head data. From the temporal evolution of RMSE(T) it cannot clearly be distinguished which of the updating scenarios performs better throughout the validation period. In the first phase the scenarios with a T-update in the assimilation period have lower errors than the ensemble without T-update. However, in the last phase of the validation period this relationship reverses and the ensemble for RW$_{\mathrm{hKL}}$ gives better results than the one for RW$_{\mathrm{hTKL}}$. The global error statistics also suggest that there is not a big difference for the ensemble with and without update of groundwater temperatures.

When the measurement error is increased during the assimilation period (Figure 5.25) RMSE(h) increases for an event of increased groundwater withdrawal around time step 100 but is very similar to the ensemble with lower measurement error for the rest of the validation period. RMSE(T) behaves very similar to the ensemble with lower observation density (Figure 5.24), i.e., RMSE(T) is very similar to the scenario with standard values for most of the validation period and is slightly decreased in the last phase of the validation period.

Figure 5.26 additionally compares the performance of the ensemble with and without localization. For groundwater temperatures there is a small positive effect of localization in terms of RMSE(T) but the spread of residuals is also a bit higher for the scenarios with localization. A stronger effect of localization can be seen for RMSE(h) where the

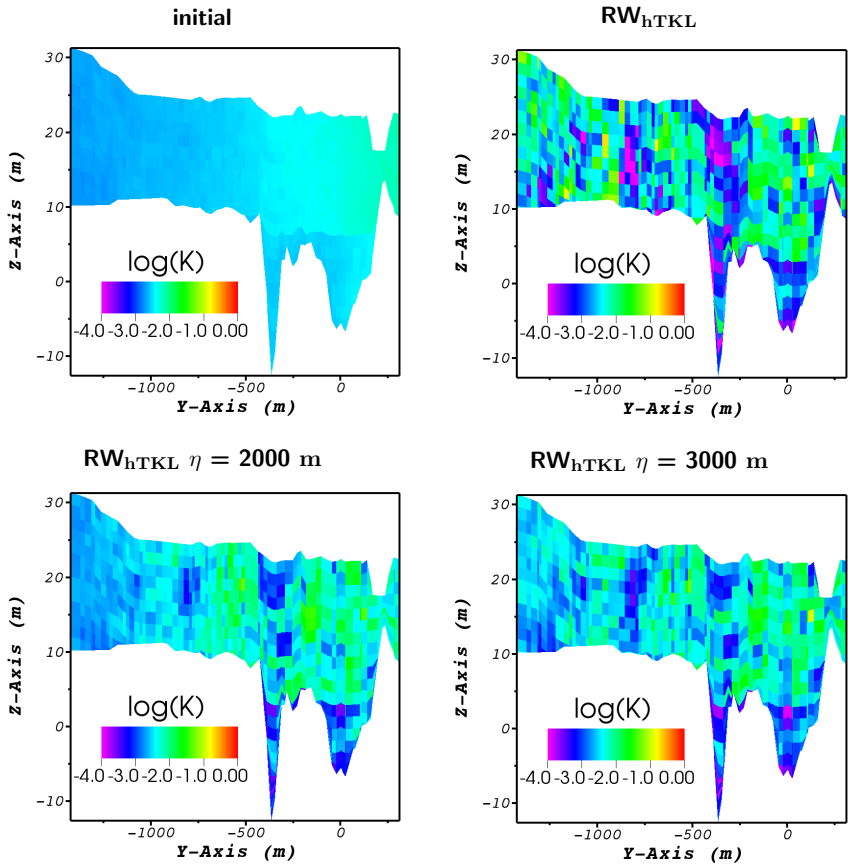

FIGURE 5.23: Cross-sections (y-z plane) of the ensemble mean of hydraulic conductivities for the drinking water well most close to river Limmat. Coordinates of the subfigures are given relative to this drinking water well. Data are shown for one scenario without localization, two scenarios with different localization length scales η (2000 and 3000 m) and the initial ensemble mean.

ensemble with localization show a significant increase compared to the scenario without localization. The relatively constant bias between the scenarios with and without localization suggests that there is a systematic misinterpretation in the groundwater dynamics for the localized ensembles. This systematic bias could be related to the effect of localization on the estimation of L-fields that was already shown in Figure 5.21. When localization is used the parameter fields for L are not constrained as well as for the unlocalized ensemble and a much higher variability is present in the localized ensembles. This can then lead to a systematic overestimation of leakage fluxes which directly affects the mass balance in the aquifer and leads to a bias in the predicted groundwater levels. Figure 5.27 shows the temporal evolution of exchange fluxes and statistics for

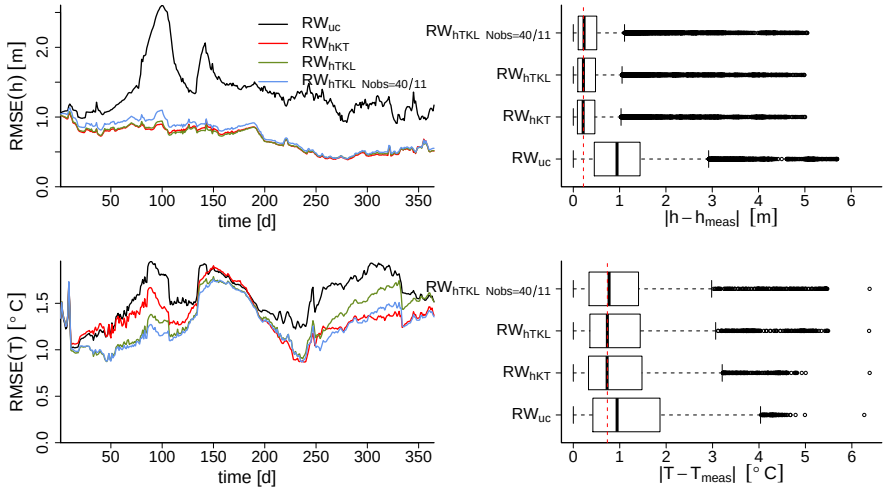

FIGURE 5.24: Temporal evolution of RMSE (left panels) and statistics of residuals for the whole validation period (right panels) of h and T for different updating scenarios. The red line in the right panels shows the median of residuals for scenario $\mathrm{RW_{hTKL}}$.

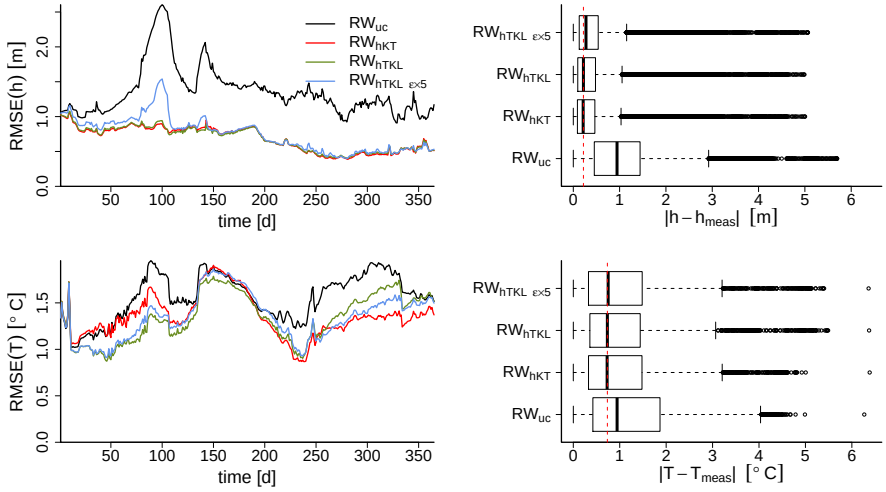

FIGURE 5.25: Temporal evolution of RMSE (left panels) and statistics of residuals for the whole validation period (right panels) of h and T for different updating scenarios and measurement errors. The red line in the right panels shows the median of residuals for scenario $\mathrm{RW_{hTKL}}$.

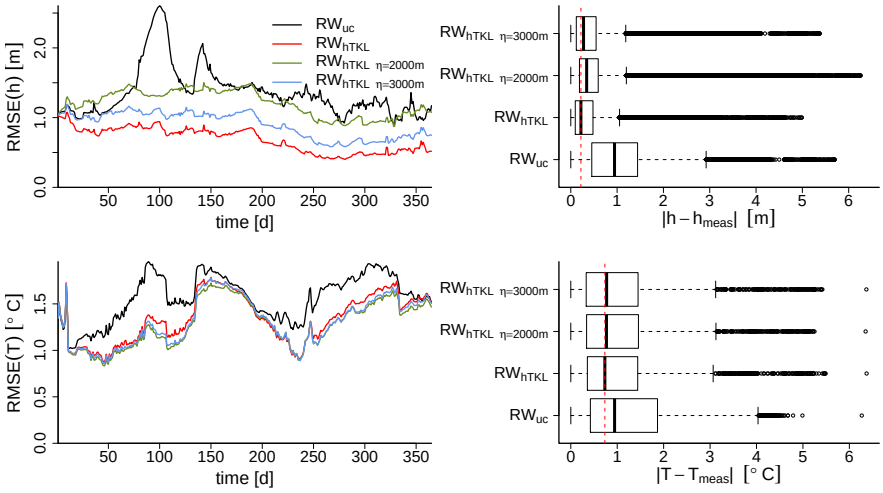

FIGURE 5.26: Temporal evolution of RMSE (left panels) and statistics of residuals for the whole validation period (right panels) of h and T for different values of localization length scale η. The red line in the right panels shows the median of residuals for scenario $\mathrm{RW_{hTKL}}$.

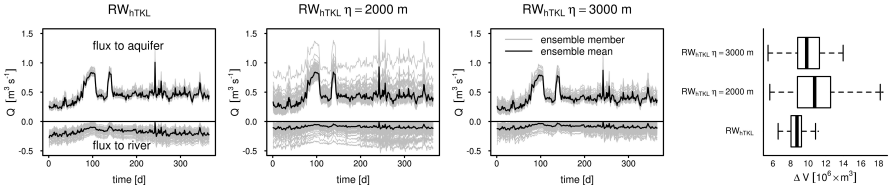

FIGURE 5.27: Exchange fluxes between river and aquifer for the validation period of different localization scenarios. The right hand diagram additionally shows statistics for the total amount of exchanged water for the whole validation period.

the net exchange between river and groundwater. It is obvious that the scenario with localization show a higher degree of uncertainty for the exchange fluxes and that the net exchange is higher for these scenarios compared to the run without localization.

5.3.2.3 Zonation of leakage coefficients for heat transport simulations

The results from Chapter 4 suggested that a higher spatial resolution of leakage parameters leads to a better estimation of river-aquifer exchange fluxes and groundwater levels. Therefore, in this section it is also tested whether this relationship can also be observed for the real-world data of the Limmat aquifer. The setup for these simulations was similar as for scenario $\mathrm{RW_{hTKL}}$ with the only difference that the four ensembles for leakage parameters of Chapter 4 ($\mathrm{Z_{het}}$, $\mathrm{Z_5}$, $\mathrm{Z_3}$ and $\mathrm{Z_2}$) were used instead of the

L-ensemble of $\mathrm{RW_{hTKL}}$ (see Section 5.2.5). Figure 5.28 shows the updated ensembles of leakage coefficients at the end of the assimilation period. It can be seen that the ensemble variance for the zonated ensembles decreases very much also for the real-world data. The errors for h and T (data not shown) are very similar for the four ensembles during the assimilation period. Also the exchange fluxes between river and aquifer and the associated uncertainty did not show significant differences for the four ensembles.

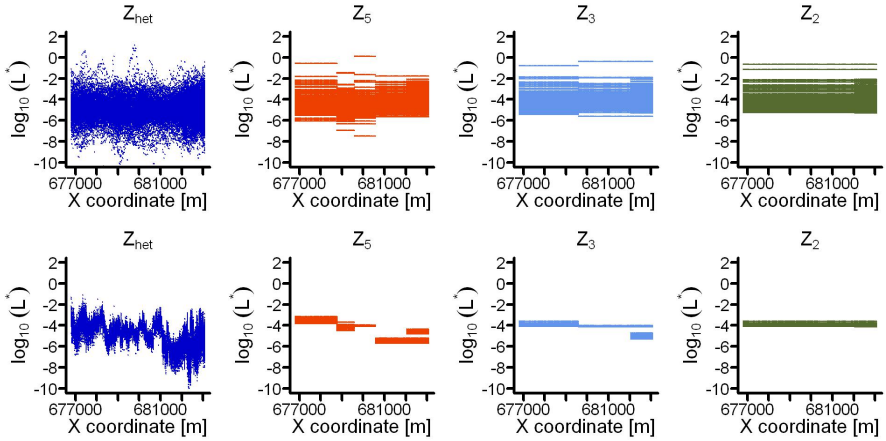

FIGURE 5.28: Initial (upper diagram) and updated (lower diagram) ensembles of leakage coefficients for four different zonation approaches. Values are shown along the x-axis of the model domain. Note that in the eastern part of the model domain there is an overlap of river Sihl and Limmat with respect to x-coordinates.

In Figure 5.29 the errors of piezometric heads and groundwater temperatures are compared for the validation period. As for the assimilation period the differences between the four ensembles are relatively low. For ensemble $\mathrm{Z_{het}}$ there is a tendency towards lower values of RMSE(h) throughout most of the validation period. However, for the phase of intensive pumping at around time step 100 there are higher deviations for $\mathrm{Z_{het}}$ compared to the other three ensembles. Also for groundwater temperatures there is no clear distinction with respect to the performance of the four ensembles of leakage parameters. $\mathrm{Z_{het}}$ shows slightly better RMSE(T) values for the two-thirds of the validation period but errors increase in the last third of the validation period.

5.4 Discussion

Results for the synthetic experiments suggest that a joint assimilation of piezometric heads and groundwater temperatures with EnKF principally can lead to an improvement in the estimation of subsurface parameters compared to an assimilation of piezometric

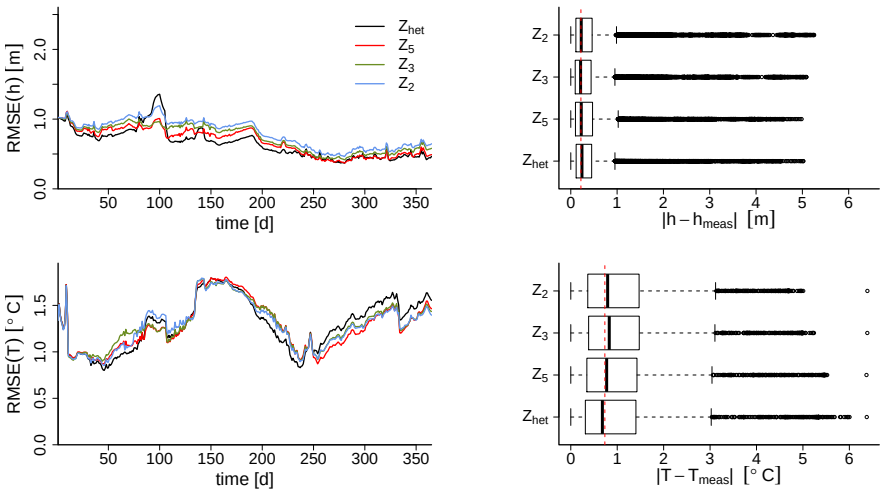

FIGURE 5.29: Temporal evolution of RMSE (left panels) and statistics of residuals for the whole validation period (right panels) of h and T for four different zonation approaches. The red line in the right panels shows the median of residuals for scenario $\mathrm{RW_{hTKL}}$.

head data alone. Assimilated temperatures mainly gave additional information on the spatial distribution of river-aquifer exchange and the corresponding leakage parameters whereas assimilated piezometric head data gave information on the overall magnitude of exchanged water. This relationship was not so clear for the real-world data of the Limmat aquifer. In this case, the additional assimilation of groundwater temperatures also led to a certain reduction of the uncertainty for the spatial distribution of leakage coefficients compared to an assimilation of piezometric head data alone. However, this additional restriction of parameter values did obviously not have a persistent effect on the state predictions. This could be seen from the validation runs with updated parameter fields with and without assimilation of groundwater temperatures which gave very similar results in terms of temperature and piezometric head predictions. Generally, the model for the real-world case seems to already capture the most important system dynamics with respect to heat transport. This becomes obvious from the relatively low errors for the unconditional simulations and also from the simulated values at the observation points which already capture the seasonal temperature dynamics that were measured for several observation points. Additionally, the results for simulations with different representations of river bed heterogeneity (Section 5.3.2.3) suggest that the real-world model is not so sensitive to the spatial resolution of river bed properties because results for the assimilation as well as the validation period were very similar for the different spatial representations of the river. Of course, the river bed properties and their spatio-temporal variations for the real-world case are largely unknown as there

are no direct measurements of this variable available. However, if the river bed in the real-world case really does not show major spatial variations then this would explain why an additional assimilation of groundwater temperatures does not significantly improve parameter estimation because the synthetic experiments already showed that the most important effect of temperature assimilation is related to the identification of the spatial structure of leakage parameters. So, if the river bed is relatively homogeneous for the real-world case, groundwater temperatures do not provide much additional information for river-groundwater exchange and the most important information comes from groundwater levels which constrain the net exchange and thus the mass balance between river and aquifer.

From the assimilation experiments for the real-world case it also became obvious that the model dynamics for some parts of the model could not be well corrected with EnKF. This observation especially refers to the temperature dynamics monitored at two multi-level piezometers south of the recharge basins and recharge wells. At these locations the model indicated as small seasonal temperature variation during the assimilation and validation period but the measured groundwater temperatures are very constant for both periods. In the simulations these piezometers seem to be influenced by the artificial recharge which causes the seasonal temperature variation but this does not reflect the true conditions in that area. EnKF was obviously not able to adapt model parameters to adjust model dynamics for this area towards the true conditions. From geological surveys for the Hardhof area it is known that there are some channel structures within the Hardhof area which facilitate preferential flow conditions for a part of the managed site. These geological structures are not included in the initial ensemble of K-values that was used for data assimilation what could be a reason for the poor adaptation of model parameters with EnKF for the area south of the artificial recharge. Another reason could lie in an erroneous definition of boundary conditions for that area. In the model all recharge wells are assumed to operate with the same injection rate which is often not fulfilled in real-world conditions. Thus, there is also the possibility that there are structural errors present in the model which cannot be corrected by parameter estimation with EnKF. Both possibilities (lack of certain geological structures in the initial ensemble and errors in the model forcings) emphasize that the application of EnKF for real-world data is accompanied by a higher degree of uncertainty which could reduce the effectiveness of the method.

Localization had a relatively clear effect on the estimation of states and parameters for the synthetic experiments. Here, localization could reduce the effect of spurious correlation during the assimilation with EnKF. For the real-world case this relationship is not so clear as for the synthetic case. In the real-world application the model dynamics are more complicated and also the spatial distribution of observation points is not as

regular as for the synthetic model setup. The comparison of covariance structures for piezometric heads and groundwater temperatures already showed that there are large differences concerning the spatial correlation for the two variables. It was also found that localization can greatly affect the prediction of exchange fluxes between river and aquifer when it is applied for the estimation of leakage parameters. For the model setup of the real-world case the initial ensemble of leakage coefficients was highly variable and the observation points were not distributed evenly along the river reach. When localization is used for such conditions it is not possible to constrain the parameters that are very distant from the observations which could then lead to a significant misinterpretation of exchange fluxes. Therefore, the localization scheme that was used for the different assimilation experiments is probably too generalized for the application in the real-world case because only one length scale is used for the distant-dependent localization. For the different state variables it seems desirable to introduce a separate localization length scale η for piezometric heads and for groundwater temperatures because their covariance structures vary considerably. Additionally, the relationship between the ensemble variance of model parameters and the localization scheme should be considered carefully before localization is applied in data assimilation with EnKF. One goal of localization beneath the reduction of spurious correlations is to maintain a certain ensemble variance throughout the assimilation process. However, the results for applying localization to river bed properties showed that when the initial ensemble spread is very high this can lead to a systematic bias between model predictions and measurement data because the highly variable parameters in some parts of the model cannot be updated any more when localization is used. The application of localization on the update of hydraulic conductivities seemed to have a more positive effect because the tendency towards relatively extreme values for hydraulic conductivities with high spatial variations was reduced during the updating procedure. For this parameter observation points were distributed more evenly over the model domain and also the initial ensemble was better constrained compared to the initial ensemble of leakage coefficients. Thus, it is concluded that the application of distance-depend localization requires a careful tuning and adaption towards the specific conditions of a model. This adaption should consider the estimation of the variability of model parameters, the specific covariance structures of the model states and parameters as well as the availability and spatial distribution of observations.

5.5 Conclusions

In this chapter a simplified model of a river-aquifer system and data from the real-world case of the Limmat aquifer in Zurich were used to identify the usefulness of a

joint assimilation of piezometric head and groundwater temperature data for the prediction of aquifer states and the identification of hydraulic subsurface parameters. For the synthetic river-aquifer model the joint assimilation of piezometric heads and groundwater temperatures resulted in the best estimate of hydraulic properties (i.e., hydraulic conductivities and leakage coefficients). However, the additional assimilation of temperatures only led to an improvement of about 5 % in terms of RMSE for each of the parameters where the overall reduction in RMSE in the best case was about 37 % for hydraulic conductivities and 78 % for leakage coefficients. With respect to leakage parameters the assimilated piezometric head data mainly gave information on the magnitude of river-aquifer exchange fluxes and assimilated temperature data led to a better characterization of the spatial distribution of leakage parameters. Results for the real-world case indicate that a good prediction of groundwater temperatures can be achieved through data assimilation with EnKF under real-world conditions where the best results were obtained with a simultaneous update of model parameters. However, validation experiments revealed that for the real-world case most of the improvement of model parameters is dedicated to the information coming from assimilated piezometric heads and that the additional assimilation of temperature data did not lead to a significantly better prediction capability of the updated parameters. The effect of distance-dependent localization was relatively straightforward for the synthetic river-aquifer system because it could easily be identified from the updated parameter fields that non-physical parameters updates were suppressed through the tapering with the localization function. For the real-world case, localization also seemed to have a significant impact on the updated parameter fields. This was mainly observed for the fields of aquifer hydraulic conductivities where localization lead to a relatively strong smoothing effect compared to the updating scheme without localization. This smoothing also prevented the buildup of extremer parameter values which was observed for the standard EnKF. However, it also became clear that the localization limit should to be carefully chosen in order to honor the different physical relationships of model variables. A further issue related to the use of localization is that the effective range of the localization function and the variance in the initial parameter ensemble have to be balanced very carefully. For example, when the initial variability of a parameter which is important for the system dynamics is set too high this can lead to a bias in the prediction capability of the model when localization is used. This is because the high variability of the model parameter cannot be reduced through subsequent updates with EnKF in certain parts of the model due to localization. Further research is required to find an optimal strategy for the simultaneous localization of different model variables under complex system dynamics.

Chapter 6

Summary and outlook

In this work, different data assimilation experiments were performed with a 3D groundwater model of the Limmat aquifer in Zurich. For this study site a real-time modeling system has recently been put into practice which aims to enhance the management of a well field. In this modeling system, data from a dense monitoring network are used to improve the predictions of groundwater levels and model parameters through data assimilation with the Ensemble Kalman Filter (EnKF). An important aspect for the real-time modeling system at this site is that the groundwater management is highly influenced by river-aquifer exchange fluxes. Therefore, this study specifically aims to investigate the relation between the spatio-temporal variability of river bed hydraulic parameters and the application of EnKF for such systems. Another focus of this work is to include the assimilation of groundwater temperatures in the data assimilation framework of EnKF for this site. In the well field of the Limmat aquifer, also a monitoring network of groundwater temperatures is available and there is a growing interest to also get reliable predictions for the temperature distribution of the well field for management purposes. Furthermore, these data can be used as an additional source of information for the determination of hydraulic aquifer and river properties with EnKF. In order to investigate the effects of spatio-temporal pattern of river bed properties and the additional assimilation of groundwater temperatures on the performance of EnKF different data assimilation experiments were performed: In two sets of experiments a synthetic model that mimics the Limmat aquifer was used. In these sets of experiments most of the model parameters and model forcings where taken from real-world data and only the spatio-temporal patterns of leakage parameters were generated artificially. In a further step also the assimilation of groundwater temperature data was included in the EnKF analysis scheme. The worth of this additional source of information was assessed for a simple synthetic model of river-aquifer exchange and also for the Limmat aquifer model with real-world data.

The synthetic experiments on spatio-temporal patterns of river bed hydraulic conductivities revealed that EnKF is well suited for the detection of temporal changes in the river bed. Although there was a certain time-lag in the adaptation of leakage parameters, EnKF was able to adjust parameters under various proposed sedimentation/erosion regimes and the overall accuracy of adapted parameters was very promising. This is important in the light of real-time-prediction for the operation of well fields close to rivers because temporal changes of river bed properties can have a significant effect on model predictions as has been shown for example by Doppler et al. (2007).

An important aspect in this sense is also that EnKF was able to retrieve the basic structure of unknown heterogeneous fields of river bed permeabilities. In terms of computational efficiency, the introduction of heterogeneity in the initial ensemble hardly influences the required computation time. At the same time, predictions with fully heterogeneous fields of leakage parameters provided a better assessment of river-aquifer exchange fluxes and model parameters than similar simulations with effective parameters.

In order to perform data assimilation experiments on the joint assimilation of piezometric heads and groundwater temperatures, a first step was to parallelize the data assimilation algorithm for EnKF. This step was necessary to accomplish a reasonable computation time for the data assimilation experiments because the coupled simulation of flow and heat transport for a large number of model realizations constitutes a significant computational burden. The parallelized assimilation code scaled up well to 128 processors with an estimated efficiency of about 70 %. The synthetic experiments on the joint assimilation of hydraulic and thermal data highlighted that the information content of both measurements can contribute to the improvement of the estimation of uncertain subsurface parameters. In these experiments temperature data were especially useful for a more detailed characterization of the spatial structure of river bed permeabilities. For the real data of the Limmat aquifer such a clear relationship regarding the improvement of model parameters was not observed. The assimilation of temperature data during the calibration period led to a reduction in the variability of leakage parameters. However, during the verification period there was no indication from the simulated data that this leads to a better prediction capability of the model. For these experiments the errors in temperature prediction were already rather low for unconditional simulations without state-parameter updates and the question remains whether this low discrepancy between modeled and measured data was sufficient to allow for an improved parameter estimation.

Adaptive covariance inflation and localization showed to be interesting and important amendments for subsurface characterization with EnKF because they allow to correct

for some deficiencies in the EnKF updating scheme, like filter inbreeding and the effect of a limited sampling of uncertainty due to the finite ensemble size. Although localization has already been used in different studies on the estimation of subsurface parameters, there are still some open questions regarding the optimal choice of range parameters for different variables. Another open questions concerns the relation of localization parameters to ensemble variance. Adaptive covariance inflation was used for the first time in conjunction with subsurface characterization and first results suggest that this methodology is also well suited for groundwater modeling. Thus, this subject should be investigated in more detail in further studies.

From these first detailed experiments on the use of EnKF in river-aquifer systems it is concluded that data assimilation with EnKF is an interesting and promising tool to improve the prediction capability of river-aquifer models. Of course, some of the results were derived on the basis of idealized and simplified conditions. This holds, for example, for the synthetic experiments on spatio-temporal variations of river bed properties. The dynamics of sediment transport in natural river systems are usually very complex and lead to distinct patterns of heterogeneity in the river bed (e.g., riffle-pool sequences). Also the temporal variation of river sediments depends on many factors like the sediment load of the river, morphological aspects of the river course and discharge characteristics. This can, of course, lead to very complex spatio-temporal patterns of river bed properties. Such patterns are only partly captured by the utilized reference scenarios of this study and they also do not link the relationship between temporal and spatial changes in the river bed. For further investigations on this topic it would therefore be desirable to also generate the spatio-temporal patterns of river bed sediments on the basis of hydrodynamic sedimentation models that could provide patterns which closer resemble natural sediment dynamics. A further improvement towards more realistic conditions of river-aquifer systems concern the generation of the hydraulic conductivity fields. In this study, the ensembles of hydraulic conductivity were generated under a Gaussian assumption which often does not reflect the true sedimentological structure of alluvial systems which are often characterized by distinct geological structures such as paleo-channels. Object-based generation algorithms for geological structures which also account for the spatial arrangement of hydrofacies are becoming more and more available. Such models offer the chance to reduce the model structural error during the assimilation with EnKF what could lead to a better characterization of river-aquifer systems. Of course, this would require further modifications to the EnKF assimilation algorithm as has already been shown by Zhou et al. (2011) and Schöniger et al. (2012). Another aspect that should deserve more attention in upcoming investigations is the coupling between surface water and groundwater that is used in the forward model of EnKF. In this study, the commonly applied leakage principle is used for the calculation

of exchange fluxes between river and aquifer. However, more sophisticated methods for the coupling of surface water and groundwater have been proposed and parameter estimation with EnKF could also benefit from these more physically based approaches. However, these approaches usually require a very detailed representation of the saturation conditions underneath the river. This raises questions about the computational effort of such approaches in a data assimilation framework and also about the stability of such solutions when the unsaturated zone is represented in more detail because this can also introduce more non-linearities in the forward model. Comparisons between such approaches and the leakage principle with respect to data assimilation with EnKF could clarify the merits and drawbacks of both methodologies. The joint assimilation of hydraulic and thermal data that was applied in this study has already highlighted the benefits of using multiple sources of information for the application of EnKF in river-aquifer systems. Especially in this field, new measurement techniques are emerging and one promising tool for the characterization of river-aquifer exchange is Distributed Temperature Sensing (DTS). This techniques allows to retrieve temperature distributions around streams with a high spatial and temporal resolution and is therefore well suited as an additional information source in EnKF especially for river-aquifer models with a high spatial resolution.

Appendix A

Algorithm for adaptive covariance inflation

In accordance with Anderson (2007) a Bayesian updating scheme is used to calculate the inflation factor λ for each assimilation step. In this updating scheme the simulated ensemble estimate at observation points $\hat{\boldsymbol{\psi}}$, the measurement at observation points $\boldsymbol{y}^0$ and their respective variances $\sigma^2_{\hat{\psi}}$ and $\sigma^2_{y^0}$ are used to estimate a new value of λ in order to correct the model ensemble for effects of filter divergence. The basic updating equation for the assimilation time step $t_{a,i}$ can be stated as:

$$p(\lambda, t_{a,i}) \sim p(\boldsymbol{y}^0 \mid \lambda)\, p(\lambda, t_{a,i-1}) \tag{A.1}$$

where $p(\lambda, t_{a,i})$ is the posterior probability distribution of λ, $p(\lambda, t_{a,i-1})$ is the prior probability distribution and $p(\boldsymbol{y}^0 \mid \lambda)$ is a likelihood term that describes the probability that $\boldsymbol{y}^0$ is observed given a certain λ.

The prior distribution in Equation A.1 is assumed to follow a normal distribution:

$$p(\lambda, t_{a,i-1}) = \mathcal{N}(\bar{\lambda}_p, \sigma^2_{\lambda,p}) \tag{A.2}$$

where the index p refers to the previous value of λ and σ^2_λ is the variance of λ.

It is also assumed that the prior of λ is identical to the posterior from the last assimilation cycle. The likelihood term in Equation A.1 is also expressed as a normal distribution:

$$p(\boldsymbol{y}^0 \mid \lambda) = (\sqrt{2\pi}\chi)^{-1} \exp(-{D_y}^2/2\chi^2) \tag{A.3}$$

where D_y is the absolute distance between the simulated ensemble mean at observation points $\hat{\boldsymbol{\psi}}_m$ and the measured value $\boldsymbol{y}^0$:

$$D_y = \mid \hat{\boldsymbol{\psi}}_m - \boldsymbol{y}^0 \mid \tag{A.4}$$

and χ is a measure for the variability of this distance for a certain value of λ:

$$\chi = \sqrt{\lambda \sigma^2_{\hat{\psi}} + \sigma^2_{y^0}} \tag{A.5}$$

Inserting the equations of the prior and the likelihood function into Equation A.1 gives:

$$p(\lambda, t_{a,i}) \sim (\sqrt{2\pi}\chi)^{-1} \exp(-{D_y}^2/2\chi^2)\, \mathcal{N}(\bar{\lambda}_p, \sigma^2_{\lambda,p}) \tag{A.6}$$

For the determination of the inflation factor $\bar{\lambda}$ for the current assimilation cycle $\bar{\lambda}$ is set equal to the mode of Equation A.6 which is found by differentiating the right hand side of A.6 and setting it to zero. This results in a cubic equation of the form:

$$x^3 - (\sigma^2_{y^0} + \bar{\lambda}\, \sigma^2_{\hat{\psi}})\, x^2 + \frac{1}{2}\, \sigma^2_{\lambda}\, \sigma^4_{\hat{\boldsymbol{\psi}}}\, x - \frac{1}{2}\, \sigma^2_{\lambda}\, \sigma^4_{\hat{\boldsymbol{\psi}}}\, {D_y}^2 = 0 \tag{A.7}$$

where $x = \chi^2$. Solving this equation with the cubic formula and substituting the results into Equation A.5 gives the value of λ for the respective observation.

The utilized algorithm for covariance inflation in this study can be summarized as follows:

1 Propagate the ensemble forward until the next observations $\boldsymbol{y}^0$ are available

2 Determine $\hat{\boldsymbol{\psi}}_m$ and $\sigma^2_{\hat{\psi}}$ from the ensemble

3 For each observation of $\boldsymbol{y}^0$ do the following steps:

   (a) Determine D_y with Equation A.4

   (b) Solve Equation A.7 for x and insert the result in Equation A.5 to determine λ

4 From the distribution of λ calculate $\bar{\lambda}$ and update the state-parameter vector $\boldsymbol{\Psi}$ according to Equation 3.13

In the implementation of this algorithm the variance of the inflation factor σ^2_{λ} was set to a constant value of 0.25 instead of using a model for the evolution of this parameter as it was done in Anderson (2007). This was also suggested as an algorithmic variant by

Anderson (2009). Additionally, a constraint was put on the values of $\bar{\lambda}$ by setting values of lower than 1 which could occur when the filter is very confident (i.e., low residuals) to a value of 1.

Bibliography

Aanonsen, S. I., Naevdal, G., Oliver, D. S., Reynolds, A. C., and Valles, B. (2009). The Ensemble Kalman Filter in Reservoir Engineering-a Review. *SPE J.*, 14(3):393–412.

Alcolea, A., Carrera, J., and Medina, A. (2006). Pilot points method incorporating prior information for solving the groundwater flow inverse problem. *Adv. Water Resour.*, 29(11):1678–1689.

Allen, R. G., Pereira, L. S., Raes, D., and Smith, M. (1998). Crop evapotranspiration: Guidelines for computing crop water requirements. FAO Irrig. Drainage Pap. 56, Food and Agric. Organ., Rome.

Anderson, J. L. (2001). An ensemble adjustment Kalman filter for data assimilation. *Mon. Weather Rev.*, 129(12):2884–2903.

Anderson, J. L. (2007). An adaptive covariance inflation error correction algorithm for ensemble filters. *Tellus A*, 59(2):210–224.

Anderson, J. L. (2009). Spatially and temporally varying adaptive covariance inflation for ensemble filters. *Tellus A*, 61(1):72–83.

Anderson, M. (2005). Heat as a ground water tracer. *Ground Water*, 43(6):951–968.

Bailey, R. T. and Bau, D. A. (2010). Ensemble smoother assimilation of hydraulic head and return flow data to estimate hydraulic conductivity distribution. *Water Resour. Res.*, 46.

Bailey, R. T., Bau, D. A., and Gates, T. K. (2012). Estimating spatially-variable rate constants of denitrification in irrigated agricultural groundwater systems using an Ensemble Smoother. *J. Hydrol.*, 468:188–202.

Bauser, G., Hendricks Franssen, H. J., Kaiser, H. P., Kuhlmann, U., Stauffer, F., and Kinzelbach, W. (2010). Real-time management of an urban groundwater well field threatened by pollution. *Environ. Sci. Technol.*, 44(17):6802–6807.

Bear, J. and Chen, A. H.-D. (2010). *Modeling groundwater flow and contaminant transport*. Springer, Dordrecht.

Bishop, C., Etherton, B., and Majumdar, S. (2001). Adaptive sampling with the ensemble transform Kalman filter. Part I: Theoretical aspects. *Mon. Weather Rev.*, 129(3):420–436.

Blaschke, A. P., Steiner, K. H., Schmalfuss, R., Gutknecht, D., and Sengschmitt, D. (2003). Clogging processes in hyporheic interstices of an impounded river, the Danube at Vienna, Austria. *Int. Rev. Hydrobiol.*, 88(3-4):397–413.

Boano, F., Camporeale, C., Revelli, R., and Ridolfi, L. (2006). Sinuosity-driven hyporheic exchange in meandering rivers. *Geophys. Res. Lett.*, 33(18):L18406–.

Bouwer, H. and Maddock, T. (1997). Making sense of the interactions between groundwater and streamflow: Lessons for water masters and adjudicators. *Rivers*, 6(1):19–31.

Bravo, H. R., Jiang, F., and Hunt, R. J. (2002). Using groundwater temperature data to constrain parameter estimation in a groundwater flow model of a wetland system. *Water Resour. Res.*, 38(8).

Bruen, M. P. and Osman, Y. Z. (2004). Sensitivity of streamaquifer seepage to spatial variability of the saturated hydraulic conductivity of the aquifer. *J. Hydrol.*, 293(14):289 – 302.

Brunke, M. and Gonser, T. (1997). The ecological significance of exchange processes between rivers and groundwater. *Freshwater Biol.*, 37(1):1–33.

Brunner, P., Cook, P. G., and Simmons, C. T. (2009). Hydrogeologic controls on disconnection between surface water and groundwater. *Water Resour. Res.*, 45:W01422.

Brunner, P., Simmons, C. T., Cook, P. G., and Therrien, R. (2010). Modeling surface water-groundwater interaction with MODFLOW: Some considerations. *Ground Water*, 48(2):174–180.

Burgers, G., van Leeuwen, P. J., and Evensen, G. (1998). Analysis scheme in the ensemble Kalman filter. *Mon. Weather Rev.*, 126(6):1719–1724.

Calver, A. (2001). Riverbed Permeabilities: Information from Pooled Data. *Ground Water*, 39(4):546 – 553.

Camporese, M., Paniconi, C., Putti, M., and Salandin, P. (2009a). Comparison of Data Assimilation Techniques for a Coupled Model of Surface and Subsurface Flow. *Vadose Zone J.*, 8(4):837–845.

Camporese, M., Paniconi, C., Putti, M., and Salandin, P. (2009b). Ensemble Kalman filter data assimilation for a process-based catchment scale model of surface and subsurface flow. *Water Resour. Res.*, 45(10).

Cardenas, M. B., Wilson, J. L., and Zlotnik, V. A. (2004). Impact of heterogeneity, bed forms, and stream curvature on subchannel hyporheic exchange. *Water Resour. Res.*, 40(8):W08307.

Chen, Y. and Oliver, D. S. (2010). Cross-covariances and localization for EnKF in multiphase flow data assimilation. *Computational Geosciences*, 14(4):579–601.

Chen, Y. and Zhang, D. (2006). Data assimilation for transient flow in geologic formations via ensemble Kalman filter. *Adv. Water Resour.*, 29(8):1107 – 1122.

Conant, B. (2004). Delineating and quantifying ground water discharge zones using streambed temperatures. *Ground Water*, 42(2):243–257.

Constantz, J. (2008). Heat as a tracer to determine streambed water exchanges. *Water Resour. Res.*, 44:W00D10.

Constantz, J., Thomas, C. L., and Zellweger, G. (1994). Influence of diurnal variations in stream temperature on streamflow loss and groundwater recharge. *Water Resour. Res.*, 30(12):3253–3264.

Davies, H. C. and Turner, R. E. (1977). Updating prediction models by dynamical relaxation: an examination of the technique. *Quart. J. Roy. Meteor. Soc.*, 103(436):225–245.

de Marsily, G. (1978). *De l'identificaton des systèmes hydrogéologiques.* PhD thesis, Paris VI, Paris.

Delta h Ingenieurgesellschaft mbH (2006). Spring 3.3. Software. Witten, Germany.

Devegowda, D., Arroyo-Negrete, E., and Datta-Gupta, A. (2010). Flow relevant covariance localization during dynamic data assimilation using EnKF. *Adv. Water Resour.*, 33(2):129 – 145.

Domenico, P. A. and Schwartz, F. W. (1990). *Physical and chemical hydrogeology.* John Wiley & Sons, New York.

Doppler, T., Hendricks Franssen, H. J., Kaiser, H. P., Kuhlman, U., and Stauffer, F. (2007). Field evidence of a dynamic leakage coefficient for modelling river-aquifer interactions. *J. Hydrol.*, 347(1-2):177–187.

Doussan, C., Toma, A., Paris, B., Poitevin, G., Ledoux, E., and Detay, M. (1994). Coupled use of thermal and hydraulic head data to characterize river-groundwater exchanges. *J. Hydrol.*, 153(1-4):215 – 229.

Engeler, I., Hendricks Franssen, H. J., Müller, R., and Stauffer, F. (2011). The importance of coupled modelling of variably saturated groundwater flow-heat transport for assessing river-aquifer interactions. *J. Hydrol.*, 397(3-4):295–305.

Evensen, G. (1994). Sequential data assimilation with a nonlinear quasi-geostrophic model using monte-carlo methods to forecast error statistics. *J. Geophys. Res. C: Oceans*, 99(C5):10143–10162.

Evensen, G. (2003). The Ensemble Kalman Filter: theoretical formulation and practical implementation. *Ocean Dynamics*, 53:343–367.

Evensen, G. (2009). *Data Assimilation - The Ensemble Kalman Filter*. Springer-Verlag, 2 edition.

Evensen, G. and van Leeuwen, P. (2000). An ensemble Kalman smoother for nonlinear dynamics. *Mon. Weather Rev.*, 128(6):1852–1867.

Fleckenstein, J. H., Krause, S., Hannah, D. M., and Boano, F. (2010). Groundwater-surface water interactions: New methods and models to improve understanding of processes and dynamics. *Adv. Water Resour.*, 33(11):1291–1295.

Fleckenstein, J. H., Niswonger, R. G., and Fogg, G. E. (2006). River-aquifer interactions, geologic heterogeneity, and low-flow management. *Ground Water*, 44(6):837–852.

Frei, S., Fleckenstein, J. H., Kollet, S. J., and Maxwell, R. M. (2009). Patterns and dynamics of river-aquifer exchange with variably-saturated flow using a fully-coupled model. *J. Hydrol.*, 375(3-4):383–393.

Gaspari, G. and Cohn, S. E. (1999). Construction of correlation functions in two and three dimensions. *Quart. J. Roy. Meteor. Soc.*, 125(554):723–757.

Genereux, D. P., Leahy, S., Mitasova, H., Kennedy, C. D., and Corbett, D. R. (2008). Spatial and temporal variability of streambed hydraulic conductivity in West Bear Creek, North Carolina, USA. *J. Hydrol.*, 358(3-4):332–353.

Gómez-Hernández, J. and Journel, A. (1993). Joint sequential simulation of multi-Gaussian fields. In Soares, A., editor, *Geostatistics Tróia '92*, volume 1, pages 85–94. Kluwer Acad., New York.

Gómez-Hernández, J. and Wen, X.-H. (1998). To be or not to be multi-Gaussian? A reflection on stochastic hydrogeology. *Adv. Water Resour.*, 21(1):47 – 61.

Hamill, T., Whitaker, J., and Snyder, C. (2001). Distance-dependent filtering of background error covariance estimates in an ensemble Kalman filter. *Mon. Weather Rev.*, 129(11):2776–2790.

Hatch, C. E., Fisher, A. T., Ruehl, C. R., and Stemler, G. (2010). Spatial and temporal variations in streambed hydraulic conductivity quantified with time-series thermal methods. *J. Hydrol.*, 389(3-4):276–288.

Heberer, T. (2002). Tracking persistent pharmaceutical residues from municipal sewage to drinking water. *J. Hydrol.*, 266(3-4):175–189.

Hendricks Franssen, H. J., Alcolea, A., Riva, M., Bakr, M., van der Wiel, N., Stauffer, F., and Guadagnini, A. (2009). A comparison of seven methods for the inverse modelling of groundwater flow. Application to the characterisation of well catchments. *Adv. Water Resour.*, 32(6):851–872.

Hendricks Franssen, H. J., Kaiser, H. P., Kuhlmann, U., Bauser, G., Stauffer, F., Mueller, R., and Kinzelbach, W. (2011). Operational real-time modeling with ensemble Kalman filter of variably saturated subsurface flow including stream-aquifer interaction and parameter updating. *Water Resour. Res.*, 47:W02532.

Hendricks Franssen, H. J. and Kinzelbach, W. (2008). Real-time groundwater flow modeling with the Ensemble Kalman Filter: Joint estimation of states and parameters and the filter inbreeding problem. *Water Resour. Res.*, 44(9):W09408.

Hendricks Franssen, H. J. and Kinzelbach, W. (2009). Ensemble Kalman filtering versus sequential self-calibration for inverse modelling of dynamic groundwater flow systems. *J. Hydrol.*, 365(3-4):261–274.

Houtekamer, P. L. and Mitchell, H. L. (1998). Data assimilation using an Ensemble Kalman Filter technique. *Mon. Weather Rev.*, 126(3):796 – 811.

Huber, E., Hendricks Franssen, H. J., Kaiser, H., and Stauffer, F. (2011). The role of prior model calibration on predictions with Ensemble Kalman Filter. *Ground Water*, 49(6):845–858.

Irvine, D. J., Brunner, P., Hendricks Franssen, H. J., and Simmons, C. T. (2012). Heterogeneous or homogeneous? Implications of simplifying heterogeneous streambeds in models of losing streams. *J. Hydrol.*, 424425(0):16 – 23.

Jafarpour, B. and Tarrahi, M. (2011). Assessing the performance of the ensemble Kalman filter for subsurface flow data integration under variogram uncertainty. *Water Resour. Res.*, 47(5).

Jiang, Y. and Woodbury, A. D. (2006). A full-Bayesian approach to the inverse problem for steady-state groundwater flow and heat transport. *Geophys. J. Int.*, 167(3):1501–1512.

Kalbus, E., Reinstorf, F., and Schirmer, M. (2006). Measuring methods for groundwater - surface water interactions: a review. *Hydrol. Earth Syst. Sci.*, 10(6):873–887.

Kalbus, E., Schmidt, C., Molson, J. W., Reinstorf, F., and Schirmer, M. (2009). Influence of aquifer and streambed heterogeneity on the distribution of groundwater discharge. *Hydrol. Earth Syst. Sci.*, 13(1):69–77.

Kalman, R. E. (1960). A new approach to linear filtering and prediction problems. *J. Basic Eng.*, 82 (Series D):35–45.

Käser, D. H., Binley, A., Heathwaite, A. L., and Krause, S. (2009). Spatio-temporal variations of hyporheic flow in a riffle-step-pool sequence. *Hydrol. Process.*, 23(15):2138–2149.

Kennedy, C. D., Genereux, D. P., Corbett, D. R., and Mitasova, H. (2009). Spatial and temporal dynamics of coupled groundwater and nitrogen fluxes through a streambed in an agricultural watershed. *Water Resour. Res.*, 45:W09401.

Kerrou, J., Renard, P., Hendricks Franssen, H.-J., and Lunati, I. (2008). Issues in characterizing heterogeneity and connectivity in non-multiGaussian media. *Adv. Water Resour.*, 31(1):147 – 159.

Kollet, S. J. and Maxwell, R. M. (2006). Integrated surface-groundwater flow modeling: A free-surface overland flow boundary condition in a parallel groundwater flow model. *Adv. Water Resour.*, 29:945–958.

Krause, S., Bronstert, A., and Zehe, E. (2007). Groundwater-surface water interactions in a North German lowland floodplain - Implications for the river discharge dynamics and riparian water balance. *J. Hydrol.*, 347(3-4):404–417.

Kurtz, W., Hendricks Franssen, H.-J., Brunner, P., and Vereecken, H. (2013a). Is inversion based high resolution characterization of spatially heterogeneous river bed hydraulic conductivity needed and possible? *Hydrol. Earth Syst. Sci. Discuss.*, 10(5):5831–5873.

Kurtz, W., Hendricks Franssen, H. J., Kaiser, H.-P., and Vereecken, H. (2013b). Joint assimilation of piezometric heads and groundwater temperatures for improved assessment of river-aquifer interactions. UNDER PREPARATION FOR: *Water Resour. Res.*

Kurtz, W., Hendricks Franssen, H.-J., and Vereecken, H. (2012). Identification of time-variant river bed properties with the ensemble Kalman filter. *Water Resour. Res.*, 48(10):W10534.

Li, L., Zhou, H., Gómez-Hernández, J. J., and Hendricks Franssen, H. J. (2012). Jointly mapping hydraulic conductivity and porosity by assimilating concentration data via ensemble Kalman filter. *J. Hydrol.*, 428-429(0):152 – 169.

Liang, B., Sepehrnoori, K., and Delshad, M. (2009). A Weighted Ensemble Kalman Filter for Automatic History Matchings. *Pet. Sci. Technol.*, 27(10):1062–1091.

Liu, G., Chen, Y., and Zhang, D. (2008). Investigation of flow and transport processes at the MADE site using ensemble Kalman filter. *Adv. Water Resour.*, 31(7):975 – 986.

Lorentzen, R., Naevdal, G., and Lage, A. (2003). Tuning of parameters in a two-phase flow model using an ensemble Kalman filter. *Int. J. Multiphase Flow*, 29(8):1283–1309.

Ma, R. and Zheng, C. (2010). Effects of density and viscosity in modeling heat as a groundwater tracer. *Ground Water*, 48(3):380–389.

Montzka, C., Pauwels, V. R. N., Hendricks Franssen, H. J., Han, X., and Vereecken, H. (2012). Multivariate and Multiscale Data Assimilation in Terrestrial Systems: A Review. *Sensors*, 12(12):16291–16333.

Moradkhani, H., Sorooshian, S., Gupta, H. V., and Houser, P. R. (2005). Dual state-parameter estimation of hydrological models using ensemble Kalman filter. *Adv. Water Resour.*, 28(2):135–147.

Muskat, M. (1937). *The Flow of Homogenous Fluids through Porous Media*. McGraw-Hill, New York.

Mutiti, S. and Levy, J. (2010). Using temperature modeling to investigate the temporal variability of riverbed hydraulic conductivity during storm events. *J. Hydrol.*, 388(3-4):321–334.

Naevdal, G., Johnsen, L., Aanonsen, S., and Vefring, E. (2005). Reservoir monitoring and continuous model updating using ensemble Kalman filter. *SPE J.*, 10(1):66–74. 2003 SPE Annual Technical Conference and Exhibition, DENVER, CO, OCT 05-08, 2003.

Nan, T. and Wu, J. (2011). Groundwater parameter estimation using the ensemble Kalman filter with localization. *Hydrogeol. J.*, 19(3):547–561.

Nowak, W. (2009). Best unbiased ensemble linearization and the quasi-linear Kalman ensemble generator. *Water Resour. Res.*, 45:W04431.

Panday, S. and Huyakorn, P. S. (2004). A fully coupled physically-based spatially distributed model for evaluating surface/subsurface flow. *Adv. Water Resour.*, 27:361–382.

Pasetto, D., Camporese, M., and Putti, M. (2012). Ensemble Kalman filter versus particle filter for a physically-based coupled surface-subsurface model. *Adv. Water Resour.*, 47:1–13.

Racz, A. J., Fisher, A. T., Schmidt, C. M., Lockwood, B. S., and Los Huertos, M. (2012). Spatial and temporal infiltration dynamics during managed aquifer recharge. *Ground Water*, 50(4):562–570.

Rehg, K. J., Packman, A. I., and Ren, J. H. (2005). Effects of suspended sediment characteristics and bed sediment transport on streambed clogging. *Hydrol. Process.*, 19(2):413–427.

Renard, P., Le Loc'h, G., Ledoux, E., de Marsily, G., and Mackay, R. (2000). A fast algorithm for the estimation of the equivalent hydraulic conductivity of heterogeneous media. *Water Resour. Res.*, 36(12):3567–3580.

Rosenberry, D. O. and Pitlick, J. (2009a). Effects of sediment transport and seepage direction on hydraulic properties at the sediment-water interface of hyporheic settings. *J. Hydrol.*, 373(3-4):377–391.

Rosenberry, D. O. and Pitlick, J. (2009b). Local-scale variability of seepage and hydraulic conductivity in a shallow gravel-bed river. *Hydrol. Process.*, 23(23):3306–3318.

Sahuquillo, A., Capilla, J., Gómez-Hernández, J., and Andreu, J. (1992). Conditional simulation of transmissivity fields honoring piezometric data. In Blain, W. R. and Cabrera, E., editors, *Hydraulic Engineering Software IV: Fluid Flow Modeling*, pages 201–214. WIT Press.

Schälchli, U. (1992). The clogging of coarse gravel river beds by fine sediment. *Hydrobiologia*, 235:189–197.

Schmidt, C., Bayer-Raich, M., and Schirmer, M. (2006). Characterization of spatial heterogeneity of groundwater-stream water interactions using multiple depth streambed temperature measurements at the reach scale. *Hydrol. Earth Syst. Sci.*, 10(6):849–859.

Schöniger, A., Nowak, W., and Hendricks Franssen, H. J. (2012). Parameter estimation by ensemble Kalman filters with transformed data: Approach and application to hydraulic tomography. *Water Resour. Res.*, 48:W04502.

Schornberg, C., Schmidt, C., Kalbus, E., and Fleckenstein, J. H. (2010). Simulating the effects of geologic heterogeneity and transient boundary conditions on streambed temperatures - Implications for temperature-based water flux calculations. *Adv. Water Resour.*, 33(11):1309–1319.

Schubert, J. (2002). Hydraulic aspects of riverbank filtration-field studies. *J. Hydrol.*, 266(3-4):145 – 161.

Scietec Flussmanagement GmbH (2000). FLORIS2000. Software. Linz, Austria.

Sophocleous, M. (2002). Interactions between groundwater and surface water: the state of the science. *Hydrogeol. J.*, 10(1):52–67.

Springer, A. E., Petroutson, W. D., and Semmens, B. A. (1999). Spatial and temporal variability of hydraulic conductivity in active reattachement bars of the Colorado river, Grand Canyon. *Ground Water*, 37(3):338 – 344.

Sun, A. Y., Morris, A. P., and Mohanty, S. (2009). Comparison of deterministic ensemble Kalman filters for assimilating hydrogeological data. *Adv. Water Resour.*, 32(2):280–292.

Tippett, M., Anderson, J., Bishop, C., Hamill, T., and Whitaker, J. (2003). Ensemble square root filters. *Mon. Weather Rev.*, 131(7):1485–1490.

Tufenkji, N., Ryan, J. N., and Elimelech, M. (2002). The promise of bank filtration. *Environ. Sci. Technol.*, 36(21):422A–428A.

van Genuchten, M. T. (1980). A closed-form equation for predicting the hydraulic conductivity of unsaturated soils. *Soil Sci. Soc. Am. J.*, 44(5):892–898.

van Leeuwen, P. and Evensen, G. (1996). Data assimilation and inverse methods in terms of a probabilistic formulation. *Mon. Weather Rev.*, 124(12):2898–2913.

van Leeuwen, P. J. (2009). Particle filtering in geophysical systems. *Mon. Weather Rev.*, 137(12):4089–4114.

Vandenbohede, A. and Van Houtte, E. (2012). Heat transport and temperature distribution during managed artificial recharge with surface ponds. *J. Hydrol.*, 472-473(0):77–89.

VanderKwaak, J. E. and Loague, K. (2001). Hydrologic-response simulations for the r-5 catchment with a comprehensive physics-based model. *Water Resour. Res.*, 37(4):999–1013.

Vogt, T., Schirmer, M., and Cirpka, O. A. (2012). Investigating riparian groundwater flow close to a losing river using diurnal temperature oscillations at high vertical resolution. *Hydrol. Earth Syst. Sci.*, 16:473–487.

Wett, B., Jarosch, H., and Ingerle, K. (2002). Flood induced infiltration affecting a bank filtrate well at the River Enns, Austria. *J. Hydrol.*, 266(34):222 – 234.

Whitaker, J. and Hamill, T. (2002). Ensemble data assimilation without perturbed observations. *Mon. Weather Rev.*, 130(7):1913–1924.

Winter, T. C. (1999). Relation of streams, lakes, and wetlands to groundwater flow systems. *Hydrogeol. J.*, 7:28–45.

Woessner, W. W. (2000). Stream and fluvial plain ground water interactions: Rescaling hydrogeologic thought. *Ground Water*, 38(3):423–429.

Woodbury, A. D. and Smith, L. (1988). Simultaneous inversion of hydrogeologic and thermal data. 2. incorporation of thermal data. *Water Resour. Res.*, 24(3):356–372.

Zhang, Y., Hubbard, S., and Finsterle, S. (2011). Factors Governing Sustainable Groundwater Pumping near a River. *Ground Water*, 49(3):432–444.

Zhou, H., Gómez-Hernández, J. J., Hendricks Franssen, H. J., and Li, L. (2011). An approach to handling non-Gaussianity of parameters and state variables in ensemble Kalman filtering. *Adv. Water Resour.*, 34(7):844 – 864.

Zimmerman, D. A., de Marsily, G., Gotway, C. A., Marietta, M. G., Axness, C. L., Beauheim, R. L., Bras, R. L., Carrera, J., Dagan, G., Davies, P. B., Gallegos, D. P., Galli, A., Gómez-Hernández, J. J., Grindrod, P., Gutjahr, A. L., Kitanidis, P. K., Lavenue, A. M., McLaughlin, D., Neuman, S. P., RamaRao, B. S., Ravenne, C., and Rubin, Y. (1998). A comparison of seven geostatistically based inverse approaches to estimate transmissivities for modeling advective transport by groundwater flow. *Water Resour. Res.*, 34(6):1373–1413.

Zinn, B. and Harvey, C. F. (2003). When good statistical models of aquifer heterogeneity go bad: A comparison of flow, dispersion, and mass transfer in connected and multivariate Gaussian hydraulic conductivity fields. *Water Resour. Res.*, 39(3).

Acknowledgements

First of all, I would like to thank Prof. Dr. Harrie-Jan Hendricks Franssen for the intensive supervision during the course of my doctoral studies and for introducing me into science. I also would like to acknowledge Prof. Dr. Harry Vereecken for making this PhD work possible. My thanks also go to the following people for the support during my PhD:

- Beatrice Marti for helping me with the Hardhof data, for fruitful discussions about the model and for hospitality during my visits in Zurich
- Dr. Uli Kuhlmann for help with the assimilation code and SPRING
- Dr. Hans-Peter Kaiser for giving an introduction to the water management at the Hardhof site and for help with the Hardhof data
- Pramod Kumbhar for help in optimizing and parallelizing the assimilation code
- The group of Prof. Dr. Reed Maxwell for hosting me for a three-month stay at their institute
- Prof. Dr. Philip Brunner and Prof. Dr. Wolfgang Kinzelbach for agreeing to review my thesis
- Water works Zurich for providing the Hardhof data
- Jülich Supercomputing Center for granting the required computation time on JUROPA
- IBG-3's institutes band for distraction after work

Very special thanks, of course, go to my parents and Julia for patience and constant support.

Band / Volume 187
Ab initio investigation of ground-states and ionic motion in particular in zirconia-based solid-oxide electrolytes
J. A. Hirschfeld (2013), v, 144 pp
ISBN: 978-3-89336-897-6

Band / Volume 188
Entwicklung protonenleitender Werkstoffe und Membranen auf Basis von Lanthan-Wolframat für die Wasserstoffabtrennung aus Gasgemischen
J. Seeger (2013), V, 130 pp
ISBN: 978-3-89336-903-4

Band / Volume 189
Entwicklung und Herstellung von metallgestützten Festelektrolyt-Brennstoffzellen (MSC-SOFC) mit einem Sol-Gel-Elektrolyten
S. D. Vieweger (2013), xviii, 176 pp
ISBN: 978-3-89336-904-1

Band / Volume 190
Mobile Brenngaserzeugungssysteme mit Mitteldestillaten für Hochtemperatur-PEFC
C. Wiethege (2013), iii, 179 pp
ISBN: 978-3-89336-905-8

Band / Volume 191
Verbundvorhaben Öko-effiziente Flugzeugsysteme für die nächste Generation (EFFESYS) - Teilprojekt Brennstoffzelle, Infrastruktur, Komponenten und System (BRINKS) – Schlussbericht
J. Pasel, R.C. Samsun, H. Janßen, W. Lehnert, R. Peters, D. Stolten (2013), xii, 152 pp
ISBN: 978-3-89336-908-9

Band / Volume 192
Analyse des Betriebsverhaltens von Hochtemperatur-Polymerelektrolyt-Brennstoffzellen
L. Lüke (2013), 150 pp
ISBN: 978-3-89336-909-6

Band / Volume 193
Full-waveform inversion of crosshole GPR data for hydrogeological applications
A. Klotzsche (2013), X, 164 pp
ISBN: 978-3-89336-915-7

Band / Volume 194
Long Term Stability and Permeability of Mixed Ion Conducting Membranes under Oxyfuel Conditions
X. Li (2013), III, 143 pp
ISBN: 978-3-89336-916-4

Band / Volume 195
Innovative Beschichtungs- und Charakterisierungsmethoden für die nasschemische Herstellung von asymmetrischen Gastrennmembranen auf Basis von SiO_2
J. Hoffmann (2013), V, 152 pp
ISBN: 978-3-89336-917-1

Band / Volume 196
Aerosol processes in the Planetary Boundary Layer: High resolution Aerosol Mass Spectrometry on a Zeppelin NT Airship
F. Rubach (2013), iii, 141 pp
ISBN: 978-3-89336-918-8

Band / Volume 197
Institute of Energy and Climate Research IEK-6: Nuclear Waste Management - Report 2011 / 2012 Material Science for Nuclear Waste Management
M. Klinkenberg, S. Neumeier, D. Bosbach (Eds.) (2013), 195 pp
ISBN: 978-3-89336-980-1

Band / Volume 198
Material migration in tokamak plasmas with a three-dimensional boundary
R. Laengner (2013), vi, 140, XVII pp
ISBN: 978-3-89336-924-9

Band / Volume 199
Improved characterization of river-aquifer interactions through data assimilation with the Ensemble Kalman Filter
W. Kurtz (2013), xxv, 125 pp
ISBN: 978-3-89336-925-6

Weitere ***Schriften des Verlags im Forschungszentrum Jülich*** unter
http://wwwzb1.fz-juelich.de/verlagextern1/index.asp

Energie & Umwelt / Energy & Environment
Band / Volume 199
ISBN 978-3-89336-925-6